A Homogenized Thermal Model For Lithium Ion Batteries

Erlend Finden

Norwegian University of Life Sciences
Department of Mathematical Sciences and Technology
Master Thesis 30 credits 2012

Preface

This thesis has been written as an accomplishment of my Master's degree at the Norwegian University of Life Sciences (UMB).

On this occasion, I want first of all to thank my supervisors Professor John Wyller, Senior Research Scientist Preben Vie and Associate Professor Espen Olsen. Without their heavy experience with scientific writing and their expertize in the fields of mathematics, chemistry and physics this work would not have been possible. In addition to hold very instructive weekly meetings, John even offered a handful very inspiring and useful seminars on the finite element method for the three of us, having him as a supervisor. He also checks his email at late hours, thus letting the discussion about mathematical problems be continuous in the time variable. Preben Vie included me in the batteries and fuel cells research group at the Norwegian Institute for Energy Technology (IFE). I want to thank him for letting me write my Master's thesis at IFE in excellent office facilities and in an inspiring research environment. He also provided experimental data for this work and gave many very instructive lessons on battery technology.

I also want to thank Thomas Holm for being helpful with sharing literature from NTNU's library resources. He provided articles the UMB library do not offer electronically. This really speed-ed up my literature study.

I express my gratitude to Hilde Larsen, Ole Elvethun and Dr. Odne Burheim. Hilde Larsen has been a friendly classmate from the first day at the University. In the period writing the master's thesis she has answered many of my questions about writing in LaTeX. Ole Elvethun has helped me by sharing his experience with the FEniCS software. Without him the implementation would have been a hard process. I am grateful that Dr. Odne Burheim found time to an introductory hour with the Comsol Multiphysics software. We also had a very instructive discussion regarding his planned paper on thermal modeling of lithium ion batteries.

I owe a special thanks to the battery research group at the Norwegian Defence Research Establishment for their support in this project.

Very important is the support I have at home. Linn's patience with a

man that at times spends much time on studies are remarkable. Thank you Linn. I also want to thank my parents for supporting me during my years at the University. I am grateful that they are letting me use the veterinary office which now serves as a mathematics and physics laboratory. At last I want to thank Sveinung Mjelde for calling forth my interest for mathematics. During his inspiring lessons at secondary school I realized that mathematics is the language that describes the physical world. Finally I say cheers to all inspiring teachers, family members, student fellows and friends for making the everyday life as a student a positive experience.

Ydersbond, May 14, 2012 *Erlend Finden*

Summary

In this work homogenization theory is applied to existing thermal models for lithium ion batteries. We study a battery with prismatic cell geometry. The inner region of the battery has a thermal conductivity that is periodic in a local variable. In this work we describe the inner region by a homogenized partial differential equation. The obtained homogenized thermal conductivity tensor is equivalent with the tensor obtained by applying a thermal equivalent-resistance approach. Thermal equivalent-resistance approaches are reported in the literature on thermal modeling of lithium ion batteries. Furthermore, the homogenized thermal conductivity in different directions varies by a factor 10. The outer region of the battery consist of a casing that is wrapped around the inner region. The outer region is described by a non-homogenized partial differential equation. Both regions is described by the two coupled partial differential equations in dimensionless form. The coupled model is applied to a conventional lithium ion pouch-cell battery with 17.5 Ah capacity. Input data to the model are obtained from experiments. The model is solved in 2 dimensions by means of the finite element method in the FEniCS software. As input parameters, an ambient temperature and an initial condition of 298 (K) are applied. Moreover is the external heat transfer coefficient estimated to be 18 ($\mathrm{W/m^2\ K}$). Simulations of a $1C$ discharge from 100 to 10% state of charge is performed. The modeled battery consists in 2 dimensions of a rectangle with long and short sides. It was found that the temperature parallel with the long side varied significant compared with the temperature parallel with the short side. A maximum temperature is achieved in the center of the battery. This occurs at the time just before the battery is at end of discharge. The maximum temperature is 2.4 (K) above the ambient air temperature. A validation of the results are necessary.

Contents

Nomenclature

Symbol	Description	Unit
a'	Constant	(V/s^3)
$\tilde{a}$	Constant	(V)
a_u	Constant	(V)
a_v	Constant	(V)
$a(\hat{u}, \hat{v})$	Bilinear form	-
$a(u, v)$	Bilinear form	-
A	Scaling constant	(K)
A_0	Differential operator	-
A_1	Differential operator	-
A_2	Differential operator	-
b'	Constant	(V/s^2)
$\tilde{b}$	Constant	(V)
b_u	Constant	(V)
b_v	Constant	(V)
B	Scaling constant	(K)
c'	Constant	(V/s)
$\tilde{c}$	Constant	(V)
c_u	Constant	(V)
c_v	Constant	(V)
C	Scaling constant	(J/m^{3}K)
C_1	Integration constant	-
C_p	Specific heat capacity	(J/kg K)

Symbol	Description	Unit
d'	Constant	(V)
$\tilde{d}$	Constant	(V)
d_u	Constant	(V)
d_v	Constant	(V)
D	Differential operator	(m^{-1})
$D_{\gamma\xi}$	Differential operator	-
D_ξ	Differential operator	-
D'_ξ	Differential operator	-
DOD	Depth of discharge	
$e(T)$	Convection coefficient	($J/m^2K\ s^{0.5}$)
f	Dimensionless mass density $\cdot$ heat capacity	-
$f(\hat{v})$	Linear form	-
$f(v)$	Linear form	-
g	Ambient air temperature	(K)
g'	Constant	(W/m^2)
h	External heat transfer coefficient	(W/m^2K)
h'	Constant	(W/m^2)
i	Scaling constant	(A)
$\underline{i}$	Unit vector in ξ_1-direction	(A)
I	Current	(A)
K_1	Numerical parameter	-
K_2	Numerical parameter	-
L_{x_i}	Scaling constant	(m)
L_i	Scaling constant	(m)
L_{kar}	Length convection estimation	(m)
L_Y	Period length	(m)
$L_{Y\xi}$	Period length	-
L_{ξ_i}	Scaling constant	(m)
$L_{i\Omega_a}$	Inner region start coordinate	(m)
$L_{i\Omega_b}$	Inner region end coordinate	(m)
$L_{i\Gamma_a}$	Inner region start coordinate	-
$L_{i\Gamma_b}$	Inner region start coordinate	-
$\underline{n}$	Unit normal vector	-
$\underline{n_1}$	Unit normal vector	-
$\underline{n_2}$	Unit normal vector	-
q	Source term	(W/m^3)
Q	Dimensionless source term	-
SOC	State of charge	-

Symbol	Description	Unit
t	Time	(s)
t_c	Time, current cut off	(s)
t_τ	Scaling constant	(s)
T	Temperature	(K)
T_0	Initial temperature	(K)
T_c	Time at end of discharge	(h)
$\hat{u}$	Dimensionless temperature	-
u	Dimensionless temperature	-
U	Open-circuit potential	(V)
$\hat{v}$	Test function	-
v	Test function	-
$vol(\Omega_1)$	Volume of battery interior	(m^3)
V	Closed-circuit potential	(V)
w_i	Y-periodic function	-
$\underline{x}$	Euclidean coordinate vector	(m)
x_1	Euclidean coordinate	(m)
x_2	Euclidean coordinate	(m)
x_3	Euclidean coordinate	(m)
X	Function space	-
X'	Function space	-
$\hat{X}$	Function space	-
$\hat{X}'$	Function space	-
y	Local dimensionless variable	-
z	Y-periodic function	-

Table 1: Greek

Symbol	Description	Unit
α	Scaling constant	(W/mK)
$\hat{\alpha}$	Potential difference function	(V)
$\hat{\beta}$	Entropic heat coefficient	(V/K)
$\Delta\tau$	Finite difference parameter	-
ε	Micro to macro scale ratio	-
λ	Thermal conductivity tensor	(W/m^2 K)
Λ	Dimensionless thermal conductivity tensor	-
Λ_1	Dimensionless thermal conductivity	-
γ_i	Dimensionless scaling constant	-
Γ	Scaled region	-
Γ_1	Scaled region, interior	-
Γ_2	Scaled region, casing	-
$\partial\Gamma$	Scaled boundary	-
$\partial\tilde{\Gamma}$	Scaled boundary	-
Ω	Region, battery	-
Ω_1	Region, battery interior	-
Ω_2	Region, battery casing	-
$\partial\Omega$	Boundary, battery	-
ρ	Mass density	(kg/m^3)
τ	Dimensionless time	-
τ_c	Dimensionless time, current cut off	-
τ_k	Discrete dimensionless time	-
θ	Finite difference parameter	-
σ	Depth of discharge	-
ν	Air velocity	(m/s)
χ	Y-periodic function	-
Φ	Function	-
z_1	Function	-
$\underline{\xi}$	Dimensionless coordinate vector	-
ξ_1	Dimensionless coordinate	-
ξ_2	Dimensionless coordinate	-
ξ_3	Dimensionless coordinate	-

Table 2: Subscript

Symbol	Description	Value
i	-	1,2,3
k	Time counter	1,2,3,..

Table 3: Superscript

Symbol	Description	Value
k	Time counter	1,2,3,..

Chapter 1

Introduction

Lithium ion batteries have been on the commercial market since they were introduced by SONY Inc. in 1991. These batteries have been used in video recorders, cellular phones and laptops, among others [40]. Moreover, compared with other battery chemistries, lithium ion batteries offers both higher specific energy and higher energy density. Therefore they are preferred for use in electric and hybrid electric vehicles. However, by 2011 lithium ion batteries were still prevented from being widely introduced for use in electric and hybrid electric vehicles due to issues regarding safety, cost, and low temperature performance [2]. One safety issue is the possibility of a thermal runaway due to abuse behavior of the battery. Thermal runaway can occur due to exothermic reactions that are believed to occur above certain temperatures [55]. Furthermore, one factor that affects the cost of a battery is its lifetime. Moreover there are strong connections between the internal temperature of a lithium ion battery, and its lifetime [2]. It is therefore clear that it is of great importance to obtain information about the temperature field inside lithium ion batteries. One way of obtaining this information is by means of mathematical modeling.

Therefore, we will in this work first consider the properties of a conventional so-called lithium ion pouch-cell. This pouch-cell is made for use in electric vehicles. Thermal models presented in the literature are then studied. Motivated by the periodic micro-structure inside the pouch-cell, we apply mathematical homogenization theory to existing thermal models. A homogenized thermal model for lithium ion batteries is then derived. The homogenized model is equipped with input parameters obtained from experiments conducted on the pouch-cell. Finally the model is solved by means of numerical methods, and modeling results are presented.

1.1 Lithium Ion Batteries

A typical lithium ion battery cell consists of a pair of electrodes with current collectors, a separator and an electrolyte. In accordance with the literature on lithium ion batteries [56], we refer to the negative and the positive electrode as anode and cathode, respectively. The anode typically consists of a carbon material which exhibits a layered microscopic structure. Conventional cathode materials for lithium ion batteries also have a layered structure, and the preferred material is typically a metal oxide [15]. Both of the electrodes are in contact with a current collector. The current collector for the anode is typically made of copper. For the cathode current collector, aluminum is the preferred material [15]. We emphasize that more advanced structures than layered have been used for electrode materials [15]. We do not pursue any details on such materials in this work, however. Figure 1.1 shows a schematic representation of a lithium ion battery cell.

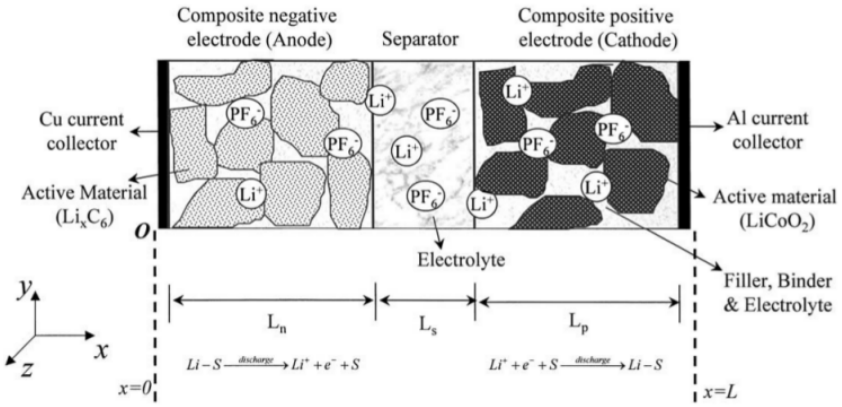

Figure 1.1: Schematic representation of lithium ion cell configuration. Length of anode, cathode and separator are denoted as L_n, L_s and L_p, respectively. Originally presented by Gomadam et al. Reprinted with permission from Elsevier.

The layered structure of the electrodes allows intercalation of lithium ions, i.e. the lithium ions can be inserted and stored between the layers of the electrodes [15]. The intercalation process is a so-called topotactic reaction. This process is characterized by the fact that no significant structural changes occur in the electrodes when the lithium ions are intercalated [15]. The electrodes in lithium ion batteries are commonly also referred to as lithium insertion compounds [39]. Lithium ion batteries are also called rocking chair

batteries. The name origins from the lithium ions that "rock" back and forth between the two electrodes when the battery is cycled [15].

In a fully charged lithium ion battery, the anode contains the maximum amount of lithium ions while the cathode has the opposite situation [21]. As the battery is discharged, the lithium ions are deintercalated from the anode, thus the anode is oxidized. At the cathode, these lithium ions are intercalated and the cathode is reduced [15]. The opposite process occur during charge [15].

Chapter 2

A Lithium Ion Pouch-Cell

In this chapter we study a conventional lithium ion battery made for use in electric vehicles. This type of batteries are commonly referred to as pouch-cell batteries. The battery has a nominal capacity of 17.5 Ah and provides a voltage of approximately 4.1 V, when fully charged. A picture of this battery is shown in figure 2.1.

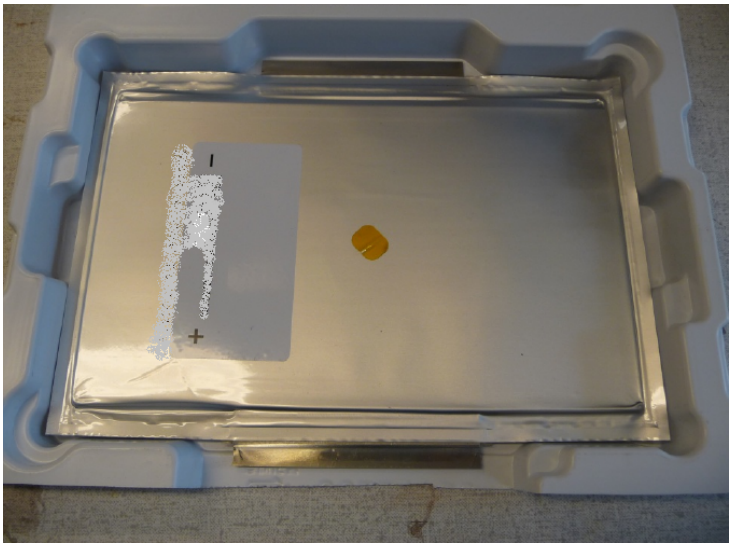

Figure 2.1: Lithium ion battery of pouch-cell type. Nominal capacity 17.5 Ah. 4.1 V provided when fully charged. Photographer: Erlend Finden.

2.1 Battery Structure

For modeling purposes it is important to obtain information about the internal geometry of the battery. Based on descriptions of pouch-cell batteries in the literature, we assume that this pouch-cell battery has a prismatic cell geometry. A few earlier modeling works on lithium ion batteries presents the prismatic cell geometry. An illustration which is presented in a work by Chen and Evans [12] is shown in figure 2.2. In their illustration the battery is composed of several layers of electrodes, currents collectors and separators in a periodic pattern. This configuration yields a parallel connection of all the unit cells. In this work we define a unit cell as a cell composed of layers of anode current collector, anode, electrolyte, separator, cathode and cathode current collector.

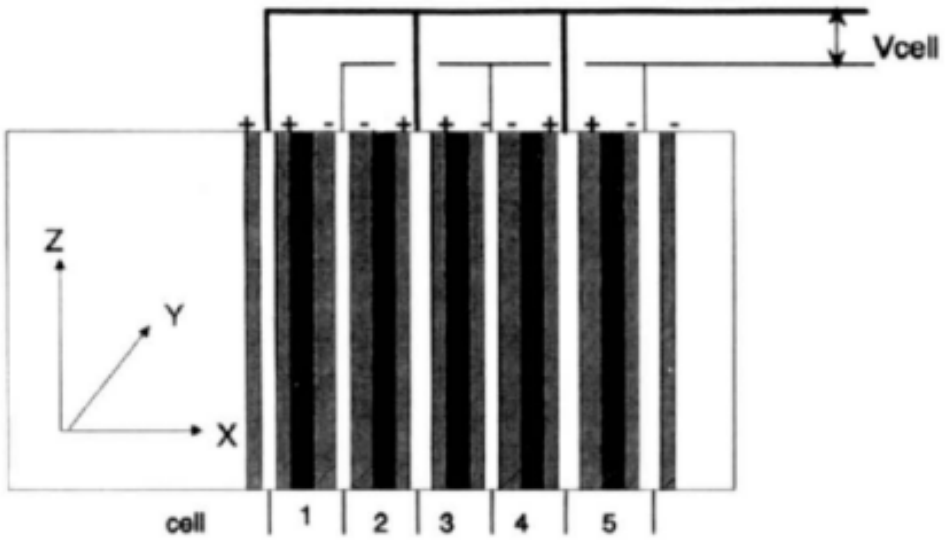

Figure 2.2: Schematic representation of prismatic lithium ion cell configuration. White, gray and black layers illustrates the current collectors, electrodes and separators, respectively. Unit cells are labeled 1-6. This configuration yields a parallel connection of unit cells. Originally presented by Chen and Evans [12]. Reproduced by permission of ECS - The Electrochemical Society.

Also Spotnitz and Franklin [55] illustrates the internal geometry in their thermal model for prismatic lithium ion batteries. Their illustration is presented in figure 2.3.

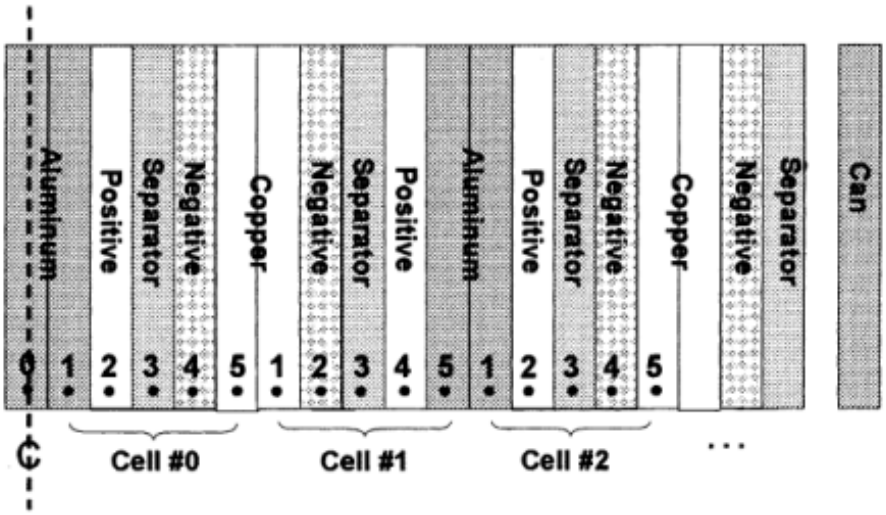

Figure 2.3: Schematic representation of prismatic lithium ion cell configuration. Positive and negative electrodes are labeled "Positive" and "Negative", respectively. Positive current collector is labeled "Aluminium" while negative current collector is labeled "Copper". 1-5 represents unit cells as indicated with "Cell # " labels. Also casing surrounding the battery interior are shown in this illustration. Casing is labeled "Can". This figure was originally presented by Spotnitz and Franklin [55]. Reprinted with permission from Elsevier.

By studying figure 2.3 we observe that the geometry is similar as in figure 2.2. Based on the works by Chen and Evans [12] and Spotnitz and Franklin [55] we therefore assume that the pouch-cell obeys the prismatic cell configuration illustrated in this section.

To describe the pouch-cell further it is convenient to specify a coordinate system. Let us introduce an Euclidean coordinate system with a coordinate vector $\underline{x}$ defined as

$$\underline{x} = [x_1, x_2, x_3]$$

Let us assume that the pouch-cell has a casing wrapped around the battery interior. We assume that the casing consists of an aluminum layer which is coated at the outside with a plastic film and at the inside with the separator material. In accordance with the literature, let us furthermore assume that the battery in the x_1-direction has the following composition: Plastic coating, *Al*-casing, separator, cathode current collector, cathode, separator,

anode, anode current collector, anode, separator, cathode, cathode current collector, cathode, separator,...,cathode, cathode current collector, separator, *Al*-casing, plastic coating. This composition is visualized in figure 2.4, where only the first few layers of unit cells in the x_1- direction are illustrated.

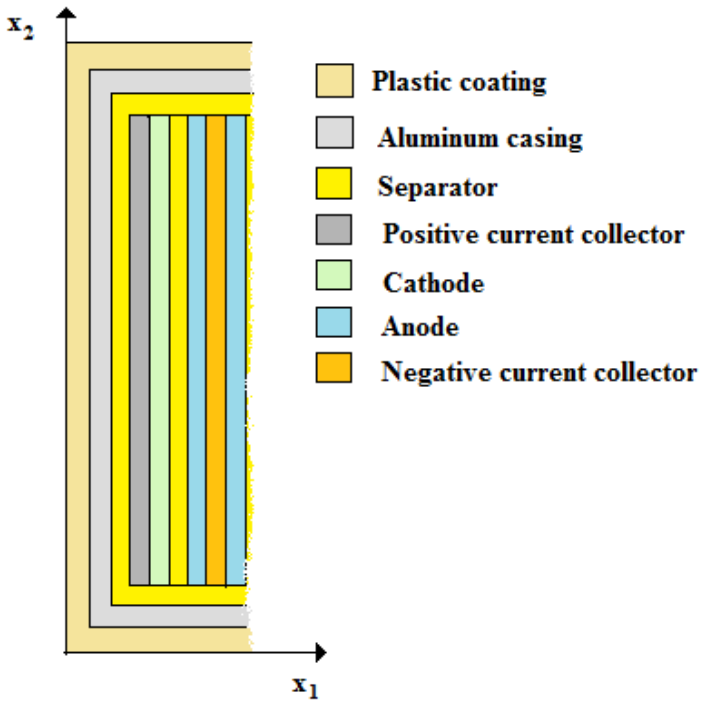

Figure 2.4: Schematic representation of the pouch-cell configuration. The illustration is at a given x_3-value in the $x_1 - x_2$ plane. Only the first few layers of unit cells in the x_1-direction are illustrated. The casing which is wrapped around the battery interior is here composed of an aluminum layer coated with plastic at the outside and coated with the separator material at the inside.

We remark that the material composition at the interior of the battery is periodic in the x_1- coordinate. The layers of cell components in the interior of the battery are homogeneous in the x_2 and x_3 directions. In the $x_2 - x_3$ plane these components can thus be considered as homogeneous sheets, as far as the interior is considered. The battery casing breaks this independence, however. Figure 2.5 illustrates the composition of the battery at a given x_1

value in the $x_2 - x_3$ plane.

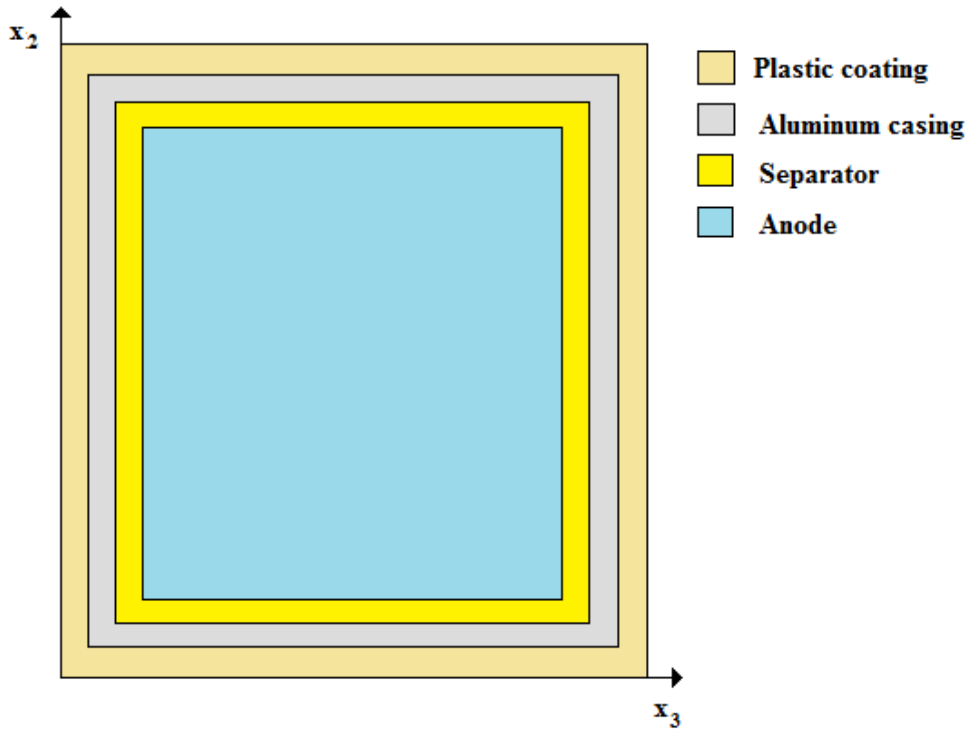

Figure 2.5: Schematic representation of the pouch-cell configuration. The illustration is taken at a given x_1-value in the x_2-x_3 plane. The casing which is wrapped around the battery interior is here composed of an aluminum layer coated with plastic at the outside and coated with the separator material at the inside. The interior of the battery is thus homogeneous in the $x_2 - x_3$ plane. Here, at the illustrated x_1 value, a sheet of an anode constitutes the battery interior.

Based on values found in the literature, totally 24 unit cells are present in the prismatic configuration of the pouch-cell. For the battery interior in the x_1-direction, this yields in total 97 layers consisting of a periodic pattern of electrodes, current collectors and separators. The size and thickness of the battery components are presented in table 2.1.

Table 2.1: Geometric data: Thickness refer to the x_1-direction, length to the x_2-direction and width to the x_3-direction.

Thickness of anode	$9.9 \cdot 10^{-5}$ (m)
Thickness of cathode	$8.0 \cdot 10^{-5}$ (m)
Thickness of Cu current collector	$2.2 \cdot 10^{-5}$ (m)
Thickness of Al current collector	$1.7 \cdot 10^{-5}$ (m)
Thickness of separator	$2.2 \cdot 10^{-5}$ (m)
Thickness of Al-layer in the casing	$11.7 \cdot 10^{-5}$ (m)
Thickness of plastic-layer in the casing	$3.0 \cdot 10^{-5}$ (m)
Width of separator	$1.49 \cdot 10^{-1}$ (m)
Width of anodes	$1.45 \cdot 10^{-1}$ (m)
Length of anodes	$2.35 \cdot 10^{-1}$ (m)
Width of cathodes	$1.40 \cdot 10^{-1}$ (m)
Length of cathodes	$2.34 \cdot 10^{-1}$ (m)
Total thickness	$5.7 \cdot 10^{-3}$ (m)
Thickness of interior	$5.3 \cdot 10^{-3}$ (m)

In this work we neglect the current collector tabs and the edges of the casing that can be observed in figure 2.1. We also neglect the difference in length and width between the electrodes and the separator. Instead we assume that the battery interior has an average length of $2.345 \cdot 10^{-1}$(m) and average with of $1.447 \cdot 10^{-1}$(m). The average quantities are presented in table 2.2. Based on these simplifications, the battery can be represented as a box. This may be an oversimplification however since the current collector tabs are assumed to be made of Ni. They may thus represent significant resistive heating sources that may transmit thermal energy into the battery through the current collectors. However, a model that considers this effect would need to distribute resistive heating effects locally. Modeling resistive heating locally are beyond the scope of this work. Nevertheless, the modeling framework presented here is assumed to be excellent for such extensions.

Table 2.2: Geometric model data: Thickness refer to the x_1-direction, length to the x_2-direction and width to the x_3-direction.

Average width of interior	$1.447 \cdot 10^{-1}$(m)
Average length of interior	$2.345 \cdot 10^{-1}$(m)
Average total length	$2.346 \cdot 10^{-1}$(m)
Average total width	$1.450 \cdot 10^{-1}$(m)
Total thickness	$5.7 \cdot 10^{-3}$ (m)
Thickness of interior	$5.3 \cdot 10^{-3}$ (m)
Average volume of interior	$1.793 \cdot 10^{-4}$(m^3)
Average total volume	$1.192 \cdot 10^{-4}$(m^3)

2.2 Physical Properties

In this section we present the assumed physical properties of the pouch-cell. The anode are assumed to be carbon based and the cathode are assumed to be a $LiNiCoMnO_2$-type. $LiNiCoMnO_2$ is also referred to as NCM.

Table 2.3: Physical properties

Material	ρ (kg/m^3)	C_p (J/kg K)	λ (W/m K)
LiC_6 anode	5032	700	5 [24]
$LiNiCoMnO_2$ cathode	1500	700	5 [24]
Al current collector	2700	870	200 [24]
Cu current collector	9000	381	380 [24]
Separator	1200	700	1 [24]
Al casing	2770	875	177 [8], [7]
Plastic coating (LDPE)	920	2500	0.40 [60]

Table 2.3 presents the physical properties of the different battery components. As in the work by Chen et al. [8], the aluminum casing is assumed to constitute of the alloy 2024-T6 and not pure Al. Thus the thermal conductivity differ from the Al current collector. We also assume that the applied material for the plastic coating is low-density polyethylene (LDPE).

Chapter 3

Thermal Modeling

In this chapter a thermal model is presented. The source term in this model has expressions that are the result of experiments conducted on the pouch-cell. The model is scaled, before homogenization theory is applied. Finally the dimensionless-scaled-homogenized model is summarized.

3.1 Governing Equations

In order to describe the thermal effects inside a battery mathematically, we need to define a region Ω in $\Re^3$ that is occupied by the battery. The corresponding boundary $\partial\Omega$ lies in $\Re^2$. Moreover, the region Ω is the box given by

$$0 < x_i < L_{x_i},\ i = 1, 2, 3$$

where L_{x_1}, L_{x_2} and L_{x_3} are constants measured in (m). Let us also introduce the two regions Ω_1 and Ω_2 that occupy the battery interior and the battery casing, respectively, i.e.

$$\Omega = \Omega_1 \cup \Omega_2 \tag{3.1}$$

Let the inner region Ω_1 occupy the box given by

$$L_{i\Omega_a} < x_i < L_{i\Omega_b},\ i = 1, 2, 3$$

Here $L_{i\Omega_a}$ and $L_{i\Omega_b}$ are constants measured in (m).

Many works are presented on thermal modeling of lithium ion batteries. The most common approach consist of applying a partial differential equation

to describe the thermal energy balance around an arbitrary volume element inside the battery (e.g. [21]), i.e.

$$\rho(\underline{x})C_p(\underline{x})\frac{\partial T(\underline{x},t)}{\partial t} = \nabla\cdot(\lambda(\underline{x})\nabla T(\underline{x},t)) + q(\underline{x},t), \quad \underline{x}\in\Omega, \quad t>0 \tag{3.2}$$

Here ρ denotes the mass density measured in (kg/m^3), C_p is the constant-pressure heat capacity measured in (J/kg K), T represents the temperature field measured in (K), t denotes the time measured in (s), while λ represents the thermal conductivity tensor measured in (W/m K). The rate of heat generated while the battery is charged or discharged is represented by the source term q measured in (W/m^3).

The heat generation in batteries can be related to three separate processes. These are activation heating due to interfacial kinetics, heating from species transport which is concentration driven and resistive heating of charged particles [2]. The literature on thermal modeling of lithium ion batteries differ mainly in the choice of the source term q. A review on different thermal modeling strategies is given in Appendix A. In this work we apply the source term presented by Bernardi et al. [3], i.e.

$$q(\underline{x},t) = \frac{I(t)}{vol(\Omega_1)}(U(t)-V(t)) - \frac{I(t)}{vol(\Omega_1)}T\frac{\partial U}{\partial T}, \quad \underline{x}\in\Omega_1, \quad t\le t_c \tag{3.3}$$

$$q(\underline{x},t) = 0, \quad \underline{x}\in\Omega_1, \quad t>t_c \tag{3.4}$$

$$q(\underline{x},t) = 0, \quad \underline{x}\in\Omega_2, \quad t\ge 0 \tag{3.5}$$

Here $I(t)$ is the total cell current measured in (A) and $vol(\Omega_1)$ represents the volume of the battery interior, measured in (m^3). $U(t)$ and $V(t)$ are the open-circuit and closed-circuit potentials, respectively, both measured in (V). We will model the battery during discharge. Therefore t_c represents the time measured in (s) when the battery current is cut off. The heating effects are obviously not present in the casing of the battery, therefore the source term is zero elsewhere than in the battery interior.

The first term on the right in equation (3.3) represents the heat generation rate due to charge transfer overpotentials at the interfaces, mass transfer limitations and ohmic losses [2]. The second term is related to the entropy of reaction and is referred to as entropic heat [2]. Furthermore $\frac{\partial U}{\partial T}$ is the

entropic heat coefficient [2]. From a thermodynamic perspective the first term represents irreversible effects while the second term corresponds to reversible effects [21]. Details about derivation, assumptions and discussions about a valid modeling regime for this source term are provided in Appendix A.

In this work we will model a 1C discharge at constant current from 100-10% state of charge (SOC). This yields a current of

$$I(t) = 17.5 \text{ (A)}, \quad t \leq t_c \tag{3.6}$$

$$I(t) = 0 \text{ (A)}, \quad t > t_c \tag{3.7}$$

Here the time at end of discharge is $t_c = 3240$ (s). Experiments are conducted to obtain expressions for the difference between the open-circuit and closed-circuit potentials ($U(t) - V(t)$) and for the entropic heat coefficient $\frac{\partial U}{\partial T}$. Experimental details, analysis of experimental results and conclusions of these experiments are given in Appendix B. Here we present the main results of these experiments.

The difference between the open-circuit and closed-circuit potentials is expressed by a time-dependent function $\hat{\alpha}$, i.e.

$$\hat{\alpha}(t) = U(t) - V(t) = a't^3 + b't^2 + c't + d' \tag{3.8}$$

Here a', b', c' and d' are constants measured in (V/s^3), (V/s^2), (V/s) and (V), respectively. These constants are given in table 3.1.

Table 3.1: Polynomial coefficients

$a' =$	$1.3 \cdot 10^{-11}$	(V/s^3)
$b' =$	$-6.461 \cdot 10^{-8}$	(V/s^2)
$c' =$	$9.907361 \cdot 10^{-5}$	(V/s)
$d' =$	$4.51243100 \cdot 10^{-2}$	(V)

The entropic heat coefficient is approximated by a constant $\hat{\beta}$ measured in (V/K), i.e.

$$\frac{\partial U}{\partial T} = \hat{\beta} \tag{3.9}$$

where $\hat{\beta}$ has the following value

$$\hat{\beta} = -2.7 \cdot 10^{-4} \text{ (V/K)}$$

This yields the following expression for the source term 3.3

$$q(\underline{x}, t) = \frac{I(t)}{vol(\Omega_1)}\hat{\alpha}(t) - \frac{I(t)}{vol(\Omega_1)}T\hat{\beta}, \quad \underline{x} \in \Omega_1, \quad t \leq t_c \tag{3.10}$$

Let us define the initial temperature field in the region Ω as T_0. The problem (3.2) then has the following initial condition:

$$T(\underline{x}, 0) = T_0(\underline{x}), \quad \underline{x} \in \Omega \tag{3.11}$$

In order to model the interaction between the ambient air and the battery surface represented by the boundary $\partial\Omega$, we impose a Robin boundary condition to the problem (3.2). We thus neglect the exchange of heat by radiation. The Robin boundary condition is expressed as

$$-\lambda \nabla T \cdot \underline{n} = h(T - g), \quad \underline{x} \in \partial\Omega \tag{3.12}$$

where g is a constant measured in (K) that represents the ambient air temperature. Furthermore are $\underline{n}$ an outward unit normal vector defined on $\partial\Omega$ and h a constant measured in (W/m^{2}K) representing the external heat transfer coefficient.

3.2 Scaling of the Model

In this section, we scale the model problem to obtain a dimensionless form. The region Ω is transformed into the region Γ with the boundary $\partial\Gamma$ by the dimensionless vector $\underline{\xi}$ defined as

$$\underline{\xi} = [\frac{x_1}{L_1}, \frac{x_1}{L_2}, \frac{x_3}{L_3}]$$

Here L_1, L_2 and L_3 are constants measured in (m). The scaled region Γ is given by the box

$$0 < \xi_i < L_{\xi_i}, \ i = 1, 2, 3$$

We observe that by definition,

$$L_{\xi_i} = \frac{L_{x_i}}{L_i}$$

i.e. if

$$L_i = L_{x_i}$$

we have that

$$L_{\xi_i} = 1$$

We also divide the region Γ into the two regions Γ_1 and Γ_2 representing the scaled battery interior and the scaled battery casing, respectively, i.e.

$$\Gamma = \Gamma_1 \cup \Gamma_2 \tag{3.13}$$

Let us furthermore introduce the dimensionless time-variable τ defined as

$$\tau = \frac{t}{t_\tau}$$

Here t_τ is a constant measured in (s). t_τ and L_i are often referred to as characteristic time and length scales, respectively.

3.2.1 Scaling of the PDE

Consider the model equation

$$\rho(\underline{x})C_p(\underline{x})\frac{\partial T(\underline{x},t)}{\partial t} = \nabla \cdot (\lambda(\underline{x})\nabla T(\underline{x},t)) + q(\underline{x},t) \tag{3.14}$$

We now introduce a dimensionless temperature distribution $\hat{u}(\underline{\xi},\tau)$ given by

$$T(\underline{x},t) = A\hat{u}(\underline{\xi},\tau) + B \tag{3.15}$$

Here A and B are constants measured in (K). Furthermore we introduce the dimensionless thermal conductivity tensor Λ defined as

$$\lambda(\underline{x}) = \alpha\Lambda(\underline{\xi})$$

where α is a constant measured in (W/mK). $\Lambda(\underline{\xi})$ is expressed as

$$\Lambda(\underline{\xi}) = \begin{pmatrix} \Lambda_1(\underline{\xi}) & 0 & 0 \\ 0 & \Lambda_2(\underline{\xi}) & 0 \\ 0 & 0 & \Lambda_3(\underline{\xi}) \end{pmatrix} \tag{3.16}$$

Moreover we scale the spatial dependent mass density and specific heat capacity by introducing a dimensionless function f dependent of the variable $\underline{\xi}$, i.e.

$$\rho(\underline{x})C_p(\underline{x}) = Cf(\underline{\xi}) \tag{3.17}$$

Here C is a constant measured in (J/m^3 K). Inserting (3.15)-(3.17) into equation (3.14), applying the chain rule and rearranging we get

$$f\frac{\partial \hat{u}}{\partial \tau} = \frac{t_\tau \alpha}{C} D \cdot (\Lambda D\hat{u}) + \frac{qt_\tau}{AC} \tag{3.18}$$

where D is the differential operator defined as

$$D = [\frac{1}{L_1}\frac{\partial}{\partial \xi_1}, \frac{1}{L_2}\frac{\partial}{\partial \xi_2}, \frac{1}{L_3}\frac{\partial}{\partial \xi_3}] \tag{3.19}$$

Equation (3.18) can also be expressed in terms of the Einstein summation convention, i.e.

$$f\frac{\partial \hat{u}}{\partial \tau} = \frac{t_\tau \alpha}{C}\frac{1}{L_i^2}\frac{\partial}{\partial \xi_i}(\Lambda_i \frac{\partial \hat{u}}{\partial \xi_i}) + \frac{qt_\tau}{AC} \tag{3.20}$$

We now introduce γ_i as

$$\gamma_i = \frac{L_1}{L_i} \tag{3.21}$$

By choosing

$$t_\tau = \frac{CL_1^2}{\alpha}$$

we get

$$\frac{t_\tau \alpha}{CL_1^2} = 1$$

t_τ is referred to as the *diffusion timescale*. Furthermore we define the scaled source term Q as

$$Q = \frac{qL_1^2}{\alpha A} \tag{3.22}$$

This yields the following form for the scaled PDE:

$$f\frac{\partial \hat{u}}{\partial \tau} = \frac{\partial}{\partial \xi_1}(\Lambda_1 \frac{\partial \hat{u}}{\partial \xi_1}) + \gamma_2^2 \frac{\partial}{\partial \xi_2}(\Lambda_2 \frac{\partial \hat{u}}{\partial \xi_2}) + \gamma_3^2 \frac{\partial}{\partial \xi_3}(\Lambda_3 \frac{\partial \hat{u}}{\partial \xi_3}) + Q \tag{3.23}$$

The source term Q in this general model equation needs now to be specified. For this work, we apply the source term presented in section 3.1. We will thus scale the expression (3.10).

We introduce the dimensionless function $J(\tau)$ describing the current as

$$I(t) = iJ(\tau) \tag{3.24}$$

where i is a constant measured in (A). Furthermore we introduce the dimensionless function $\hat{\kappa}(\tau)$ that represents the dimensionless potential difference as

$$\hat{\alpha}(t) = \delta\hat{\kappa}(\tau) \tag{3.25}$$

Here δ is a constant measured in (V). Let the dimensionless constant $\hat{\mu}$ representing the entropic heat coeffient $\hat{\beta}$ be defined as

$$\hat{\beta}(t) = \epsilon\hat{\mu} \tag{3.26}$$

where ϵ is a constant measured in (V/K). We chose $\delta = 1$ and $\epsilon = 1$, it follows that

$$\hat{\kappa}(\tau) = a't_\tau^3\tau^3 + b't_\tau^2\tau^2 + c't_\tau\tau + d' \tag{3.27}$$

and that

$$\hat{\mu} = \hat{\beta} \tag{3.28}$$

We conveniently introduce the constants $\tilde{a} = a't_\tau^3$, $\tilde{b} = b't_\tau^2$, $\tilde{c} = c't_\tau$ and $\tilde{d} = d'$. These constants are measured in (V). $\hat{\kappa}(\tau)$ can then be expressed as

$$\hat{\kappa}(\tau) = \tilde{a}\tau^3 + \tilde{b}\tau^2 + \tilde{c}\tau + \tilde{d} \tag{3.29}$$

The scaled dimensionless source term thus reads

$$Q(\tau, \underline{\xi}) = \frac{L_1^2 iJ}{A\alpha vol(\Omega_1)}(\hat{\kappa} - A\hat{\mu}\hat{u} - B\hat{\mu}), \quad \underline{\xi} \in \Gamma_1, \quad \tau \leq \tau_c, \tag{3.30}$$

$$Q(\tau, \underline{\xi}) = 0, \quad \underline{\xi} \in \Gamma_1, \quad \tau > \tau_c \tag{3.31}$$

$$Q(\tau, \underline{\xi}) = 0, \quad \underline{\xi} \in \Gamma_2, \quad \tau \geq 0, \tag{3.32}$$

Here τ_c is defined as

$$\tau_c = \frac{t_c}{t_\tau} \tag{3.33}$$

thus representing the dimensionless time for which the dimensionless current is cut off. Equation (3.30) can now be written as

$$Q(\tau, \underline{\xi}) = \frac{L_1^2 iJ}{A\alpha vol(\Omega_1)}(\hat{\kappa} - B\hat{\mu}) - \frac{L_1^2 iJ}{\alpha vol(\Omega_1)}\hat{\mu}\hat{u} \tag{3.34}$$

Let us introduce the dimensionless function O defined as

$$O = \frac{L_1^2 iJ}{A\alpha vol(\Omega_1)}(\hat{\kappa} - B\hat{\mu}) \tag{3.35}$$

and the dimensionless function P defined as

$$P = -\frac{L_1^2}{\alpha vol(\Omega_1)} iJ\hat{\mu} \tag{3.36}$$

The scaled dimensionless source term (3.30) can thus be expressed as

$$Q(\tau) = O(\tau) + P(\tau)\hat{u}, \quad \underline{\xi} \in \Gamma_1, \quad \tau \leq \tau_c \tag{3.37}$$

3.2.2 Scaling of the Initial and Boundary Conditions

The initial condition

$$T(\underline{x}, 0) = T_0, \quad \underline{x} \in \Omega \tag{3.38}$$

is scaled by imposing the scaled temperature distribution $T = A\hat{u} + B$ to equation (3.38), i.e.

$$A\hat{u}(\underline{\xi}, 0) + B = T_0 \tag{3.39}$$

By rearranging equation (3.39) we get the scaled initial condition

$$\hat{u}(\underline{\xi}, 0) = \frac{T_0 - B}{A} \tag{3.40}$$

The model problem is equipped with a Robin boundary condition, i.e.

$$-\lambda \nabla T \cdot \underline{n} = h(T - g), \quad \underline{x} \in \partial\Omega \tag{3.41}$$

Imposing the scaled temperature distribution $T = A\hat{u} + B$ and the scaled thermal conductivity tensor $\lambda = \alpha\Lambda$ to the boundary condition yields

$$-A\alpha\Lambda D\hat{u} \cdot \underline{n} = h(A\hat{u} + B - g), \quad \underline{\xi} \in \partial\Gamma \tag{3.42}$$

Here the chain rule is exploited. We conveniently introduce

$$g' = h(g - B)$$

and

$$h' = hA$$

.

It is convenient to choose $B = g$, which yields a simplified Robin boundary condition. It follows that the scaled boundary condition reads

$$h'\hat{u} + A\alpha\Lambda D\hat{u} \cdot \underline{n} = 0, \quad \underline{\xi} \in \partial\Gamma \tag{3.43}$$

3.3 Homogenization Theory

In lithium ion batteries electrochemical and mechanical phenomena occur at both micro and macro-scales. Therefore, homogenization theory has earlier been applied to derive macroscale equations from underlying microscale equations. We refer the reader to the works by Golomon et al. [20], Ciucci and Lai [13] and Zhang [63] for details.

Our contribution consists of applying homogenization theory to a thermal model for lithium ion batteries with prismatic cell geometry.

3.3.1 Homogenization of the Thermal Model

In this section we apply homogenization theory to the partial differential equation (3.23) describing the dimensionless temperature field inside a lithium ion battery. We emphasize that general parabolic problems as the problem (3.23) are successfully homogenized in Persson et al. [45].

The battery occupies the scaled region Γ, where the battery interior occupies the region Γ_1 and the casing of the battery occupies the region Γ_2. Let the region Γ_1 be given by the box

$$L_{i\Gamma_a} < \xi_i < L_{i\Gamma_b}, \ i = 1, 2, 3$$

Here $L_{i\Gamma_a}$ and $L_{i\Gamma_b}$ are dimensionless constants. We observe that the region Γ_1 is a simply connected bounded region with the boundary $\tilde{\Gamma}$. The region Γ_2 is a doubly connected bounded region with the outer boundary $\partial\Gamma$ and the inner boundary $\partial\tilde{\Gamma}$ [33].

The geometry of the battery interior Γ_1 yields a periodic structure in the ξ_1-direction. The period length corresponds to a series of layers in the following order: Positive electrode current collector, cathode, separator, anode, negative electrode current collector, anode, separator, cathode and positive

electrode current collector. We define this series of layers as a unit $Y-$cell. Let the length of a Y-cell in the unscaled region Ω_1 be defined as L_Y.

Furthermore let the respective scaled dimensionless length of a Y-cell in Γ_1 be defined as $L_{Y\xi}$.

We then have the following relation:

$$L_{Y\xi} = \frac{1}{L_1} L_Y \tag{3.44}$$

In this work we refer to functions that are periodic in the interval $L_{Y\xi}$ as Y-periodic functions. Let us introduce the parameter ε which describes the fractional relation between the dimensionless period-length $L_{Y\xi}$ and the dimensionless length of the periodic battery interior in ξ_1-direction $\mid L_{1\Gamma_b} - L_{1\Gamma_a} \mid$, i.e.

$$\varepsilon = \frac{L_{Y\xi}}{\mid L_{1\Gamma_b} - L_{1\Gamma_a} \mid} = \frac{\frac{1}{L_1} L_Y}{\frac{1}{L_1} \mid L_{1\Omega_b} - L_{1\Omega_a} \mid} = \frac{L_Y}{\mid L_{1\Omega_b} - L_{1\Omega_a} \mid} \tag{3.45}$$

We observe that ε is conserved under scaling.

The battery has a so-called prismatic cell geometry which is described in section 2.1. In accordance with the literature (e.g. [8]), we assume that the thermal conductivity, mass density and specific heat capacity are dependent on the spatial coordinates only. By these assumptions the dimensionless thermal conductivity tensor Λ describing the regions Γ_1 and Γ_2 is expressed as:

$$\Lambda(\underline{\xi}) = \begin{pmatrix} \Lambda_1(\underline{\xi}) & 0 & 0 \\ 0 & \Lambda_1(\underline{\xi}) & 0 \\ 0 & 0 & \Lambda_1(\underline{\xi}) \end{pmatrix} \tag{3.46}$$

The thermal conductivity in the interior Γ_1 is only dependent on the ξ_1-coordinate. Moreover, in Γ_1 the thermal conductivity is periodic in the ξ_1 variable, i.e.

$$\Lambda_1(\underline{\xi}) = \begin{pmatrix} \Lambda_1(\underline{\xi}), & \underline{\xi} \in \Gamma_2 \\ \Lambda_1(\xi_1), & \underline{\xi} \in \Gamma_1 \end{pmatrix} \tag{3.47}$$

Furthermore, the dimensionless function f that represents the product of the mass density and the specific heat capacity are dependent on position only. Thus f can be described as

$$f(\underline{\xi}) = \begin{pmatrix} f(\underline{\xi}), & \underline{\xi} \in \Gamma_2 \\ f(\underline{\xi}_1), & \underline{\xi} \in \Gamma_1 \end{pmatrix} \tag{3.48}$$

We also stress that any source term Q should naturally be zero in the region Γ_2, as pointed out in section 3.1.

3.3.2 The Inner Region Γ_1

Here we describe the model problem for the inner region Γ_1. We emphasize that the theory applied in this section is mainly taken from the work by Persson et al. [45]. The periodic properties of the geometry affects certain physical parameters. In general the solution $\hat{u}$ is dependent on these parameters as well. Based upon this, we make the following assumptions:

1. It is convenient to describe the model problem by the parameter ε.

2. Furthermore, the physical parameters and the solution can conveniently be described by a local variable considering the periodicity on a different scale than the scale of the regular spatial variable.

By means of vector notation and 1., the scaled equation (3.23) can be expressed as

$$f^{\varepsilon}\frac{\partial \hat{u}^{\varepsilon}(\underline{\xi},\tau)}{\partial \tau} = D_{\gamma\xi} \cdot (\Lambda^{\varepsilon} D_{\xi} \hat{u}^{\varepsilon}(\underline{\xi},\tau)) + Q \tag{3.49}$$

Here we tacitly have introduced the operators $D_{\gamma\xi}$ and D_{ξ} defined as

$$D_{\gamma\xi} = [\frac{\partial}{\partial \xi_1}, \gamma_2^2 \frac{\partial}{\partial \xi_2}, \gamma_3^2 \frac{\partial}{\partial \xi_3}] \tag{3.50}$$

and

$$D_{\xi} = [\frac{\partial}{\partial \xi_1}, \frac{\partial}{\partial \xi_2}, \frac{\partial}{\partial \xi_3}] \tag{3.51}$$

respectively.

2. leads to the following assumptions:

$$\Lambda_1^{\varepsilon}(\xi_1) = \Lambda(\frac{\xi_1}{\varepsilon}) \tag{3.52}$$

$$f^{\varepsilon}(\xi_1) = f(\frac{\xi_1}{\varepsilon}) \tag{3.53}$$

$$\hat{u}^{\varepsilon}(\underline{\xi},\tau) = \hat{u}(\underline{\xi},\frac{\xi_1}{\varepsilon},\tau) \tag{3.54}$$

The thermal conductivity tensor then reads

$$\Lambda(\frac{\xi_1}{\varepsilon}) = \begin{pmatrix} \Lambda_1(\frac{\xi_1}{\varepsilon}) & 0 & 0 \\ 0 & \Lambda_1(\frac{\xi_1}{\varepsilon}) & 0 \\ 0 & 0 & \Lambda_1(\frac{\xi_1}{\varepsilon}) \end{pmatrix} \tag{3.55}$$

Furthermore we introduce the local variable y defined as

$$y = \frac{1}{\varepsilon}\xi_1 \tag{3.56}$$

As stated above, we will refer to functions that are periodic in the variable y as $Y-$periodic functions. It follows directly that the thermal conductivity tensor can be described as

$$\Lambda(y) = \begin{pmatrix} \Lambda_1(y) & 0 & 0 \\ 0 & \Lambda_1(y) & 0 \\ 0 & 0 & \Lambda_1(y) \end{pmatrix} \tag{3.57}$$

Now, when we consider $D_{\xi}\hat{u}^{\varepsilon}$, we have that

$$D_{\xi}\hat{u}^{\varepsilon}(\underline{\xi},\tau) = D_{\xi}\hat{u}(\underline{\xi},y,\tau) + \frac{1}{\varepsilon}\frac{\partial\hat{u}(\underline{\xi},y,\tau)}{\partial y}\underline{i} = D'_{\xi}\hat{u} \tag{3.58}$$

by the chain rule. Here we tacitly have introduced the operator D'_{ξ} defined as $D_{\xi} + \frac{1}{\varepsilon}\frac{\partial}{\partial y}\underline{i}$, where $\underline{i}$ denotes the unit vector in the ξ_1-direction. Writing out the first term on the right side of equation (3.49) yields

$$\begin{aligned} D_{\gamma\xi}\cdot(\Lambda^{\varepsilon}D_{\xi}\hat{u}^{\varepsilon}) = (\frac{\partial}{\partial\xi_1},\gamma_2^2\frac{\partial}{\partial\xi_2},\gamma_3^2\frac{\partial}{\partial\xi_3})\cdot(\Lambda D'_{\xi}\hat{u}) = \\ (\frac{\partial}{\partial\xi_1},\gamma_2^2\frac{\partial}{\partial\xi_2},\gamma_3^2\frac{\partial}{\partial\xi_3})\cdot\begin{pmatrix} \Lambda_1(\frac{\partial\hat{u}}{\partial\xi_1}+\frac{1}{\varepsilon}\frac{\partial\hat{u}}{\partial y}) \\ \Lambda_1\frac{\partial\hat{u}}{\partial\xi_2} \\ \Lambda_1\frac{\partial\hat{u}}{\partial\xi_3} \end{pmatrix} \end{aligned} \tag{3.59}$$

Exploiting the chain rule gives the following result:

$$\begin{aligned} D_{\gamma\xi}\cdot(\Lambda^{\varepsilon}D_{\xi}\hat{u}^{\varepsilon}) = \frac{1}{\varepsilon^2}\frac{\partial}{\partial y}(\Lambda_1\frac{\partial\hat{u}}{\partial y}) + \frac{1}{\varepsilon}(\Lambda_1\frac{\partial^2\hat{u}}{\partial\xi_1\partial y} + \frac{\partial}{\partial y}(\Lambda_1\frac{\partial\hat{u}}{\partial\xi_1}))+ \\ \frac{1}{\varepsilon^0}(\Lambda_1\frac{\partial^2\hat{u}}{\partial\xi_1^2} + \gamma_2^2\Lambda_1\frac{\partial^2\hat{u}}{\partial\xi_2^2} + \gamma_3^2\Lambda_1\frac{\partial^2\hat{u}}{\partial\xi_3^2}) \end{aligned} \tag{3.60}$$

We now introduce the three following operators:

$$A_0 = \frac{\partial}{\partial y}(\Lambda_1 \frac{\partial}{\partial y}) \tag{3.61}$$

$$A_1 = (\Lambda_1 \frac{\partial^2}{\partial \xi_1 \partial y} + \frac{\partial}{\partial y}(\Lambda_1 \frac{\partial}{\partial \xi_1})) \tag{3.62}$$

$$A_2 = \Lambda_1 \frac{\partial^2}{\partial \xi_1^2} + \gamma_2^2 \Lambda_1 \frac{\partial^2}{\partial \xi_2^2} + \gamma_3^2 \Lambda_1 \frac{\partial^2}{\partial \xi_3^2} \tag{3.63}$$

It follows that equation (3.49) can be expressed as

$$f \frac{\partial \hat{u}}{\partial \tau} = \varepsilon^{-2} A_0 \hat{u} + \varepsilon^{-1} A_1 \hat{u} + \varepsilon^0 A_2 \hat{u} + Q \tag{3.64}$$

Furthermore we assume that the solution can be represented by an asymptotic expansion of functions w_i that are periodic in the variable y, i.e.

$$\hat{u}(\underline{\xi}, y, \tau) = \sum_{i=0}^{\infty} \varepsilon^i w_i(\underline{\xi}, y, \tau) \tag{3.65}$$

Inserting (3.65) into (3.64) and equating terms of equal order in ε yields the following three lowest order equations (i.e. terms with ε^{-2}, ε^{-1} and ε^0, respectively):

$$A_0 w_0 = 0 \tag{3.66}$$

$$A_0 w_1 + A_1 w_0 = 0 \tag{3.67}$$

$$f \frac{\partial w_0}{\partial \tau} = A_0 w_2 + A_1 w_1 + A_2 w_0 + Q \tag{3.68}$$

In order to solve the hierarchy (3.66)-(3.68) we make use of the following Lemma (see Persson et al. [45]):

Lemma 3.3.1. *For the boundary value problem*

$$A_0\Phi = F, \text{ in a unit } Y - cell,$$

where Φ is Y-periodic and F belongs to $L^2(L_{Y\xi})$, we have that:

- *There exists a weak Y-periodic solution Φ if and only if $\langle F \rangle = 0$.*
- *If there exists a weak Y-periodic solution Φ, then it is unique up to an additive constant.*

Here $\langle F \rangle$ is defined as $\langle F \rangle \equiv \frac{1}{meas(L_{Y\xi})} \int_{L_{Y\xi}} F dy$, where $meas(L_{Y\xi})$ is the so-called Lebesgue measure of $L_{Y\xi}$.

Furthermore $L^2(L_{Y\xi})$ is the space defined as $\{F : \int_{L_{Y\xi}} |F|^2 dx < \infty\}$, with the norm $\|F\|_{L^2} = (\int_{L_{Y\xi}} |F|^2 dx)^{1/2}$

By Lemma 3.3.1, there exists a weak $Y-$periodic solution w_0 to equation (3.66). Furthermore, this solution is unique up to an additive constant. The trivial solution $w_0 = 0$ clearly fulfills equation (3.66). Since this solution also can be considered as periodic in the variable y, the trivial solution is unique up to a constant. Therefore the unique solution to (3.66) is given by

$$w_0(\underline{\xi}, y, \tau) = z(\underline{\xi}, \tau) \tag{3.69}$$

Furthermore, if we insert the solution w_0 into equation (3.67), we obtain the following problem

$$A_0 w_1 = -A_1 z = -\frac{d\Lambda_1(y)}{dy} \frac{\partial z(\underline{\xi}, \tau)}{\partial \xi_1} \tag{3.70}$$

By Lemma 3.3.1 the existence of a periodic solution to the problem (3.70) is guaranteed. Furthermore, by the same Lemma, this solution is unique up to an additive constant. When assuming that the solution can be represented by

$$w_1(\underline{\xi}, y, \tau) = \Phi(\underline{\xi}, \tau)\chi(y) \tag{3.71}$$

the problem (3.70) can be expressed as

$$\Phi(\underline{\xi}, \tau) A_0 \chi(y) = -\frac{d\Lambda_1(y)}{dy} \frac{\partial z(\underline{\xi}, \tau)}{\partial \xi_1} \tag{3.72}$$

By separation of variables, we obtain

$$\Phi(\underline{\xi},\tau) = \frac{\partial z}{\partial \xi_1} \tag{3.73}$$

By substitution of (3.73) into (3.72) we obtain the so-called cell problem, i.e.

$$A_0\chi(y) = -\frac{d\Lambda_1(y)}{dy} \tag{3.74}$$

Since $\Phi(\underline{\xi},\tau)$ is known, by the solution of the cell problem, we obtain a solution w_1 to (3.70) that is unique up to the additive arbitrary constant $z_1(\underline{\xi},\tau)$, i.e.

$$w_1(\underline{\xi},y,\tau) = \frac{\partial z(\underline{\xi},\tau)}{\partial \xi_1}\chi(y) + z_1(\underline{\xi},\tau) \tag{3.75}$$

We now consider the problem (3.68). For w_2 to be a unique solution, by Lemma 3.3.1, the following equation must hold:

$$\langle f\frac{\partial z}{\partial \tau}\rangle = \langle A_2 z\rangle + \langle A_1(\frac{\partial z}{\partial \xi_1}\chi)\rangle + \langle A_1 z_1\rangle + \langle Q\rangle \tag{3.76}$$

Here we tacitly have substituted the expressions for the solutions w_0 and w_1. By Gauss' theorem, the third term on the right in equation (3.76) is zero. Furthermore the second term can be expressed as

$$\langle A_1(\frac{\partial z}{\partial \xi_1}\chi)\rangle = \langle \frac{\partial}{\partial \xi_1}(\Lambda_1\frac{\partial}{\partial y}(\frac{\partial z}{\partial \xi_1}\chi))\rangle + \langle \frac{\partial}{\partial y}(\Lambda_1\frac{\partial}{\partial \xi_1}(\frac{\partial z}{\partial \xi_1}\chi))\rangle \tag{3.77}$$

The second term of equation (3.77) vanishes by Gauss' theorem, hence

$$\langle A_1(\frac{\partial z}{\partial \xi_1}\chi)\rangle = \frac{\partial^2 z}{\partial \xi_1^2}\langle \Lambda_1\frac{d\chi}{dy}\rangle \tag{3.78}$$

By these findings, the following equation must hold for in order w_2 to be a $Y-$periodic solution to the problem (3.68):

$$\langle f\rangle\frac{\partial z}{\partial \tau} = \langle \Lambda_1 + \Lambda_1\frac{d\chi}{dy}\rangle\frac{\partial^2 z}{\partial \xi_1^2} + \langle \Lambda_1\rangle\gamma_2^2\frac{\partial^2 z}{\partial \xi_2^2} + \langle \Lambda_1\rangle\gamma_3^2\frac{\partial^2 z}{\partial \xi_3^2} + \langle Q\rangle \tag{3.79}$$

where we tacitly have written out $A_2 z$. By means of vector notation, we get the following homogenized equation

$$\langle f\rangle \frac{\partial z}{\partial \tau} = D_{\gamma\xi} \cdot (\Lambda^{hom} D_\xi z) + \langle Q\rangle \tag{3.80}$$

where we have introduced the homogenized thermal conductivity tensor Λ^{hom} defined as

$$\Lambda^{hom} = \begin{pmatrix} \langle \Lambda_1 + \Lambda_1 \frac{d\chi}{dy}\rangle & 0 & 0 \\ 0 & \langle \Lambda_1 \rangle & 0 \\ 0 & 0 & \langle \Lambda_1 \rangle \end{pmatrix} \tag{3.81}$$

We observe that

$$\langle \Lambda_1 + \Lambda_1 \frac{d\chi}{dy}\rangle = \langle \Lambda_1 (1 + \frac{d\chi}{dy})\rangle \tag{3.82}$$

Furthermore, let us express the cell-problem (3.74) as

$$\frac{d}{dy}((\Lambda_1 \frac{d\chi}{dy}) + \Lambda_1) = 0 \tag{3.83}$$

Taking the indefinite integral with respect to y yields

$$\Lambda_1 \frac{d\chi}{dy} + \Lambda_1 + C_1 = 0 \tag{3.84}$$

where C_1 is an arbitrary integration constant. From equation (3.84) we can express $(1 + \frac{d\chi}{dy})$ as

$$(1 + \frac{d\chi}{dy}) = -\frac{C_1}{\Lambda_1} \tag{3.85}$$

Substituting this expression into equation (3.82) results in

$$\langle \Lambda_1 + \Lambda_1 \frac{d\chi}{dy}\rangle = \langle \Lambda_1 (-\frac{C_1}{\Lambda_1})\rangle = \langle -C_1\rangle = -C_1 \tag{3.86}$$

Let us integrate equation (3.85) over the interval $L_{Y\xi}$ with respect to y. The result is

$$\int_{L_{Y\xi}} dy = -\int_{L_{Y\xi}} \frac{C_1}{\Lambda_1} dy \tag{3.87}$$

where $\int_{L_{Y\xi}} \frac{d\chi}{dy} dy = 0$ by Gauss' theorem. Dividing both sides of equation (3.87) by $meas(L_{Y\xi})$ results in

$$\frac{1}{meas(L_{Y\xi})} \int_{L_{Y\xi}} dy = -\frac{1}{meas(L_{Y\xi})} \int_{L_{Y\xi}} \frac{C_1}{\Lambda_1} dy \tag{3.88}$$

The result is that

$$\langle -\frac{C_1}{\Lambda_1} \rangle = 1 \tag{3.89}$$

Furthermore we have that

$$-C_1 = \langle \Lambda_1^{-1} \rangle^{-1} \tag{3.90}$$

We substitute (3.90) into (3.86), i.e.

$$\langle \Lambda_1 + \Lambda_1 \frac{d\chi}{dy} \rangle = \langle \Lambda_1^{-1} \rangle^{-1} \tag{3.91}$$

To summarize, the homogenized thermal conductivity coefficient $\langle \Lambda_1^{-1} \rangle^{-1}$ can be expressed as

$$\langle \Lambda_1^{-1} \rangle^{-1} = \frac{1}{\frac{1}{meas(Y)} \int_{L_{Y\xi}} \frac{1}{\Lambda_1} dy} \tag{3.92}$$

By (3.91), the homogenized thermal conductivity tensor thus reads

$$\Lambda^{hom} = \begin{pmatrix} \langle \Lambda_1^{-1} \rangle^{-1} & 0 & 0 \\ 0 & \langle \Lambda_1 \rangle & 0 \\ 0 & 0 & \langle \Lambda_1 \rangle \end{pmatrix} \tag{3.93}$$

3.3.3 The Outer Region Γ_2

The equation describing the outer region Γ_2 is given by the scaled equation (3.23). By means of vector notation the model problem for region Γ_2 reads

$$f \frac{\partial \hat{u}(\underline{\xi}, \tau)}{\partial \tau} = D_{\gamma\xi} \cdot (\Lambda D_\xi \hat{u}(\underline{\xi}, \tau)), \quad \underline{\xi} \in \Gamma_2 \tag{3.94}$$

where the corresponding scaled thermal conductivity tensor Λ is expressed as follows:

$$\Lambda = \begin{pmatrix} \Lambda_1(\underline{\xi}) & 0 & 0 \\ 0 & \Lambda_1(\underline{\xi}) & 0 \\ 0 & 0 & \Lambda_1(\underline{\xi}) \end{pmatrix} \tag{3.95}$$

Moreover the function f is defined as

$$f = f(\underline{\xi}) \tag{3.96}$$

3.3.4 Initial and Boundary Conditions

The scaled initial condition (3.40) must hold for the regions Γ_1 and Γ_2. However, for the region Γ_1, we have that $\hat{u} = \sum_i^\infty \varepsilon^i w_i$. The corresponding initial condition for the homogenized problem thus reads

$$z(\underline{\xi}, 0) = \frac{T_0 - B}{A}, \quad \underline{\xi} \in \Gamma_1 \tag{3.97}$$

For the region Γ_2 the initial condition reads

$$\hat{u}(\underline{\xi}, 0) = \frac{T_0 - B}{A}, \quad \underline{\xi} \in \Gamma_2 \tag{3.98}$$

At the interface between Γ_1 and Γ_2, defined as $\partial\tilde{\Gamma}$ the flux-density of the thermal energy must be pointwise continuous, i.e.

$$\Lambda^{hom} Dz \cdot \underline{n_1} = \Lambda D\hat{u} \cdot \underline{n_2}, \quad \underline{\xi} \in \partial\tilde{\Gamma} \tag{3.99}$$

Here $\underline{n_1}$ and $\underline{n_2}$ are the outer unit normal vectors defined at the boundary $\partial\tilde{\Gamma}$. We remark that the two unit normal vectors have the opposite direction.

The scaled Robin boundary condition is imposed to the problem (3.94), i.e.

$$h'\hat{u} + A\alpha\Lambda D\hat{u} \cdot \underline{n} = 0, \quad \underline{\xi} \in \partial\Gamma \tag{3.100}$$

3.4 Summary

In this section the results of the scaled-dimensionless-homogenized thermal model for the lithium ion battery are summarized. The governing equations are:

$$\langle f\rangle \frac{\partial z}{\partial \tau} = D_{\gamma\xi} \cdot (\Lambda^{hom} D_\xi z) + \langle Q\rangle, \quad \underline{\xi} \in \Gamma_1 \tag{3.101}$$

$$f \frac{\partial \hat{u}}{\partial \tau} = D_{\gamma\xi} \cdot (\Lambda D_\xi \hat{u}), \quad \underline{\xi} \in \Gamma_2 \tag{3.102}$$

$$z(\underline{\xi}, 0) = \frac{T_0 - B}{A}, \quad \underline{\xi} \in \Gamma_1 \tag{3.103}$$

$$\hat{u}(\underline{\xi}, 0) = \frac{T_0 - B}{A}, \quad \underline{\xi} \in \Gamma_2 \tag{3.104}$$

$$\Lambda^{hom} Dz \cdot \underline{n_1} = \Lambda D\hat{u} \cdot \underline{n_2}, \quad \underline{\xi} \in \partial\tilde{\Gamma} \tag{3.105}$$

$$h'\hat{u} + A\frac{1}{L_1}\alpha\Lambda D_{\gamma\xi}\hat{u} \cdot \underline{n} = 0, \quad \underline{\xi} \in \partial\Gamma \tag{3.106}$$

The homogenized thermal conductivity tensor is expressed as:

$$\Lambda^{hom} = \begin{pmatrix} \langle \Lambda_1^{-1}\rangle^{-1} & 0 & 0 \\ 0 & \langle \Lambda_1\rangle & 0 \\ 0 & 0 & \langle \Lambda_1\rangle \end{pmatrix} \tag{3.107}$$

This is the outcome of the requirement of existence of periodic solutions to the lowest order equations of the asymptotic expansion in the microvariable y. We emphasize that the result (3.107) is similar as the result obtained by applying a thermal equivalent-resistance approach. This approach estimates thermal resistances for parallel and series coupling of thermal resistors [7]. Such equivalent expressions are introduced in thermal models of lithium ion batteries by e.g. Chen et al. [8]. We remark that the assumption of an asymptotic expansion representation of the solution to the partial differential equation leads to, in the lowest orders of correction, the expression also applied in thermal engineering. This illustrates the beauty and power of mathematical theories.

As a final remark we observe that if the source term Q exhibit a periodic behavior, one can assume that it can be represented by an asymptotic expansion, i.e.

$$Q(\underline{\xi},\tau) = \sum_{i=0}^{\infty} \varepsilon^i Q_i(\underline{\xi}, y, \tau) \tag{3.108}$$

Here Q_i are $Y-$periodic functions. As a result of this expansion the lowest order approximation of the asymptotic expansion of Q (i.e. Q_0) shall appear instead of Q in equation (3.101). In this manner homogenization theory may serve as a powerful tool as an alternative justification of the simplifications of the more local source terms described in the literature. It may even extend the limits for the modeling regime for these simplified expressions. A further analysis in this direction is beyond the scope of this thesis, however.

Chapter 4

Variational Formulation

In this chapter we will bring the scaled-dimensionless-homogenized problem over to variational formulation. This is done in order to solve the problem numerically by means of the finite element method. We will first present a continuous variational formulation, however.

4.1 Continuous Variational Formulation

In this section we express the two partial differential equations on differential form that describes the dimensionless temperature field in each of the regions Γ_1 and Γ_2 as a variational problem for the whole region Γ. The dimensionless temperature distribution of the region Γ is described by the two following equations:

$$\langle f \rangle \frac{\partial \hat{u}}{\partial \tau} = D_{\gamma\xi} \cdot (\Lambda^{hom} D_\xi \hat{u}) + \langle Q \rangle, \quad \underline{\xi} \in \Gamma_1 \tag{4.1}$$

$$f \frac{\partial \hat{u}}{\partial \tau} = D_{\gamma\xi} \cdot (\Lambda D_\xi \hat{u}), \quad \underline{\xi} \in \Gamma_2 \tag{4.2}$$

In addition, we have the initial and boundary conditions, i.e.

$$\hat{u}(\underline{\xi}, 0) = \frac{T_0 - B}{A}, \quad \underline{\xi} \in \Gamma_1 \tag{4.3}$$

$$\hat{u}(\underline{\xi}, 0) = \frac{T_0 - B}{A}, \quad \underline{\xi} \in \Gamma_2 \tag{4.4}$$

$$h' \hat{u} + A \frac{1}{L_1} \alpha \Lambda D_{\gamma\xi} \hat{u} \cdot \underline{n} = 0, \quad \underline{\xi} \in \partial\Gamma \tag{4.5}$$

Here we tacitly have replaced the operator D with $\frac{1}{L_1}D_{\gamma\xi}$. We also replace the solution z with $\hat{u}$ in order to have the same notation for the solution in both of the regions Γ_1 and Γ_2.

We now multiply equations (4.1) and (4.2) by a test function $\hat{v}(\underline{\xi})$ and integrate over the respective regions, i.e.

$$\langle f \rangle \int_{\Gamma_1} \frac{\partial \hat{u}}{\partial \tau} \hat{v} d\Gamma_1 = \int_{\Gamma_1} D_{\gamma\xi} \cdot (\Lambda^{hom} D_\xi \hat{u}) \hat{v} d\Gamma_1 + \int_{\Gamma_1} \langle Q \rangle \hat{v} d\Gamma_1 \tag{4.6}$$

$$\int_{\Gamma_2} f \frac{\partial \hat{u}}{\partial \tau} \hat{v} d\Gamma_2 = \int_{\Gamma_2} D_{\gamma\xi} \cdot (\Lambda D_\xi \hat{u}) \hat{v} d\Gamma_2 d\Gamma_2 \tag{4.7}$$

By applying Green's Lemma on the first term on the left in the equations (4.6) and (4.7), we get

$$\langle f \rangle \int_{\Gamma_1} \frac{\partial \hat{u}}{\partial \tau} \hat{v} d\Gamma_1 = \oint_{\partial \tilde{\Gamma}} (\Lambda^{hom} D_{\gamma\xi} \hat{u}) \hat{v} \cdot \underline{n_1} dA - \int_{\Gamma_1} (\Lambda^{hom} D_{\gamma\xi} \hat{u}) \cdot (D_\xi \hat{v}) d\Gamma_2 + \int_{\Gamma_1} \langle Q \rangle \hat{v} d\Gamma_1 \tag{4.8}$$

and

$$\int_{\Gamma_2} f \frac{\partial \hat{u}}{\partial \tau} \hat{v} d\Gamma_2 = \oint_{\partial \tilde{\Gamma}} (\Lambda D_{\gamma\xi} \hat{u}) \hat{v} \cdot \underline{n_2} dA + \oint_{\partial \Gamma} (\Lambda D_{\gamma\xi} \hat{u}) \hat{v} \cdot \underline{n} dA - \int_{\Gamma_2} (\Lambda D_{\gamma\xi} \hat{u}) \cdot (D_\xi \hat{v}) d\Gamma_2 \tag{4.9}$$

We now add equation (4.8) and (4.9), i.e.

$$\begin{aligned} \langle f \rangle \int_{\Gamma_1} \frac{\partial \hat{u}}{\partial \tau} \hat{v} d\Gamma_1 + \int_{\Gamma_2} f \frac{\partial \hat{u}}{\partial \tau} \hat{v} d\Gamma_2 = \\ \oint_{\partial \tilde{\Gamma}} (\Lambda^{hom} D_{\gamma\xi} \hat{u}) \hat{v} \cdot \underline{n_1} dA - \int_{\Gamma_1} (\Lambda^{hom} D_{\gamma\xi} \hat{u}) \cdot (D_\xi \hat{v}) d\Gamma_2 \\ + \int_{\Gamma_1} \langle Q \rangle \hat{v} d\Gamma_1 + \oint_{\partial \tilde{\Gamma}} (\Lambda D_{\gamma\xi} \hat{u}) \hat{v} \cdot \underline{n_2} dA + \oint_{\partial \Gamma} (\Lambda D_{\gamma\xi} \hat{u}) \hat{v} \cdot \underline{n} dA \\ - \int_{\Gamma_2} (\Lambda D_{\gamma\xi} \hat{u}) \cdot (D_\xi \hat{v}) d\Gamma_2 \end{aligned} \tag{4.10}$$

By requiring a pointwise continuity of the flux-density and the test function $\hat{v}$ on every point at the interface $\partial\tilde{\Gamma}$ we have that

$$\begin{aligned}\langle f\rangle \int_{\Gamma_1} \frac{\partial \hat{u}}{\partial \tau}\hat{v}d\Gamma_1 + \int_{\Gamma_2} f\frac{\partial \hat{u}}{\partial \tau}\hat{v}d\Gamma_2 = \\ - \int_{\Gamma_1} (\Lambda^{hom} D_{\gamma\xi}\hat{u})\cdot(D_\xi \hat{v})d\Gamma_2 \\ + \int_{\Gamma_1}\langle Q\rangle \hat{v}d\Gamma_1 + \oint_{\partial\Gamma}(\Lambda D_{\gamma\xi}\hat{u})\hat{v}\cdot\underline{n}dA \\ - \int_{\Gamma_2}(\Lambda D_{\gamma\xi}\hat{u})\cdot(D_\xi\hat{v})d\Gamma_2 \quad (4.11)\end{aligned}$$

Inserting the Robin boundary condition yields

$$\begin{aligned}\langle f\rangle \int_{\Gamma_1} \frac{\partial \hat{u}}{\partial \tau}\hat{v}d\Gamma_1 + \int_{\Gamma_2} f\frac{\partial \hat{u}}{\partial \tau}\hat{v}d\Gamma_2 = \\ - \int_{\Gamma_1} (\Lambda^{hom} D_{\gamma\xi}\hat{u})\cdot(D_\xi \hat{v})d\Gamma_2 - \int_{\Gamma_2}(\Lambda D_{\gamma\xi}\hat{u})\cdot(D_\xi\hat{v})d\Gamma_2 \\ - \frac{L_1}{A\alpha}\oint_{\partial\Gamma}(h'\hat{u})\hat{v}dA + \int_{\Gamma_1}\langle Q\rangle\hat{v}d\Gamma_1 \quad (4.12)\end{aligned}$$

Inserting the expressions for the scaled source term Q represented by the equations (3.31), (3.32) and (3.37) from section 3.2.1 to specify a real modeling example yields

$$\begin{aligned}\langle f\rangle \int_{\Gamma_1} \frac{\partial \hat{u}}{\partial \tau}\hat{v}d\Gamma_1 + \int_{\Gamma_2} f\frac{\partial \hat{u}}{\partial \tau}\hat{v}d\Gamma_2 + \int_{\Gamma_1}(\Lambda^{hom} D_{\gamma\xi}\hat{u})\cdot(D_\xi\hat{v})d\Gamma_1 \\ + \int_{\Gamma_2}(\Lambda D_{\gamma\xi}\hat{u})\cdot(D_\xi\hat{v})d\Gamma_2 - P\int_{\Gamma_1}\hat{u}\hat{v}d\Gamma_1 \\ + \frac{L_1 h'}{A\alpha}\oint_{\partial\Gamma}\hat{u}\hat{v}dA = O\int_{\Gamma_1}\hat{v}d\Gamma_1 \quad (4.13)\end{aligned}$$

Introduce the bilinear form $a : \hat{X}\times\hat{X}' \to \Re$ defined as

$$a(\hat{u},\hat{v}) = \langle f \rangle \int_{\Gamma_1} \frac{\partial \hat{u}}{\partial \tau}\hat{v}d\Gamma_1 + \int_{\Gamma_2} f\frac{\partial \hat{u}}{\partial \tau}\hat{v}d\Gamma_2 + \int_{\Gamma_1} (\Lambda^{hom} D_{\gamma\xi}\hat{u}) \cdot (D_\xi \hat{v})d\Gamma_1 + \int_{\Gamma_2} (\Lambda D_{\gamma\xi}\hat{u}) \cdot (D_\xi \hat{v})d\Gamma_2 - P\int_{\Gamma_1} \hat{u}\hat{v}d\Gamma_1 + \frac{L_1 h'}{A\alpha}\oint_{\partial\Gamma} \hat{u}\hat{v}dA \quad (4.14)$$

and the linear form f: $\hat{X}' \to \Re$ defined as

$$f(\hat{v}) = O\int_{\Gamma_1} \hat{v}d\Gamma_1 \quad (4.15)$$

The variational problem is as follows: Find $\hat{u} \in \hat{X}$ such that

$$a(\hat{u},\hat{v}) = f(\hat{v}), \quad \forall \hat{v} \in \hat{X}' \quad (4.16)$$

holds for appropriate function spaces $\hat{X}$ and $\hat{X}'$.

4.2 Discrete Variational Formulation

In this section we discretize the variational problem (4.16) in section 4.1. We first replace the time derivative by a finite difference approximation, then we choose discrete function spaces X and X' for the trial and test functions, respectively. We start by restricting the time dependent functions $\hat{u}$, O and P in equation (4.16) to be represented only at discrete points in time $\tau = \tau_k$, i.e.

$$\hat{u}(\underline{\xi},\tau) \to \hat{u}(\underline{\xi},\tau_k), \quad k = \{0,1,2,3,...\}$$

$$O(\tau) \to O(\tau_k), \quad k = \{0,1,2,3,...\}$$

$$P(\tau) \to P(\tau_k), \quad k = \{0,1,2,3,...\}$$

We conveniently introduce the notation $\hat{u}^k$, O^k and P^k to represent $\hat{u}(\underline{\xi},\tau_k)$, $O(\tau_k)$ and $P(\tau_k)$, respectively. Simultaneously, we must replace the time derivative which is not defined in the discrete variable τ_k. Let us introduce the distance between the two points in time τ_k and τ_{k+1} as

$$\Delta\tau = \tau_{k+1} - \tau_k$$

The first order time derivative is replaced by a flexible finite difference approximation referred to as the θ-rule [35]. The θ-rule yields either a forward Euler, backward Euler or a Crank-Nicolson scheme for a θ-value of 0, 1 or 1/2, respectively.

Furthermore we introduce finite-dimensional function spaces defined as X and X' for the trial and test functions defined as u^k and v, respectively, i.e.

$$\hat{X} \to X$$

$$\hat{X}' \to X'$$

$$\hat{u}^k \to u^k$$

$$\hat{v} \to v$$

The spaces X and X' are specified by the choice of finite element space in the implementation section.

As a result of this discretization we may now introduce the bilinear form $a : X \times X' \to \Re$ defined as

$$\begin{aligned} a(u^k, v) = \\ \langle f \rangle \int_{\Gamma_1} u^k v d\Gamma_1 + \int_{\Gamma_2} f u^k v d\Gamma_2 + \theta \Delta\tau \int_{\Gamma_1} (\Lambda^{hom} D_{\gamma\xi} u^k) \cdot (D_\xi v) d\Gamma_1 \\ - \theta \Delta\tau P^k \int_{\Gamma_1} u^k v d\Gamma_1 + \theta \Delta\tau \int_{\Gamma_2} (\Lambda D_{\gamma\xi} u^k) \cdot (D_\xi v) d\Gamma_2 \\ + \frac{\theta \Delta\tau L_1 h'}{A\alpha} \oint_{\partial\Gamma} u^k v dA \end{aligned} \quad (4.17)$$

and the linear form $f : X' \to \Re$ defined as

$$
\begin{aligned}
f(v) = & \\
& \langle f \rangle \int_{\Gamma_1} u^{k-1} v d\Gamma_1 + \int_{\Gamma_2} f u^{k-1} v d\Gamma_2 \\
& - (1-\theta)\Delta\tau \int_{\Gamma_1} (\Lambda^{hom} D_{\gamma\xi} u^{k-1}) \cdot (D_\xi v) d\Gamma_1 \\
& + \theta\Delta\tau O^k \int_{\Gamma_1} v d\Gamma_1 + (1-\theta)\Delta\tau O^{k-1} \int_{\Gamma_1} v d\Gamma_1 \\
& + (1-\theta)\Delta\tau P^{k-1} \int_{\Gamma_1} u^{k-1} v d\Gamma_1 \\
& - (1-\theta)\Delta\tau \int_{\Gamma_2} (\Lambda D_{\gamma\xi} u^{k-1}) \cdot (D_\xi v) d\Gamma_2 \\
& - \frac{(1-\theta)\Delta\tau L_1 h'}{A\alpha} \oint_{\partial\Gamma} u^{k-1} v dA \quad (4.18)
\end{aligned}
$$

We can then express the following discrete variational formulation:

Find $u^k \in X$ such that

$$a(u^k, v) = f(v), \quad \forall \hat{v} \in X' \tag{4.19}$$

holds for appropriate function spaces X and X'.

The problem (4.19) can be solved by inserting the unknown at the previous timestep u^{k-1} and solve each variational problem in a loop over all timesteps. The discrete expression for the very first timestep u^0 can be obtained from the variational formulation of the initial condition, i.e.

$$\int_{\Gamma_1} u^0 v d\Gamma_1 + \int_{\Gamma_2} u^0 v d\Gamma_2 = \int_{\Gamma_1} \frac{T_0 - B}{A} v d\Gamma_1 + \int_{\Gamma_2} \frac{T_0 - B}{A} v d\Gamma_2 \tag{4.20}$$

We conveniently introduce the bilinear form $a_0 : X \times X' \to \Re$ defined as

$$a_0(u^0, v) = \int_{\Gamma_1} u^0 v d\Gamma_1 + \int_{\Gamma_2} u^0 v d\Gamma_2 \tag{4.21}$$

Define the corresponding linear form $f : X \to \Re$ as

$$f_0(v) = \int_{\Gamma_1} \frac{T_0 - B}{A} v d\Gamma_1 + \int_{\Gamma_2} \frac{T_0 - B}{A} v d\Gamma_2 \tag{4.22}$$

The discrete variational problem for the initial condition is thus expressed as:

Find $u^0 \in X$ such that the following equation holds:

$$a_0(u^0, v) = f_0(v), \quad \forall v \in X' \tag{4.23}$$

However, since $u(\underline{\xi}, 0)$ is known by the initial condition, one could also interpolate $u(\underline{\xi}, 0)$ with functions from the space X.

4.3 Implementation in FEniCS

The discrete variational formulation is implemented in the finite element software FEniCS. The three different layers in the casing constituting the region Γ_2 are defined and marked as separate so-called subdomains. Also the inner region Γ_1 is defined as a separate subdomain. This is done in order to assign different values to the spatial dependent dimensionless parameters in the problem. We use a loop in order to solve the stationary variational problems for each timestep. The source code is given in Appendix C.

Chapter 5

Results

In this chapter the results of the numerical implementation are presented. First we specify the parameters for the numerical simulations.

5.1 Input Parameters

This section presents the parameter set that is used in the simulations. We apply a constant ambient air temperature of 25 ℃ which yields $g = 298.15$ (K). We also use an initial condition corresponding to a uniform temperature distribution of $T_0 = 298.15$ (K). Furthermore, an external heat transfer coefficient of $h = 18$ (W/m^2 K) is applied. The choice for this value of h is given by an estimation in Appendix B.4. The physical input parameters are presented in table 5.1. We also included the time t_c for which the current is cut off in the table.

Table 5.1: Physical input parameters

Parameter	Value	Unit
g	298.15	(K)
h	18	(W/m^{2}K)
T_0	298.15	(K)
t_c	3240	(s)

We choose the scaling constants L_1, L_2, L_3 equal to the length of the battery in the x_1, x_2 and x_3 directions, respectively. This is done in order to obtain a scaled unit geometry. Moreover we choose the other scaling constants so that the different terms in the discrete variational formulation (4.19) obtains nearly the same order of magnitude. The scaling constants are presented in table 5.2.

Table 5.2: Scaling constants and dimensionless parameters

Parameter	Value	Unit
A	$1.0 \cdot 10^{-2}$	(K)
$B = g$	298.15	(K)
C	$1.4 \cdot 10^{6}$	(J/m^3 K)
α	$1.0 \cdot 10^{-2}$	(W/m^2 K)
L_1	$5.65 \cdot 10^{-3}$	(m)
L_2	$2.346 \cdot 10^{-1}$	(m)
L_3	$1.450 \cdot 10^{-1}$	(m)
γ_1	1	(-)
γ_2	0.0241	(-)
γ_3	0.0389	(-)
t_τ	4469.2	(s)
τ_c	0.725	(-)
i	1.0	(A)
δ	1.0	(V)
ϵ	1.0	(V)
g'	0	(W/m^2)
h'	$1.8 \cdot 10^{-1}$	(W/m^2)
$\langle f \rangle$	1.648	(-)
$\langle \Lambda_1^{-1} \rangle^{-1}$	381.02	(-)
$\langle \Lambda_1 \rangle$	3082.54	(-)
ε	0.083	(-)

We find it sufficient to model the problem in 2 dimensions, since the geometry in the ξ_2 and ξ_3-direction are quite similar. Therefore we chose to solve the problem in the ξ_1-ξ_2-plane. The problem was solved numerically with the discrete function spaces of piecewise linear Lagrange polynomials, i.e.

$$X = X' = \{\text{Space of piecewise linear Lagrange polynomials}\}$$

Regarding the specifications of the mesh in FEniCS, we find it convenient to define the number of partitions on the ξ_1 and ξ_2 axis as K_1 and K_2, respectively. These partitions yields a grid of rectangles, where each rectangle is divided into two triangles. The triangles are referred to as cells [36]. We find it sufficient to apply $K_1 = K_2 = 30$ for the modeling purposes. The different numerical parameters are given values based on numerical experiments presented in section 5.2.

The numerical parameters are presented in table 5.3.

Table 5.3: Numerical parameters

Parameter	Value	Unit
θ	0.5	-
$\Delta\tau$	0.005	-
K_1	30	-
K_2	30	-

5.2 Numerical Experiments

In this section we demonstrate some effects of varying numerical parameters. However, this should not be considered as a study on numerical stability and accuracy, which is beyond the scope of this work.

5.2.1 Effect of Element Size

Here we show that a mesh built by the parameters $K_1 = K_2 = 10$ causes artifacts. The mesh is shown in figure 5.1.

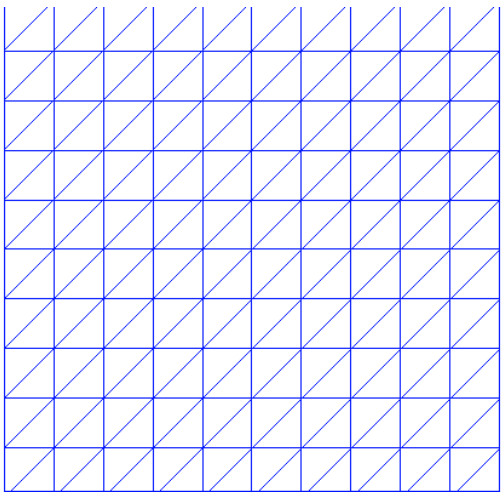

Figure 5.1: 2D finite element mesh. $K_1 = K_2 = 10$.

A snapshot of the dimensionless temperature profile at $\tau = 0.1$ along the line $\xi_2 = 0.5$ is shown in figure 5.2. The numerical parameters were $\theta = 0.5$,

$\Delta\tau = 0.005$ and $K_1 = K_2 = 10$. Other input parameters are given by tables 5.1-5.2.

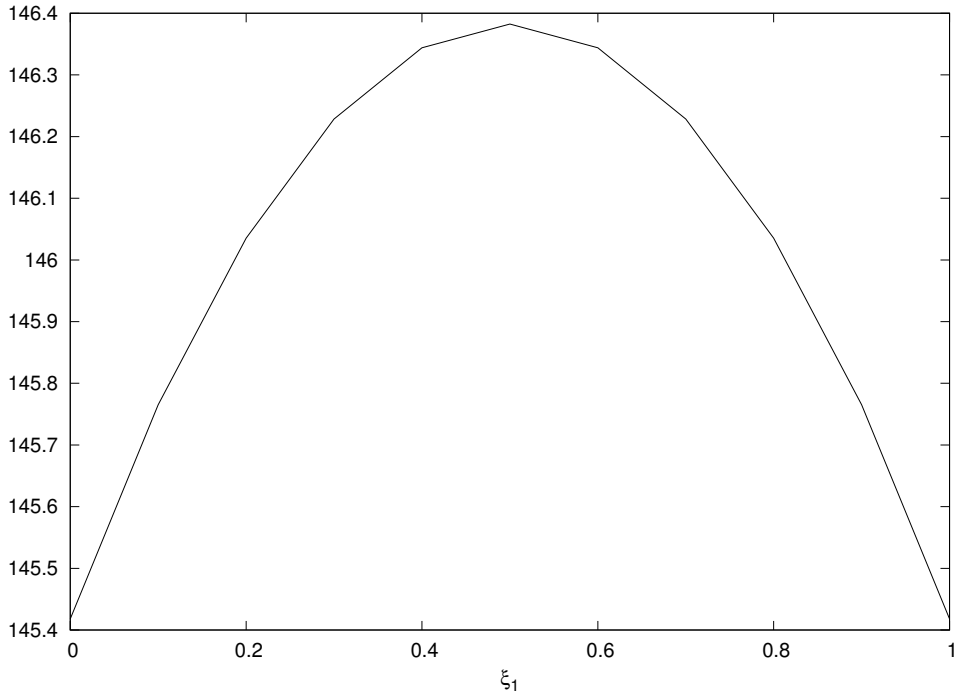

Figure 5.2: Snapshot of temperature profile at $\tau = 0.1$ along the line $\xi_2 = 0.5$. Numerical parameters $\theta = 0.5$, $\Delta\tau = 0.005$, $K_1 = 10$ and $K_2 = 10$. Input data given by tables 5.1-5.2. The figure shows the effect of few cells, causing the edges in the curve.

As figure 5.2 shows, there are artifacts in the solution by means of sharp edges in the curve. These artifact disappears by choosing $K_1 = K_2 = 30$, which is the choice for the further simulations.

5.2.2 Effect of Time Derivative Approximation Method

Here we show that a forward Euler approximation of the time derivative yields an unstable scheme at certain values of $\Delta\tau$. Figure 5.3 illustrate this, where a snapshot of the solution at $\tau = 0.1$ is plotted along the line $\xi_2 = 0.5$ for $\Delta\tau = 0.001$. The other numerical parameters are $K_1 = 30$, $K_2 = 30$ and $\theta = 0.0$. Other input parameters are given by tables 5.1-5.2.

We therefore omit the forward Euler approximation in our further numerical simulations. The backward Euler approximation however provides

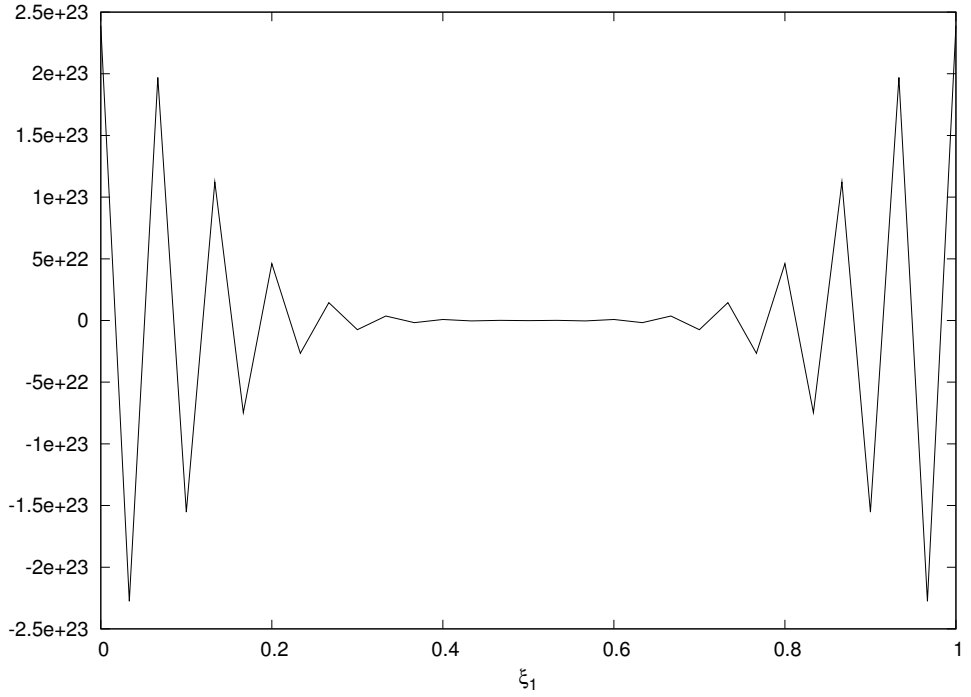

Figure 5.3: Snapshot of temperature profile at $\tau = 0.1$ along the line $\xi_2 = 0.5$. Numerical parameters $\theta = 0.0$, $\Delta\tau = 0.001$, $K_1 = 30$ and $K_2 = 30$. Input data given by tables 5.1-5.2. Heavy artifacts are observed for this forward Euler approximation.

no numerical artifacts at a timestep length $\Delta\tau = 0.1$, i.e. 100 times longer step-length than the length that caused an unstable forward Euler scheme. This is illustrated in figure 5.4, where a snapshot of the solution at $\tau = 0.9$ along the line $\xi_2 = 0.5$ is presented. The other numerical parameters are $K_1 = 30$, $K_2 = 30$ and $\theta = 1.0$. Other input parameters are given by tables 5.1- 5.2.

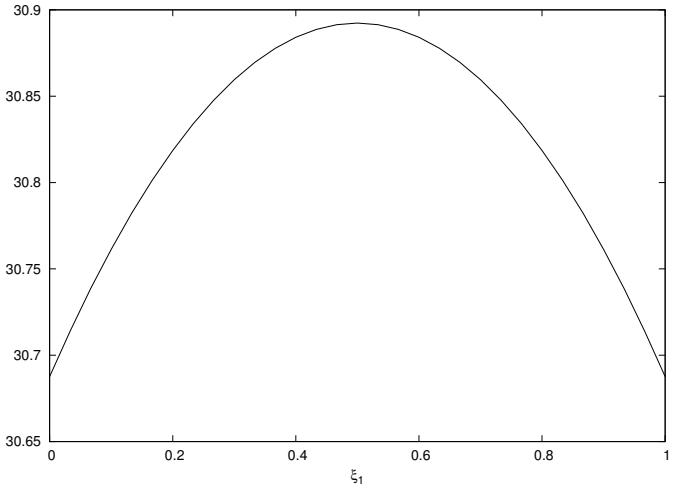

Figure 5.4: Snapshot of temperature profile at $\tau = 0.9$ along the line $\xi_2 = 0.5$. Numerical parameters $\theta = 1.0$, $\Delta\tau = 0.1$, $K_1 = 30$ and $K_2 = 30$. Input data given by tables 5.1-5.2. No numerical artifacts are observed in this backward Euler approximation.

However, from now on we only apply the Cranc-Nicolson approximation for our numerical simulations. This is done because it in general provides higher accuracy than the backward Euler approximation [35]. We emphasize however that a Cranc-Nicolson scheme may be more unstable for certain problems, than the backward Euler scheme [35].

5.2.3 Verification of the Code

To sort out bugs in the code or detect numerical artifacts, we run the code with the source term set to zero and with an initial condition that corresponds to the ambient temperature. Visual changes in the temperature are thus the results of bugs in the code or numerical artifacts. Figure 5.5 shows a snapshot of the solution along the line $\xi_2 = 0.5$ at $\tau = 0.9$. Input parameters are given by tables 5.1-5.3.

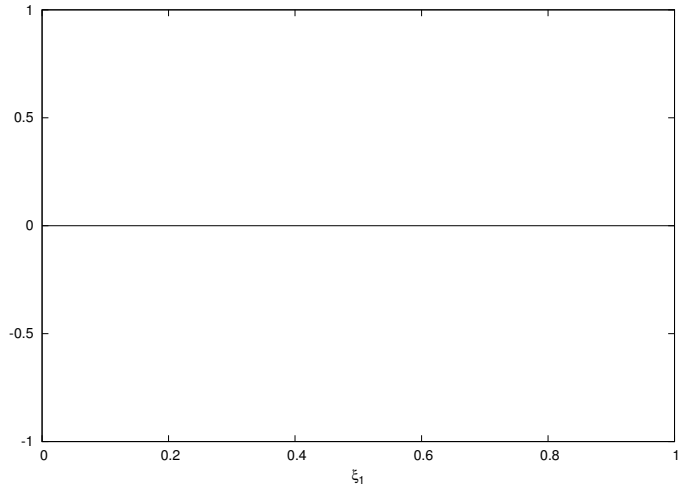

Figure 5.5: Snapshot of the solution along the line $\xi_2 = 0.5$ at $\tau = 0.9$. The source term is here set to zero. Input parameters given by tables 5.1-5.3. No numerical artifacts or errors are observed.

As figure 5.5 shows, no numerical artifacts or errors are observed.

Based on the numerical experiments done in this section, we choose the numerical parameters given by table 5.3 for the numerical simulations.

5.3 Simulation Results

Here we present the numerical solutions of the discrete variational problem defined in chapter 4.2. The solutions are provided by the FEniCS code as described in chapter 4.3. We model the problem in 2 dimensions due to the nearly similar geometry in the ξ_2 and ξ_3 directions. For the numerical solutions in this section, we use a mesh defined by the numerical parameters $K_1 = 30$ and $K_2 = 30$. This mesh is shown in figure 5.6.

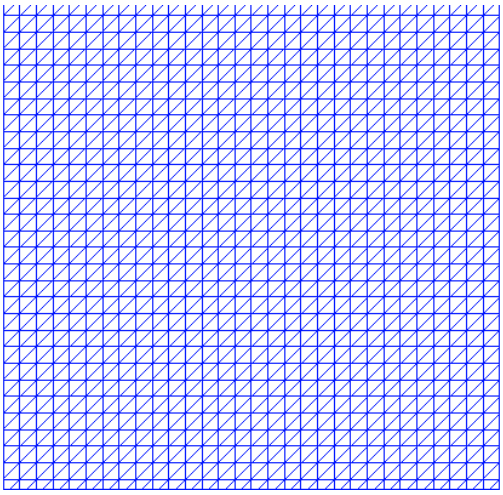

Figure 5.6: Mesh used in the numerical solutions. $K_1 = K_2 = 30$.

The input parameters in this section are given by tables 5.1-5.3. Figure 5.7 shows the initial condition projected onto the vector space of piecewise linear Lagrange polynomials.

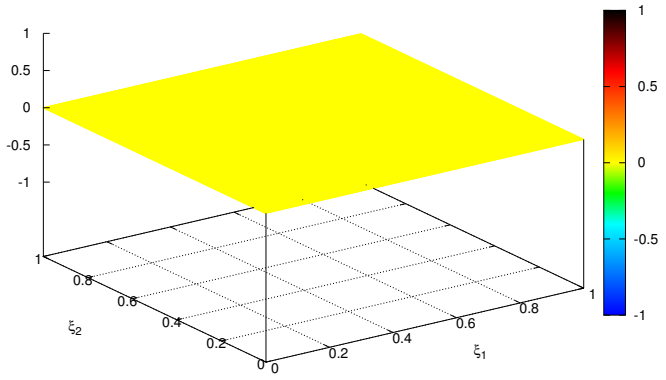

Figure 5.7: Initial condition (projected). Input parameters in tables 5.1-5.3.

Figure 5.8 shows a snapshot of the dimensionless temperature field at the instant $\tau = 0.3$.

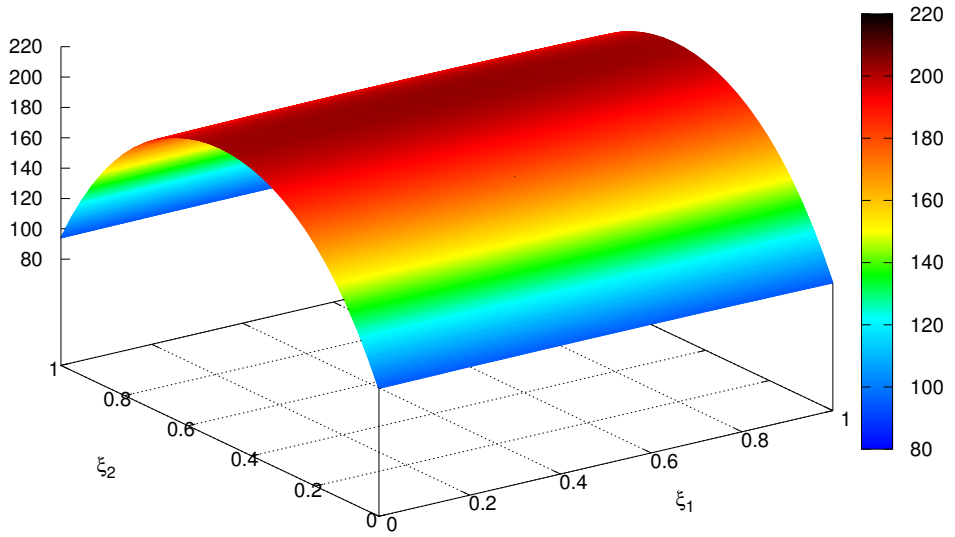

Figure 5.8: Snapshot of temperature field at $\tau = 0.3$. Input parameters given in tables 5.1 -5.3.

The temperature profile in the ξ_2-direction vary significantly compared with the temperature profile in the ξ_1-direction. Thus the temperature variation in the ξ_1 direction can not be observed in figure 5.8. However, a snapshot of the dimensionless temperature profile along the line $\xi_2 = 0.5$ at $\tau = 0.3$ shows this situation. This can be observed in figure 5.9.

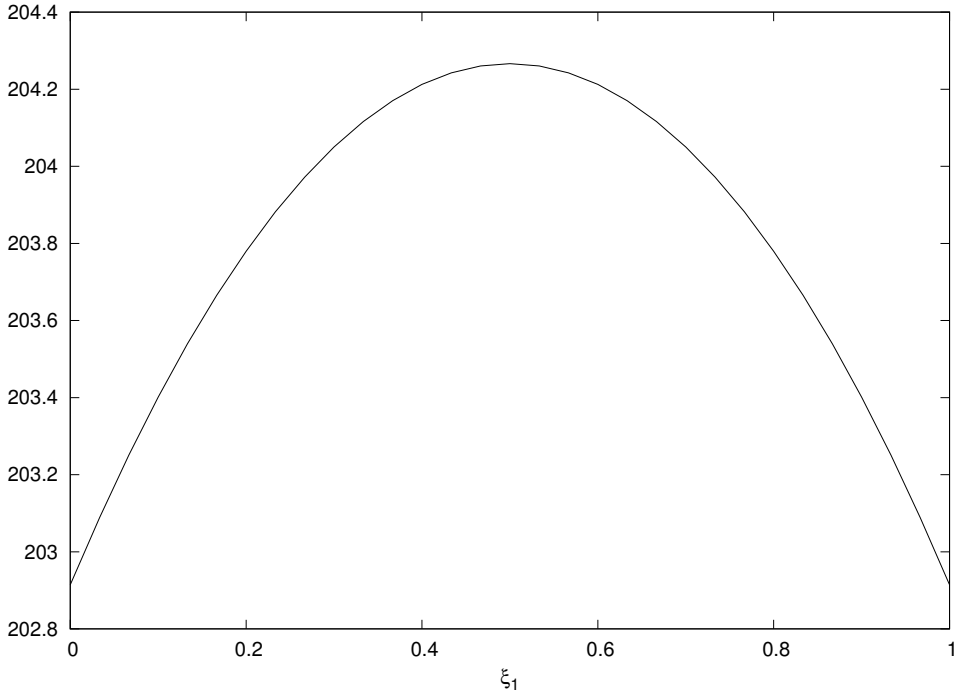

Figure 5.9: Snapshot of temperature profile along the line $\xi_2 = 0.5$ at $\tau = 0.3$. Input data given by tables 5.1 -5.3. Relatively low variation in dimensionless temperature is observed in the ξ_1- variable.

To study the qualitative behavior of the time dependent system, we plot snapshots of the dimensionless temperature profile along the line $\xi_1 = 0.5$ at different instants in time. This is shown in the series of figures 5.10- 5.13.

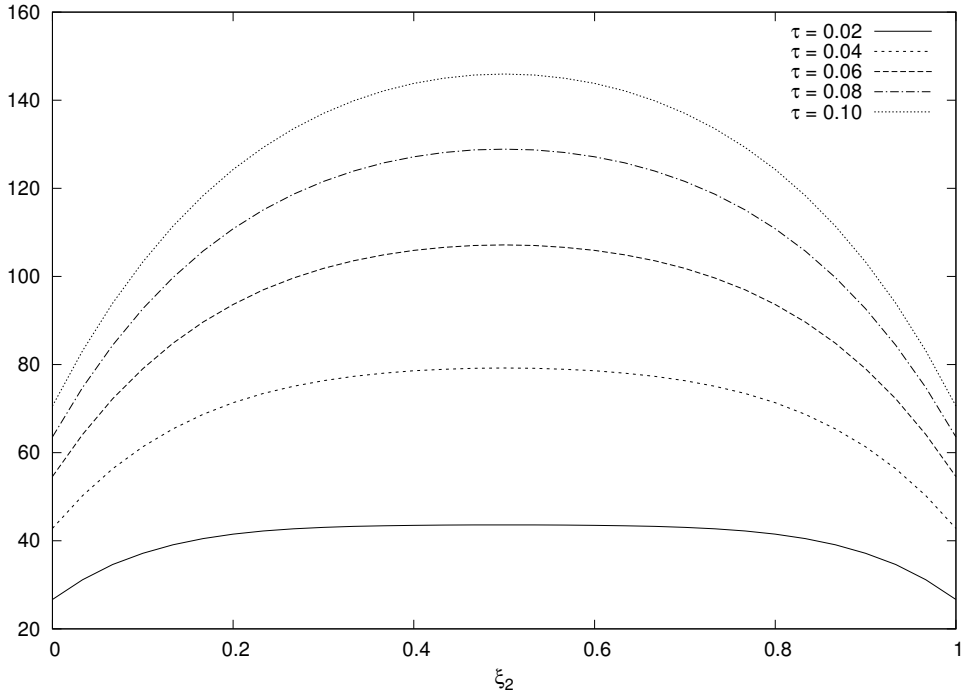

Figure 5.10: Snapshots of temperature profile along the line $\xi_1 = 0.5$ at different instants in time. Input parameters given by tables 5.1-5.3. Here the snapshots are taken right after the dimensionless temperature is starting to increase.

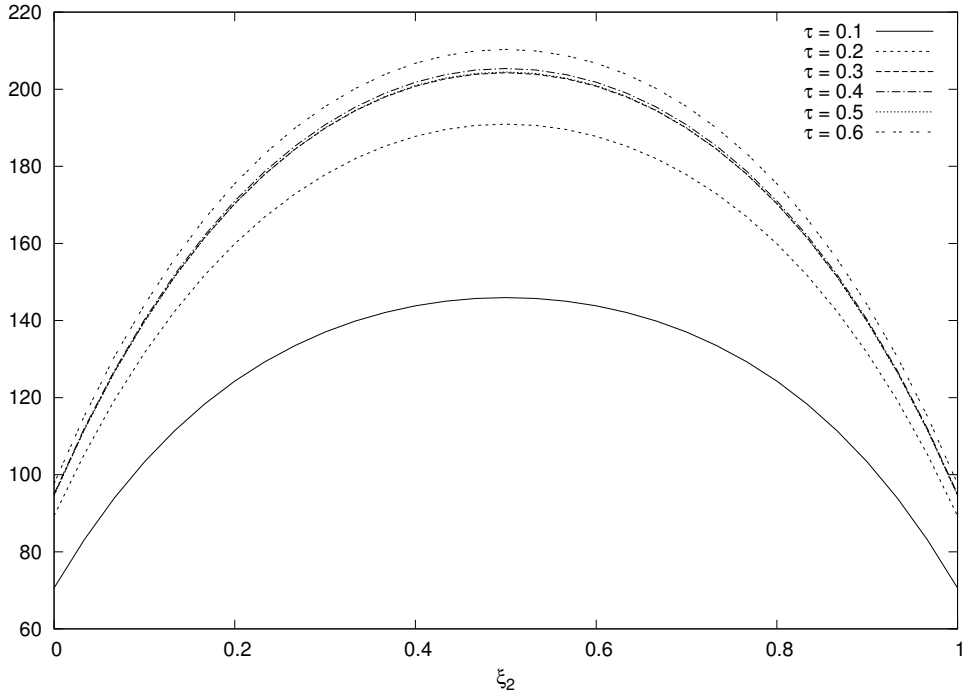

Figure 5.11: Snapshots of temperature profile along the line $\xi_1 = 0.5$ at different instants in time. Input parameters given by tables 5.1-5.3. These snapshots follows the dimensionless temperature profile of the battery from the start to it approaches end of discharge at $\tau = 0.725$.

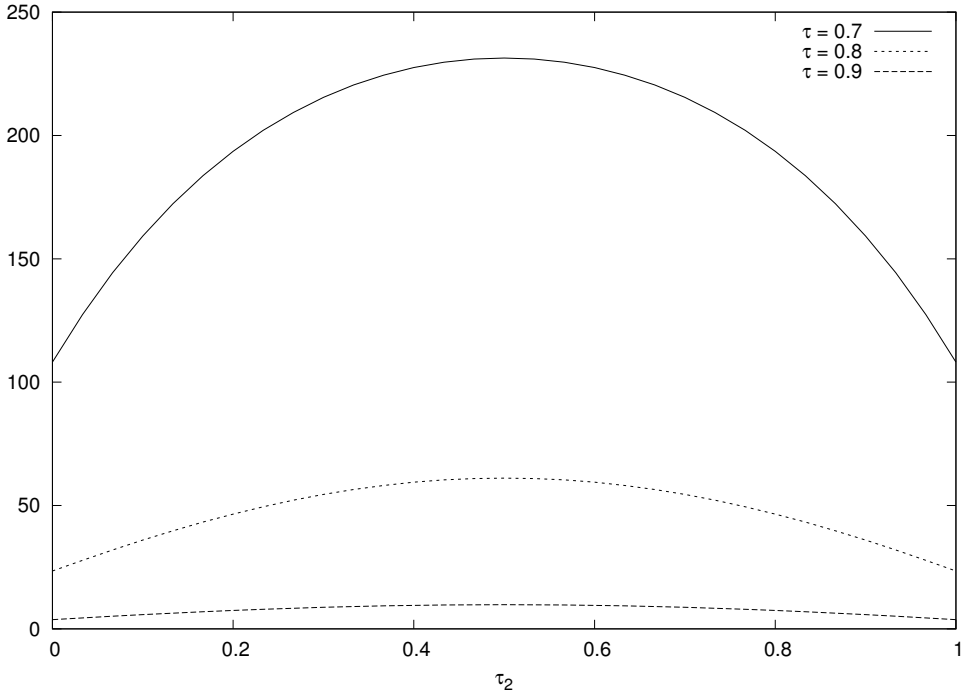

Figure 5.12: Snapshots of temperature profile along the line $\xi_1 = 0.5$ at different instants in time. Input parameters given by tables 5.1-5.3. These snapshots follows the dimensionless temperature profile of the battery from it approaches end of discharge at $\tau = 0.725$ and after the source term is cut off.

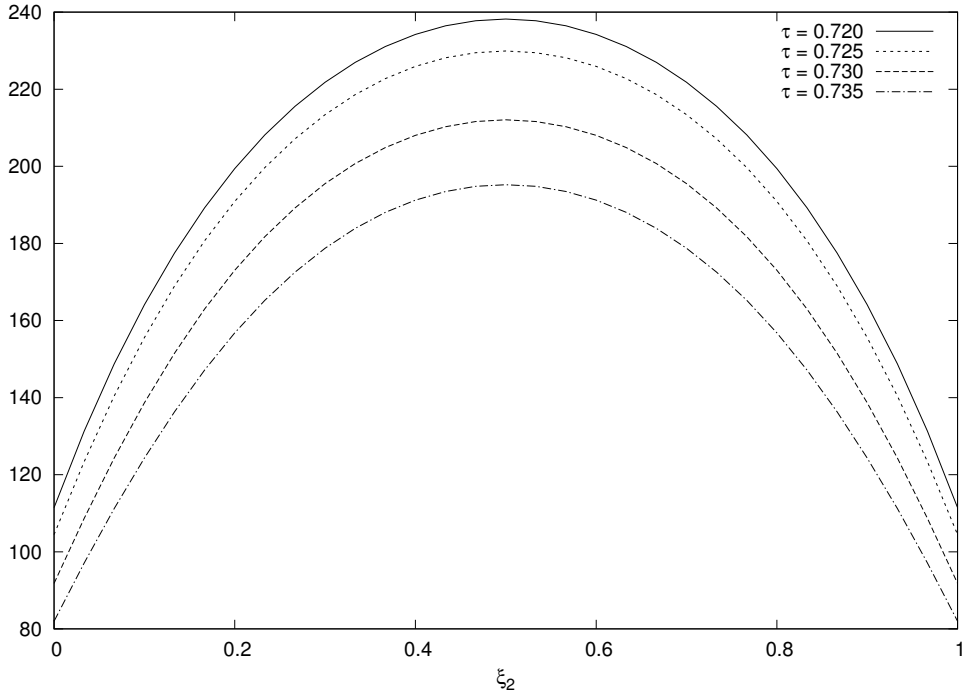

Figure 5.13: Snapshots of temperature profile along the line $\xi_1 = 0.5$ at different instants in time. Input parameters given by tables 5.1-5.3. These snapshots follows the dimensionless temperature profile of the battery from it approaches end of discharge at $\tau = 0.725$ and in the instants after the source term is cut off.

As the figures in this section illustrates, the temperature of the battery varies significant in the ξ_2-direction compared with the ξ_1-direction. This trend is found to be independent of time. The battery is approximately longer by a factor 40 in the ξ_2-direction than in the ξ_1-direction. One may at first think that the difference in length scales are the reason to these results. However, the dimensionless homogenized thermal conductivity in the ξ_2-direction is larger by approximately a factor 10 compared with the ξ_1-direction. This clearly also affects the results.

The maximum temperature is obtained in the center of the battery at the time just before the source term no longer contribute. The dimensionless maximum temperature corresponds to a temperature 2.4 (K) above the ambient air temperature at 298.15 (K).

The figures 5.10-5.13 also shows that the dimensionless temperature increases and decreases at a higher rate shortly after the source term are start-

ing to contribute and shortly after the source term becomes zero.

The results from this modeling seem to be reasonable from a physical point of view. However we emphasize that the results are obtained from a homogenized model with a simplified source term. The geometry is also slightly simplified. Moreover, heat generating contributions from the main current collector terminals are neglected. Furthermore, we have only a crude estimation of the external heat transfer coefficient.

Chapter 6

Conclusions and Outlook

In this work a homogenized thermal model that describes the dimensionless temperature field in a lithium ion battery is derived. The battery is divided into an inner and an outer region. In the inner region the thermal conductivity tensor is periodic in a microvariable. The outer region consists of 3 layers that is wrapped around the inner region. We describe the dimensionless temperature field of the inner region by a homogenized partial differential equation. However, in the outer region the dimensionless temperature field is described by a non-homogenized partial differential equation. The temperature field in both regions is described by the two coupled partial differential equations. The coupled model is applied to a conventional lithium ion pouch-cell battery with 17.5 Ah capacity. Input data to the model are obtained from experiments. The model is solved in 2 dimensions by means of the finite element method in the FEniCS software.

In order to solve a corresponding non-homogenized model for both regions in FEniCS, it is required in addition to program 97 regions or subdomains in the mesh. Therefore the homogenization greatly simplifies the implementation.

We remark that the derived homogenized thermal conductivity tensor is identical with expressions obtained by applying a thermal equivalent-resistance approach. Such expressions are applied in thermal models of lithium ion batteries by e.g. Chen et al. [8]. However, we stress that other researchers have solved thermal models for lithium ion batteries numerically without applying such expressions.

The modeled dimensionless temperature field is found to vary significant in the ξ_2-direction, compared to the ξ_1-direction. In the homogenized model the dimensionless thermal conductivity for the homogenized region is larger by approximately a factor 10 in the ξ_2-direction, compared with the ξ_1-direction. However, the length of the physical battery is larger by approx-

imately a factor 40 in the ξ_2-direction than in the ξ_1-direction. We conclude that both these factors affect the modeled dimensionless temperature field.

The maximum temperature is achieved at a single spot at the time just before the source term no longer contributes. This spot is located at the center of the battery. The dimensionless maximum temperature corresponds to a temperature 2.4 (K) above the ambient air temperature at 298.15 (K).

The results of the numerical solutions seem to be physical reasonable. However, due to the simplifications taken one should be careful assuming that they are realistic before a validation procedure is performed. As pointed out in Appendix A the applied source term may represent an oversimplification from a theoretical point of view. In addition, as pointed out in Appendix B there is a need for obtaining more experimental data for the entropic heat coefficient in this source term. Furthermore the homogenization needs to be validated. However, if validated the presented model could be applied to describe any lithium ion battery with prismatic cell geometry. A validated model can be used to determine the internal temperature of the pouch-cell. The model may in the future also be used as a starting point of a parameter study on effects of different modeling parameters.

Although no numerical artifacts are observed and the numerical solution seems to be stable, it is necessary to perform both stability analysis and a numerical truncation analysis.

A natural extension of this work would be to validate the homogenization by comparing it with a non-homogenized model. The non-homogenized model may be solved analytically or numerically. One could also add the first order correction of the asymptotic expansion representation and study the effect of this. The result of this experiment could say something about the limit for the validity of the homogenization theory. Homogenization is expected to be exact in the limit when the micro to macroscale parameter ε goes to zero.

If the homogenization is found to provide reliable results, the source term and the geometrical simplifications must be validated as well.

In future work an experimental validation should be feasible. It will eventually validate the simplification of the source term, geometrical simplifications and the homogenization.

Another interesting extension is to apply a more detailed heat source term. The modeling framework presented in this work is assumed to handle this.

Bibliography

[1] 2011 American Control Conference (AACC). *PDE Model for Thermal Dynamics of a Large Li-Ion Battery Pack*, June 29 - July 01 2011.

[2] T.M. Bandhauer, S. Garimella, and T.F. Fuller. ACritical Review of Thermal Issues in Lithium-Ion Batteries. *Journal of the Electrochemical Society*, 158, 2011.

[3] D. Bernardi, E. Pawlikowski, and J. Newman. A General Energy Balance for Battery Systems. *Journal of the Electrochemical Society*, 132:5, 1985.

[4] S. Bhide and T. Shim. Novel Predictive Electric Li-Ion Battery Model Incorporating Thermal and Rate Factor Effects. *IEEE Transactions on vehicular technology*, 60, 2011.

[5] G.G. Botte, V.R. Subramanian, and R.E. White. Mathematical modeling of secondary lithium batteries. *Electrochemical Acta*, 45:2595, 2000.

[6] L. Cai and R.E. White. Mathematical modeling of a lithium ion battery with thermal effects in COMSOL Inc. Multiphysics (MP) software. *Journal of Power Sources*, 196, 2011.

[7] Y. A. Cengel. *Heat and mass transfer: A practical approach.* McGraw-Hill, 1221 Avenue of the Americas, New York, NY 10020, USA, 3. edition, 2006.

[8] S.C. Chen, C.C. Wan, and Y.Y. Wang. Thermal analysis of lithium-ion batteries. *Journal of Power Sources*, 140, 2005.

[9] S.C. Chen, Y.Y. Wang, and C.C. Wan. Thermal Analysis of Spirally Wound Lithium Batteries. *Journal of The Electrochemical Society*, 153, 2006.

[10] Y. Chen and J.W. Evans. Heat Transfer Phenomena in Lithium/Polymer-Electrolyte Batteries for Electric Vehicle Application. *Journal of the Electrochemical Society*, 140:1833, 1993.

[11] Y. Chen and J.W. Evans. Three-dimensional Thermal Modeling of Lithium-Polymer Batteries under Galvanostatic Discharge and Dynamic Power Profile. *Journal of the Electrochemical Society*, 141:2947, 1994.

[12] Y. Chen and J.W. Evans. Thermal Analysis of Lithium-Ion Batteries. *Journal of the Electrochemical Society*, 143:2708, 1996.

[13] F. Ciucci and W. Lai. Derivation of Micro/Macro Lithium Battery Models from Homogenization. *Trans Porous Med*, 88:249–270, 2011.

[14] M. Doyle and J. Newman. The use of mathematical modeling in the design of lithium/polymer battery systems. *Electrochemical Acta*, 40:2191, 1995.

[15] G. M. Ehrlich. *HANDBOOK OF BATTERIES*. McGraw-Hill, USA, 3 edition, 2002.

[16] W. Fang, O.J. Kwon, and C-Y. Wang. Electrochemical-thermal modeling of automotive Li-ion batteries and experimental validation using a three-electrode cell. *Int. J. Energy Res.*, 34, 2010.

[17] C. Forgez, D.V. Do, G. Friedrich, M. Morcrette, and C. Delacourt. Thermal modeling of a cylindrical LiFePO_4/graphite lithium-ion battery. *Journal of Power Sources*, 195:2961–2968, 2010.

[18] A. Funahashi, Y. Kida, K. Yanagida, T. Nohma, and I. Yonezu. Thermal simulation of large-scale lithium secondary batteries using a graphite-coke hybrid carbon negative electrode and lini_0.7co_0.3o_2 posistive electrode. *Journal of Power Sources*, 104, 2002.

[19] R.E. Gerver and J.P. Meyers. Three-Dimensional Modeling of Electrochemical Performance and Heat Generation of Lithium-Ion Batteries in Tabbed Planar Configurations. *Journal of The Electrochemical Society*, 158:A835–A83, 2011.

[20] S. Golomon, K. Maute, and M. L. Dunn. Numerical modeling of electrochemical-mechanical interactions in lithium polymer batteries. *Computers and Structures*, 87:1567–1579, 2009.

[21] P.M. Gomadam, J.W. Weidner, R.A. Dougal, and R.E. White. Mathematical modeling of lithium-ion and nickel battery systems. *Journal of Power Sources*, 110, 2002.

[22] M. Guo, G. Sikha, and R.E. White. Single-Particle Model for a Lithium-Ion Cell: Thermal Behavior. *Journal of the Electrochemical Society*, 158:A122, 2011.

[23] Y. Inui, Y. Kobayashi, Y. Watanabe, Y. Watase, and Y. Kitamura. Simulation of temperature distribution in cylindrical and prismatic lithium ion secondary batteries. *Energy Conversion and Management*, 48, 2007.

[24] D.H. Jeon and S.M. Baek. Thermal modeling of cylindrical lithium ion battery during discharge cycle. *Energy Conversion and Management*, 52, 2011.

[25] S. A. Khateeb, M. M. Farid, J. R. Selman, and S. Al-Hallaj. Design and simultation of a lithium-ion battery with a phase change material thermal management system for an electric scooter. *Journal of Power Sources*, 128:292–307, 2004.

[26] G-H. Kim, K. Smith, K-J. Lee, and S. Santhanagopalan. Multi-Domain Modeling of Lithium-Ion Batteries Encompassing Multi-Physics in Varied Length Scales. *Journal of The Electrochemical Society*, 158:A955, 2011.

[27] U.S. Kim, C.B. Shin, and C-S. Kim. Modeling for the scale up of a lithium-ion polymer battery. *Journal of Power Sources*, 189:A1461, 2009.

[28] U.S. Kim, C.B. Shin, and C.S. Kim. Effect of the electrode configuration in the thermal behavior of a lithium-polymer battery. *Journal of Power Sources*, 180, 2008.

[29] U.S. Kim, C.B. Shin, and C.S. Kim. Modeling for the scale-up of a lithium-ion polymer battery. *Journal of Power Sources*, 189, 2009.

[30] U.S. Kim, J. Yi, C.B. Shin, T. Han, and S. Park. Modeling the Dependence of the Discharge Behavior of a Lithium-Ion Battery on the Environmental Temperature. *Journal of The Electrochemical Society*, 158, 2011.

[31] U.S. Kim, J. Yi, C.B. Shin, T. Han, and S. Park. Modeling the thermal behaviour of a lithium-ion battery during charge. *Journal of Power Sources*, 196, 2011.

[32] R. Kizilel, R. Sabbah, J.R. Selman, and S. Al-Hallaj. An alternative cooling system to enhance the safety of Li-ion battery packs. *Journal of Power Sources*, 194, 2009.

[33] E. Kreyszig. *Advanced engineering mathematics*. John Wiley & Sons, Inc., 111 River Street, Hoboken, NJ, 9 edition, 2006.

[34] K. Kumaresan, G. Sikha, and R.E. White. Thermal Model for a Li-Ion Cell. *Journal of the Electrochemical Society*, 155:A164, 2008.

[35] H. P. Langtangen. *Computational Partial Differential Equations: Numerical Methods and Diffpack Programming*. Simula Research Laboratory and
Department of Informatics, University of Oslo, 2. edition, 2002.

[36] H. P. Langtangen. A FEniCS Tutorial. www.fenicsproject.org/doc, 2011.

[37] R. Mahamud and C. Park. Reciprocating air flow for Li-ion battery thermal management to improve temperature uniformity. *Journal of Power Sources*, 196, 2011.

[38] H. Maleki and A.K. Shamsuri. Thermal analysis and modeling of a notebook computer battery. *Journal of Power Sources*, 115, 2003.

[39] A. Mantiharam. *Lithium Batteries: Science and Technology*. Springer Science+Business Media (LLC), New York, 2003.

[40] K. Matsuki and K. Ozawa. *Lithium Ion Rechargeable Batteries: Materials, Technology and New Applications*. Wiley-VCH Verlag GmbH & Co, Weinheim, 2009.

[41] A. Mills and S. Al-Hallaj. Simulation of passive thermal management systems for lithium-ion battery packs. *Journal of Power Sources*, 141, 2005.

[42] D. C. Montgomery, E. A. Peck, and G. G. Vining. *Introduction To Linear Regression Analysis*. John Wiley & Sons, Inc., 3. edition, 2001.

[43] P.W.C. Northrop, V. Ramadesigan, S. De, and V.R. Subramanian. Coordinate Transformation, Orthogonal Collocation, Model Reformulation and Simulation of Electrochemical-Thermal Behavior of Lithium-Ion Battery Stacks. *Journal of the Electrochemical Society*, 158:A1461, 2011.

[44] C.R. Pals and J. Newman. Thermal Modeling of the Lithium/Polymer Battery: I. Discharge Behavior of a Single Cell. *Journal of the Electrochemical Society*, 142:3274, 1995.

[45] L.E. Persson, L. Persson, N. Svanstedt, and J. Wyller. *The Homogenization Method: An introduction*. Studentlitteratur, Chartwell Bratt, 1993.

[46] D.V. Portnyagin. Computational Modeling of Discharge of a Lithium Battery with a Microporous Carbon Electrode. *Russian Journal of Electrochemistry*, 46, 2010.

[47] E. Prada, D.D. Domenico, Y. Creff, J. Bernard, and V. Sauvant-Moynot. A coupled 0D electrochemical ageing & electro-thermal Li-ion modeling approach for HEV/PHEV. *IEEE*, 2011.

[48] L. Rao and J. Newman. Heat-Generation Rate and General Energy Balance for Insertion Battery Systems. *Journal of the Electrochemical Society*, 144:2697, 1997.

[49] R. Sabbah, R. Kizilel, J.R. Selman, and S. Al-Hallaj. Active (air-cooled) vs. passive (phase change material) thermal management of high power lithium-ion packs: Limitation of temperature rise and uniformity of temperature distribution. *Journal of Power Sources*, 182, 2008.

[50] M. Sievers, U. Sievers, and S.S. Mao. Thermal modelling of new Li-ion cell design modifications. *Forsch Ingenieurwes*, 74, 2010.

[51] K. Smith and C.Y. Wang. Power and thermal characterization of a lithium-ion battery pack for hybrid-electric vehicles. *Journal of Power Sources*, 160, 2006.

[52] K. Somasundaram, E. Birgersson, and A.S. Mujumdar. Thermal-electrochemical model for passive thermal management of a spiral-wound lithium-ion battery. *Journal of Power Sources*, 203, 2012.

[53] L. Song and J.W. Evans. The Thermal Stability of Lithium Polymer Batteries. *Journal of the Electrochemical Society*, 145:2327, 1998.

[54] L. Song and J.W. Evans. Electrochemical-Thermal Model of Lithium Polymer Batteries. *Journal of the Electrochemical Society*, 147:2086, 2000.

[55] R. Spotnitz and J. Franklin. Abuse behavior of high-power, lithium-ion cells. *Journal of Power Sources*, 113:81, 2003.

[56] R. Srinivasan. Monitoring dynamic thermal behavior of the carbon anode in a lithium-ion cell using a four-probe technique. *Journal of Power Sources*, 198, 2012.

[57] K.E. Thomas and J. Newman. Thermal Modeling of Porous Inserion Electrodes. *Journal of The Electrochemical Society*, 150:A176–A192, 2003.

[58] V.V. Viswanathan, D. Choi, D. Wang, W. Xu, S. Towne, R.E. Williford, J.G. Zhang, J. Liu, and Z. Yang. Effect of entropy change of lithium intercalation in cathodes and anodes on Li-ion battery thermal management. *Journal of Power Sources*, 195:3720–3729, 2010.

[59] C.Y. Wang and V. Srinivasan. Computational battery dynamics (CBD)-electrochemical/thermal coupled modeling and multi-scale modeling. *Journal of Power Sources*, 110, 2002.

[60] H. Warlimont. *Springer Handbook of Condensed Matter and Materials Data*. Springer, 2005.

[61] R.E. Williford, V.V. Viswanathan, and J-G. Zhang. Effects of entropy change in anodes and cathodes on the thermal behavior of lithium ion batteries. *Journal of Power Sources*, 189:101–107, 2009.

[62] Y. Ye, Y. Shi, N. Cai, J. Lee, and X. He. Electro-thermal modeling and experimental validation for lithium ion battery. *Journal of Power Sources*, 199, 2012.

[63] Xiangchun Zhang. *MULTISCALE MODELING OF LI-ION CELLS: MECHANICS, HEAT GENERATION AND ELECTROCHEMICAL KINETICS* . PhD thesis, The University of Michigan, 2009.

Appendix A

A Review of Previous Thermal Models

In this chapter a brief review of previous thermal models for lithium ion batteries is presented. The main focus in this Appendix is on the approach taken to estimate the heat generation in thermal models. As the number of symbols used in this Appendix is quite large, we do not include these in the nomenclature. In this way we also preserve the original notation in the reviewed works. For easier reading, we also omit the units for the symbols when we present the various models.

A.1 A Brief Review of Previous Thermal Models

The recent years have shown a growth of published papers on thermal models of lithium ion batteries. The most detailed thermal models share the common feature that the thermal energy conservation on differential form is expressed in terms of a single partial differential equation, i.e.

$$\rho(\underline{x})C_p(\underline{x})\frac{\partial T(\underline{x},t)}{\partial t} = \nabla\cdot(\lambda(\underline{x})\nabla T(\underline{x},t)) + q(\underline{x},t), \quad \underline{x}\in\Omega, \quad t>0 \quad \text{(A.1)}$$

Here ρ denotes the mass density, C_p is the constant-pressure heat capacity, T represents the temperature field, t denotes the time and $\underline{x}$ is the Euclidean coordinate vector defined as

$$\underline{x} = [x_1, x_2, x_3]$$

Furthermore, Ω is a region in $\Re^3$ that is occupied by the battery. The thermal conductivity tensor is denoted as λ. The rate of heat generated while the battery is charged or discharged is represented by the source term q. It is mainly the composition of the source term q that varies in the different modeling works.

Bernardi et al. [3] presents a general energy balance equation that could be applied to various battery chemistries. Their energy equation is the first in the literature considering contributions from mixing, phase changes, and simultaneous electrochemical reactions with composition-dependent open-circuit potential. In their work, each of these contributions are derived and their importance discussed.

Bandhauer et al. [2] reviews the work by Bernardi et al. [2]. In the review they states that heat generated inside a battery is related to three different processes. These are activation heating due to interfacial kinetics, heating from species transport which is concentration driven and ohmic heating related to resistive heating of charged particles [2]. Bernardi et al. [3] presents a simplified expression for the heat generation q. A version of this simplified expression where phase changes and mixing effects are neglected is frequently reported in the literature on lithium ion battery models [2]. This source term reads

$$q = I(U - V) - I(T\frac{\partial U}{\partial T}) \tag{A.2}$$

Here I is the total cell current, V is the overall cell potential and U is the open circuit potential. The contributions to heat generation from overpotential related to ohmic losses, charge transfer overpotentials at the interface, and mass transfer limitations is described by the first term on the right side. The electrode potential is taken at the average composition. The heat due to entropy change is described by the second term on the right [2].

In a work by Thomas and Newman [57] it is found that the heat generated by mixing is small compared to heat generation from entropy change and resistive heating for a realistic and properly designed battery.

In larger cells developed for electric vehicle purposes, Ohmic heating in the current collectors may be of significance [2]. In the works by Kim et al. [28, 29], a temperature-independent parametrized electrochemical model is used to model the current distributions of two electrode current collectors. The local current production is estimated by means of local overpotential.

Moreover Ohm's law is applied to obtain the current distribution in the current collectors. They use the following heat generation term

$$q = i(U - V - T\frac{\partial U}{\partial T}) + (\sigma|\nabla\phi|^2)_{cc,pos} + (\sigma|\nabla\phi|^2)_{cc,neg} \tag{A.3}$$

Here the first term is similar to that of equation (A.2) and the two latter terms represents ohmic heating in the current collectors. The first study finds a 17 (K) temperature difference across the battery, where the hottest region is where the current collector ends in a current collector tab.

As Bandhauer et al. [2] points out, the thermal modeling works done on lithium ion batteries can be divided into models that use experimental data to obtain their heat generation rate and models that apply electrochemical models to obtain the heat generation rate.

One approach is to describe the source term by means of polynomials that is obtained by least square fitting of experimental data. This is done in the work by Sabbah et al. [49]. Another modeling work by Smyshlyaev et al. [1] assumes that the heat generation term can be measured/estimated. Kizilel et al. [32] predicts heat generation by means of an accelerating rate calorimetry (ARC) measurement. ARC measurement is also used in a simulation of a thermal management system for a lithium ion battery by Khateeb et al. [25]. A work by Mills and Al-Hallaj [41] measures experimentally the heat generation during a constant current discharge. An alternative approach consists of of considering only pure ohmic electrical heating effects as in the work by Bhide and Shim [4].

Chen et al. [8] studies a thermal model of a battery that consists of many layers of cells. They solve the equation considering the different thermal conductivities in each direction by means of the finite difference method. However, they also present a simplified model where the thermal conductivity is estimated by a thermal equivalent-resistance approach. Their result for the thermal conductivity in the direction perpendicular to the layered cells is:

$$\lambda = \frac{\sum_i L_i}{\sum_i (\frac{L_i}{k_i})} \tag{A.4}$$

This result is similar to that obtained from a homogenization procedure in section 3.3. Chen et al. [8] assumes a uniform heat generation distribution in the cell. The following source term are used

$$q = \frac{I}{V_{total}}(E_{OC} - U - T\frac{dE_{OC}}{dT}) \tag{A.5}$$

Here, V_{total} represents the volume of the heat generating region, E_{OC} and E represents the open-circuit and closed-circuit potential. I represents the total current while T represents the temperature.

Chen et al. [9] also presents a thermal model of a spiral wound lithium ion battery. The source term applied is (A.5). The model equation is then solved by an advanced numerical method.

Funahashi et al. [18] applies the source term (A.2) in their modeling work. They perform thermal simulation of a lithium ion battery that shows good agreement with experimental results. Their model equation is expressed in cylindrical coordinates, and is solved by means of the finite element method. However, they consider the thermal conductivity coefficient as homogeneous through the battery.

Chen and Evans [10] also applies the source term (A.5) to model the heat generation inside batteries with lithium cathode and polymer electrolyte. These batteries have a layered structure of many thin cells that constitute a cell-stack. The particular approach assumes uniform heat generation q inside the battery, expressed as

$$q = \frac{iN_{cell}}{LX}(E_{oc} - V - T\frac{dE_{oc}}{dT}) \tag{A.6}$$

Here i is the superficial current density, E_{oc} is the open-circuit voltage of a cell, LX is the thickness of the cell stack, T is the temperature, V is the cell voltage and N_{cell} is the number of cells in a stack. They furthermore use the source term in a 2 dimensional transient thermal energy balance equation to calculate the temperature distribution in each layer i in the cell, i.e.

$$\rho_i C_{pi}\frac{\partial T}{\partial t} = \lambda_i\frac{\partial^2 T}{\partial x^2} + \lambda_i\frac{\partial^2 T}{\partial y^2} + q \tag{A.7}$$

Here, ρ_i is the mass density of layer i, C_{pi} is the specific heat capacity of layer i, λ_i is the thermal conductivity of layer i and t is time. x and y are the spatial coordinates. The equation is solved by means of a finite difference method. In Chen and Evans [11], this model is extended to three dimensions. In that work, they estimate a value for the thermal conductivity in a similar manner as the way electrical equivalent resistance is calculated. Here they also justify the assumption of uniform heat generation more in detail. Their argument is that the cells are very thin compared to the length of the cell

stack. Furthermore, the heat generation takes place in each cell. Therefore they argue that this approach is reasonable.

Several other authors use a similar heat generation term as (A.2). Some of them are Maleki and Shamsuri [38], Portnyagin [46], Mahamud and Park [37], Prada et al. [47], Sievers et al. [50].

Pals and Newman [44] use it in a thermal model that is coupled to an electrochemical model, i.e. they use the thermal model to update temperature-dependent parameters in the electrochemical model. Their study considers a single-cell model, in one dimension. Moreover, they assume uniform temperature trough the cell, thus avoiding the use of a thermal conductivity coefficient. Doyle and Newman [14] also use the heat generation term A.2 to calculate the temperature of a single lithium anode/polymer electrolyte cell.

Williford et al. [61] apply the following source term in their thermal model:

$$q = I^2R + T\Delta S\frac{I}{nF} \tag{A.8}$$

Here I is the current density, R is the material resistance T is temperature, ΔS is the entropy change, n represents one electron per reaction and F is Faraday's constant. The equation (A.8) can be integrated over the cell to obtain the heat generation for the whole cell. They measure the entropy change ΔS using an electrochemical thermodynamic measurement system (ETMS). The experimental results are then used as inputs to the model. An experiment is set up for a prismatic lithium ion battery, using thermocouples at the surface of the battery. The battery consist of 8 cells that are stacked inside. The battery is under the experiment placed in a channel to allow convective air cooling that should have a similar effect on the different sides of the surface. The experimental results shows relatively good agreement with the simulated predictions.

Also a work by Inui et al. [23] considers heat generation due to entropy change. They apply a source term q expressed as

$$q = r_i i^2 - T\Delta S\frac{i}{nF} \tag{A.9}$$

Here r_i is the internal equivalent resistance per unit volume and i is the discharge current per unit volume. T is temperature, ΔS is the entropy change, n is the number of electrons involved in the reaction and F is Faraday's constant. They measure the the entropy change experimentally based on the the equation

$$\Delta S = nF\frac{\partial E_0}{\partial T} \tag{A.10}$$

where E_0 is the open circuit voltage of the battery. They find that the entropy change is dependent on state of charge and little affected by the temperature. They also measure the internal equivalent resistance. The corresponding energy balance equation is solved for both prismatic and cylindrical cell geometry. However, the thermal conductivities of the core region of the battery are considered as constants in each spatial direction.

Chen and Evans [12] presents a thermal model for a lithium ion battery. In their model, the convective flow of the liquid electrolyte is neglected. This is justified by the fact that the liquid electrolyte is trapped in the pore structure of the separator. The heat generation rate in each cell is assumed to be uniform. The authors use an experimental determined heat generation term q for their thermal model.

In a work by Song and Evans [53], a thermal model for a lithium/polymer electrolyte battery is presented. Their heat generation term reads

$$q = (\frac{\Delta\phi}{L})^2\sigma_e + i^2(\frac{RT}{i_{oa}nF} + \frac{RT}{i_{oc}nF}) - iT(\frac{dE_{oc}}{dT}) \tag{A.11}$$

Here $\Delta\phi$ is the potential difference across the electrolyte, L is the thickness of the polymer electrolyte and i is the current density. R and T is the gas constant and the temperature, respectively. n is the number of electrons involved in a stoichiometric reaction and F is Faraday's constant. i_{oa} and i_{oc} is the current exchange density of the anode and cathode, respectively. Finally, E_{oc} is the cell open-circuit potential. The first term on the right side of equation (A.11) represents ohmic heating in the polymer electrolyte. However, ohmic heating in the lithium and counter electrode is neglected by the authors. The next term is heat effects of the overpotentials at the anode and the cathode. Here they assume that the electrodes are in the linear polarization regime. The last term represents the reversible heat generation. The local current density i is here calculated for each time step based on the local value of the conductivity of the polymer electrolyte, which in turn is calculated by the temperature.

Gerver and Meyers [19] presents an thermal-electrochemical coupled model where the thermal model is based on the heat generation term (A.2). Moreover they extend it by including local heat generating effects from ohmic heating in the current collectors.

Botte et al. [5] reviews modeling of lithium ion batteries. In their work, they point out that the thermal conductivity vary in different directions even inside the cathode or anode of lithium ion cells. The same study find the heat capacity to be dependent of state of charge (SOC). However, no thermal models presented in literature consider these effects, they are therefore neglected in this work.

Kim et al. [28] presents a thermal model with the following heat source term:

$$q = aJ(E_{OC} - E - T\frac{dE_{OC}}{dT}) + a_p r_p i_p^2 + a_n r_n i_n^2 \tag{A.12}$$

Here a is the specific battery area, J is the current density, E_{OC} is the open-circuit potential of the cell, E is the voltage of the cell, T is the temperature, $a_{p,n}$ denotes the specific area of the negative and the positive electrodes and $i_{n,p}$ is the magnitude of the linear current density vectors at the negative and the positive electrode. $r_{n,p}$ denote the resistance in the negative and the positive electrode. The current density J is calculated by the following equation

$$J = Y(V_p - V_n - U) \tag{A.13}$$

Here Y and U are parameters that needs to be fitted. In their work these parameters are described by means of polynomial fitting of the variable depth of discharge (DOD) based on experiments. $V_{n,p}$ is the potential at the negative or the positive electrode. Moreover is the magnitude of the linear current density vectors calculated by the two following equations

$$\vec{i}_{n,p} = -\frac{1}{r_{n,p}}\nabla V_{n,p}, \quad in\ \Omega_{n,p} \tag{A.14}$$

where $\Omega_{n,p}$ is the domain of the negative and positive electrode. The equations (A.13)-(A.14) are then substituted into equation (A.12). As in the work by Chen et al. [8], the thermal conductivity in the different directions is estimated based by thermal equivalent networks.

In a later work by Kim et al. [29] this model is also applied. The thermal model is not coupled back to update the electrochemical model, however. The model is extended by Kim et al. [30] to be applied for different ambient temperatures. Thus the parameters in the heat generation term are made temperature dependent. In this work, they use IR images to verify their model experimentally. This thermal model is also applied in a work by Kim et al. [31] to simulate a lithium ion battery during charge.

Coupled thermal-electrochemical models which consider local heat generation phenomena are frequently presented in the literature. Advanced models consists of coupled partial differential equations for the temperature field, chemical concentrations, electric potentials etc. The coupling enters the thermal model equation through the source term. The most detailed of these models also have temperature dependent parameters in the electrochemical models, such that both models need to be solved simultaneously. These models are referred to as fully coupled models. A review of the most detailed coupled models are beyond the scope of this work, however. We refer the reader to the references [6, 16, 21, 57, 22, 26, 31, 27, 34, 43, 48, 51, 52, 54, 59, 62] for presentations, reviews and applications of detailed coupled models for thermal modeling of lithium ion batteries.

However, many of these models are similar, we therefore present the source term from Somasundaram et al. [52]:

$$q = J\eta + JT\frac{\partial U_{ref,i}}{\partial T} + \sigma_s^{eff}(\nabla\phi_s)^2 + \sigma_l^{eff}(\nabla\phi_l)^2 + \frac{2RT\sigma_l^{eff}}{F}(1-t_+^0)\nabla(ln\ c_l)\cdot\nabla\phi_l, \quad i = ne, pe \tag{A.15}$$

Here J is the local charge transfer current per unit volume, η is the overpotential, $U_{ref,i}$ is the open circuit potential of the electrode, σ_s^{eff} and σ_l^{eff} is the effective electronic conductivity of the solid and the liquid phase, respectively. ϕ_s and ϕ_l is the solid and liquid phase potential, respectively. t_+^0 is the transference number of the cations, R is the gas constant, F is Faraday's constant and c_l is the electrolyte concentration. ne and pe denotes the negative and the positive electrode, respectively. Models with this type of source term which are fully coupled are, by our opinion, the most detailed thermal models of lithium ion batteries in the literature.

The source term q is here dependent on local electrochemical parameters obtained from an electrochemical model. Furthermore, as the electrochemical model parameters are temperature dependent, they are updated by the solutions of the thermal model.

A.2 Summary

Although advanced coupled electrochemical-thermal models are presented in the literature, more simple models are still applied. Hence, the source term A.5, is frequently used for various modeling and thermal analysis applications in the literature.

According Bandhauer et al. [2], the heat generation term (A.2) is the most frequent reported heat source term for thermal models in the literature. It can be applied to estimate the heat generation from electrochemical origins in the case when no heat from mixing and phase changes are present. Moreover should no spatial variations in state of charge occur. It is also applicable only when the temperature across a cell is uniform, when there is only one reaction occurring at each electrode, and when ohmic heating in the current collectors can be neglected [2]. However, side reactions and phase changes are normally not present in lithium ion batteries [2]. Furthermore, the heat of mixing is shown to be small [57]. However, spatial variations in state of charge, non-uniform temperature distributions, and ohmic heating in the current collectors may occur in the battery we model. Therefore we conclude that it may be an oversimplification to apply the source term (A.6).

Appendix B

Experimental Input Parameters

In this chapter we present results from experiments conducted on a commercial lithium ion pouch-cell. All input parameters obtained in this chapter are the results of experimental data provided by Senior Research Scientist Preben Vie at the Norwegian Institute for Energy Technology. The data are analyzed, used and published with permission from Dr. Preben Vie.

B.1 Irreversible Heat Generation

We present in this section measured data of the open-circuit potential U and the closed-circuit potential V. Moreover we estimate the difference between these two, i.e. $(U - V)$. We refer to this potential difference multiplied by the total cell current I as the irreversible heat generation, although a correct terminology would be irreversible heat generation rate. In the literature this potential difference is mostly measured directly [2], we therefore adapted this method also in this work.

B.1.1 Open and Closed-Circuit Potential

The closed-circuit data were obtained from cell potential measurements during a $1C-$discharge from 100 to 10% state of charge (SOC). Alternatively this can be expressed as from 0 to 90% depth of discharge (DOD). The potential is measured by a PEC battery tester at approximately 300 points during the discharge process. The current is constant during discharge, which for the $1C$ discharge corresponds to $I = 17.5$ (A). During this test the surface temperature of the battery is 23-24 ℃.

To obtain a mathematical representation for the closed-circuit potential V, we apply a 3. order polynomial regression approximation to these data. This offers the possibility to compare the closed-circuit potential with results from other tests at corresponding DOD at points not represented by this data set. This advantage are utilized later in this section.

Let us denote the dimensionless depth of discharge as σ. The regression equation then reads

$$V = a_v\sigma^3 + b_v\sigma^2 + c_v\sigma + d_v \tag{B.1}$$

Here a_v, b_v, c_v and d_v are constants measured in (V), respectively. The constants are given in table B.1.

Table B.1: Regression coefficients

$a_v =$	$-1.444 \cdot 10^{-6}$	(V)
$b_v =$	$8.008 \cdot 10^{-5}$	(V)
$c_v =$	$-1.247945 \cdot 10^{-2}$	(V)
$d_v =$	4.04037689	(V)

We define the coefficient of determination [42] as R^2.

For this approximation $R^2 = 0.9998$ is achieved.

The closed-circuit potential curve from the $1C$ discharge together with the polynomial regression approximation are presented in figure B.1 and figure B.2.

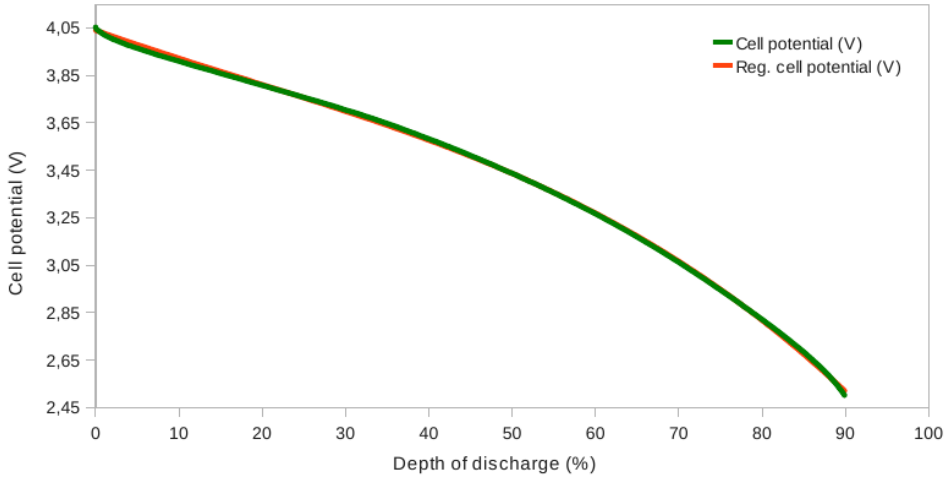

Figure B.1: Closed-circuit potential from $1C$ discharge with 3. order polynomial regression. Equation $V = a_v\sigma^3 + b_v\sigma^2 + c_v\sigma + d_v$. σ denotes depth of discharge. $R^2 = 0.9998$.

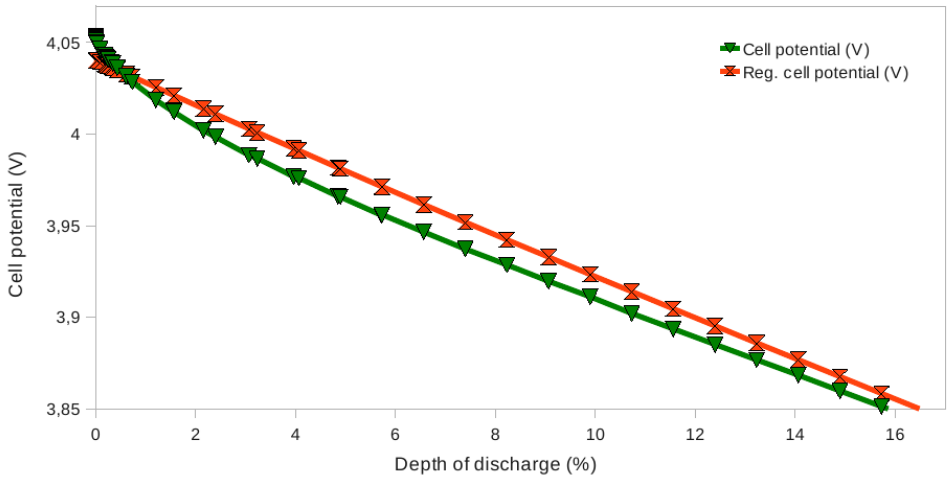

Figure B.2: Closed-circuit potential from $1C$ discharge with 3. order polynomial regression. Equation $V = a_v\sigma^3 + b_v\sigma^2 + c_v\sigma + d_v$. σ denotes depth of discharge. $R^2 = 0.9998$. Some discrepancy can be observed at low σ.

To estimate the open-circuit potential U as a function of the depth of discharge σ, we analyze data from a characterization test for lithium ion

batteries. The test is conducted with a PEC battery tester, and the relevant features in the test are now described shortly. It starts out with a fully charged battery and performs first a 30 seconds $1C$ discharge pulse. This pulse is followed by a 15 minutes zero-current period before a $2C$ current pulse of 30 seconds is performed. After this the current is again zero for 15 minutes before a 4 minutes $1C$ pulse discharges the battery such that the depth of discharge increases 10%. This step is followed by a 15 minutes zero-current period before the short $1C$ pulse is performed again. The test follows this cyclic pattern and ends with a long $1C$ pulse until the battery depth of discharge reaches about 90%. After the test the cell potential is measured during a 20 minutes zero-current period. We also note that the test starts out with a 10 minutes zero-current period. The history before this period is a $0.1C$ discharge over 30 minutes. During this test the surface temperature of the battery is 23-24 ℃. The current profile for a small period of the test is shown in figure B.3.

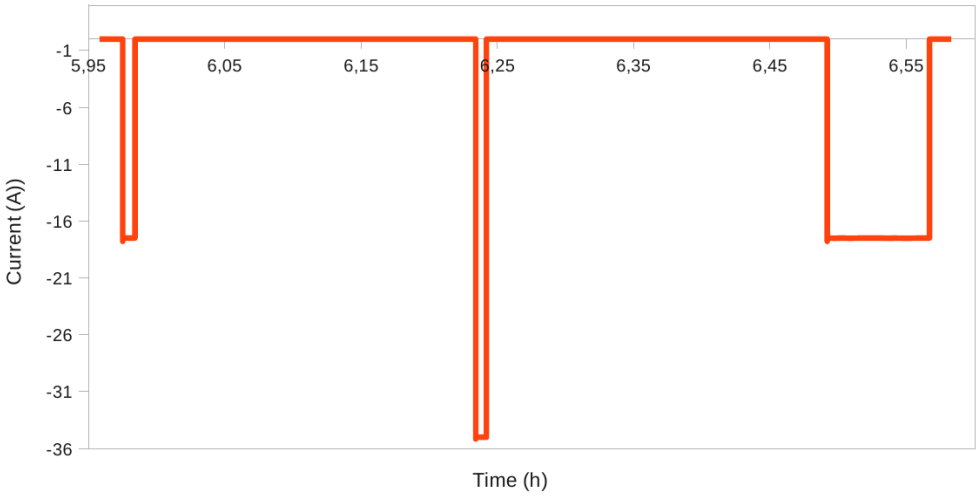

Figure B.3: Current profile for a short period of a characterization test for lithium ion batteries.

To obtain values of the open-circuit potential U for a given depth of discharge, we measure the potential 15 minutes after the current is cut off in the $1C$ discharge pulses in the characterization test. This is done for both the long and short pulses. Figure B.4 shows the cell potential first during open-circuit, then during 1C discharge from 23.5 to 40.0% depth of discharge followed by a period after the current is cut off. The first open-circuit period corresponds to the points in the graph where the potential

profile is horizontal. As the load is connected the current starts to flow causing a sudden drop in the voltage. The voltage decrease with time until the current is cut off, which can be observed as the lowest point in the curve. After this the potential increases again. The period after the current is cut off and before a stable cell potential is obtained is referred to as relaxation of the cell and is a process occurring as the cell is returning to an equilibrium state [2]. As described earlier, we register the open-circuit potential as the data point where time is 8.50 hours in figure B.4.

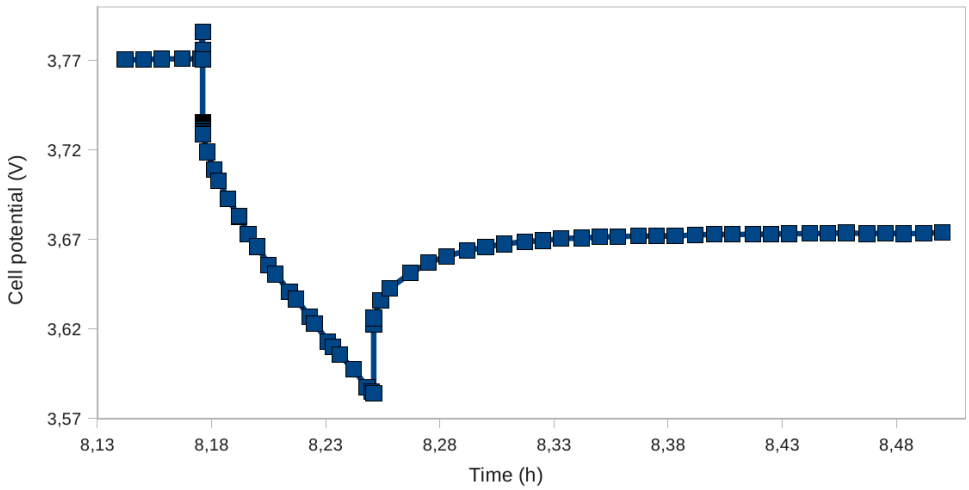

Figure B.4: Cell potential before and after $1C$ discharge pulse. The pulse causes a change in depth of discharge of 23.5-40%.

In this manner we obtain values for the open-circuit potential at various depth of discharges. We emphasize that the first data point of the open-circuit potential is measured 10 minutes after a $0.1C$ 30 minutes discharge. The rest of the data points are measured 15 minutes after the current is cut off from either a short or a long $1C$ discharge pulse.

The open-circuit potential after both the short and long pulses is plotted as separate data sets in figure B.5. As the figure shows, the two set of data follows each other rather close. This is shown when the figure is zoomed in, as can be observed in figure B.6. This may indicate that 15 minutes is sufficient to obtain an equilibrium potential. Alternatively, it may indicate that the relaxation state is similar after 15 minutes for both the short and the long pulse. We assume that an equilibrium potential is achieved after 15 minutes. Therefore, we apply the data from both the short and long pulses in our estimation of the open-circuit potential U.

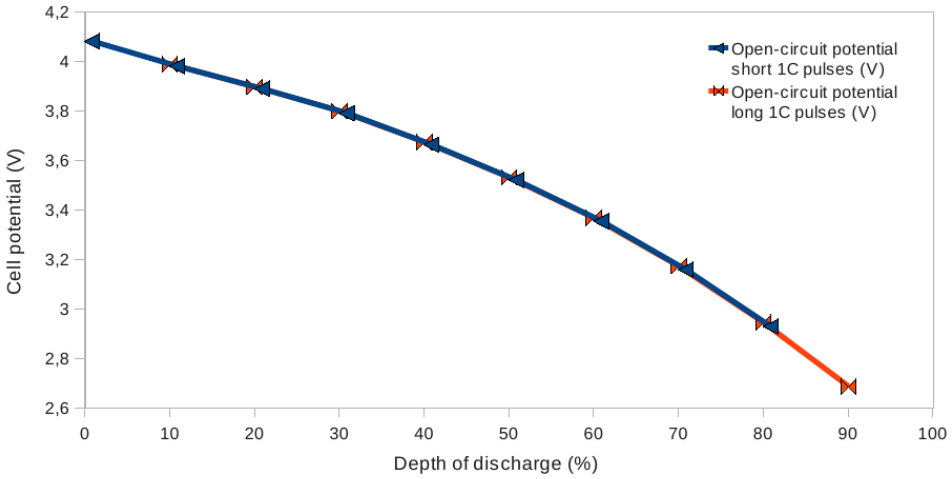

Figure B.5: Cell potential 15 minutes after short and long $1C$ discharge pulses, plotted as separate data sets.

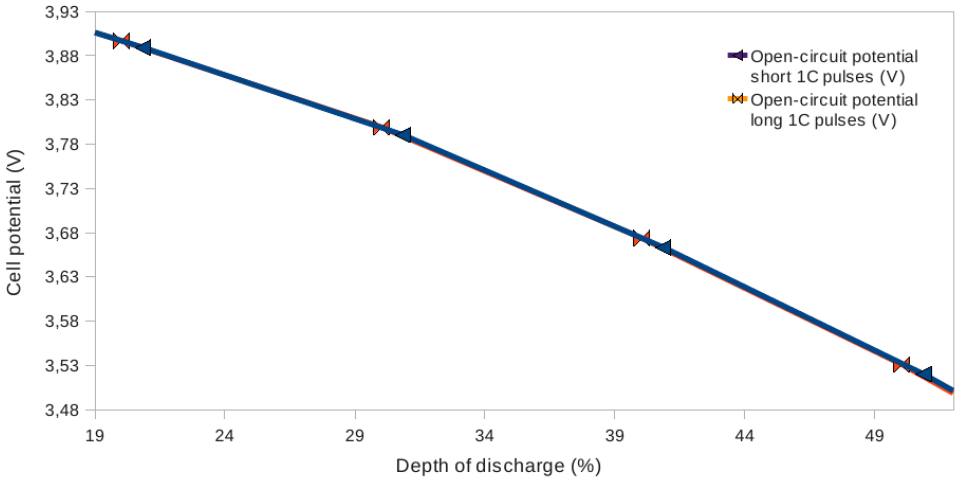

Figure B.6: Cell potential 15 minutes after short and long $1C$ discharge pulses, plotted as separate data sets. The data sets follows each other close.

The open-circuit potentials obtained from the characterization test are measured at relatively few points. To obtain corresponding values of U at the same depth of discharge as in the expression for the closed-circuit potential V, we apply a 3. order polynomial regression to these data.

The regression equation are expressed as follows:

$$U = a_u\sigma^3 + b_u\sigma^2 + c_u\sigma + d_u \tag{B.2}$$

Here a_u, b_u, c_u and d_u are constants measured in (V), respectively. The constants are given in table B.2.

Table B.2: Regression coefficients

$a_u =$	$-7.8 \cdot 10^{-7}$	(V)
$b_u =$	$-3.66 \cdot 10^{-6}$	(V)
$c_u =$	$-8.91275 \cdot 10^{-3}$	(V)
$d_u =$	4.08550120	(V)

For this approximation $R^2 = 0.9999$ is achieved.

The open-circuit potential curve together with the polynomial regression approximation are presented in figure B.7 and figure B.8.

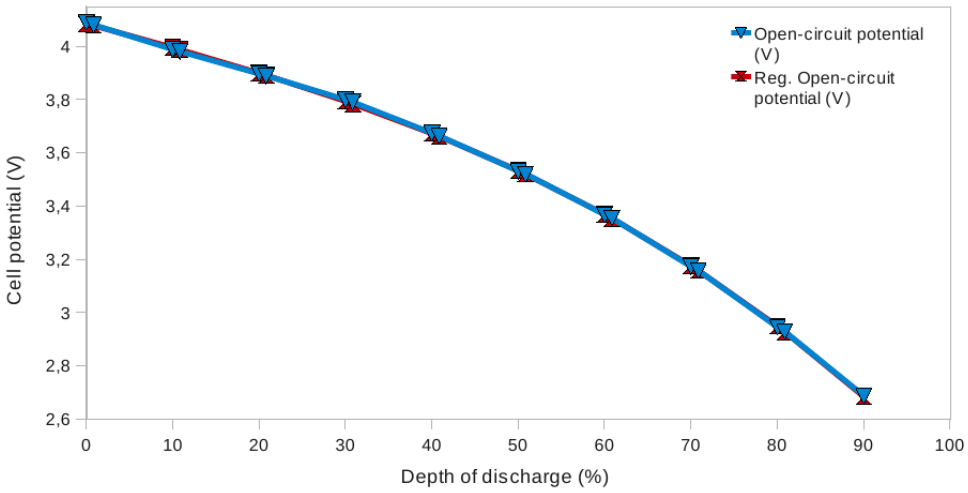

Figure B.7: Open-circuit potential with 3. order polynomial regression. Equation $U = a_u\sigma^3 + b_u\sigma^2 + c_u\sigma + d_u$. σ denotes depth of discharge. $R^2 = 0.9999$.

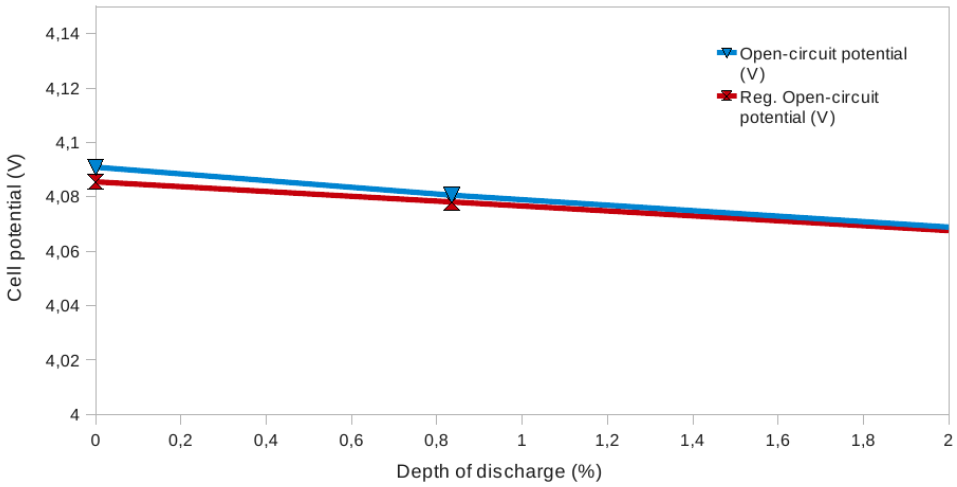

Figure B.8: Open-circuit potential with 3. order polynomial regression. Equation $U = a_u\sigma^3 + b_u\sigma^2 + c_u\sigma + d_u$. σ denotes depth of discharge. $R^2 = 0.9999$. Some discrepancy can be observed at low σ.

We present data from the closed-circuit potential V from a $1C$ continuous discharge test. However, it is also interesting to study the closed-circuit potential V in the $1C$ discharge pulses in the characterization test. We plot the closed-circuit potential V in the point just before the current is interrupted. This means a closed-circuit potential V taken approximately 30 seconds or 4 minutes after the current is turned on, for the two different pulses. The closed-circuit potential V from these pulses and from the regression representation of the continuous discharge is shown in figures B.9-B.10.

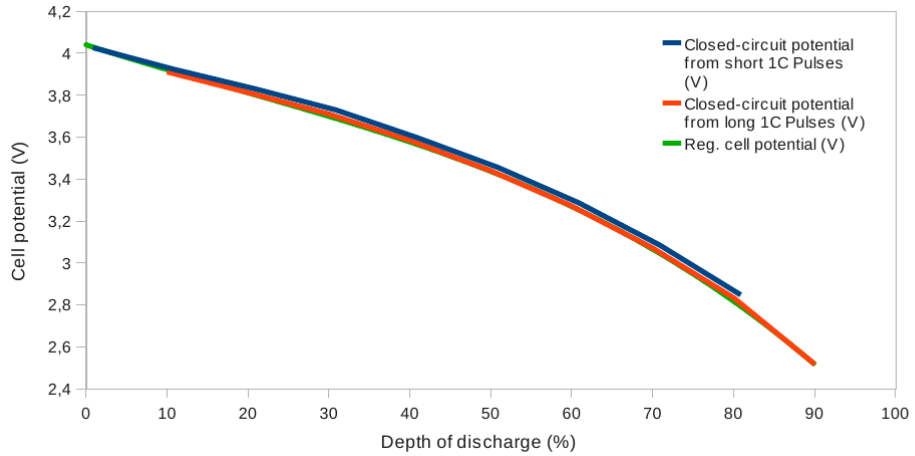

Figure B.9: Closed-circuit potential V from pulses and from regression of continuous discharge.

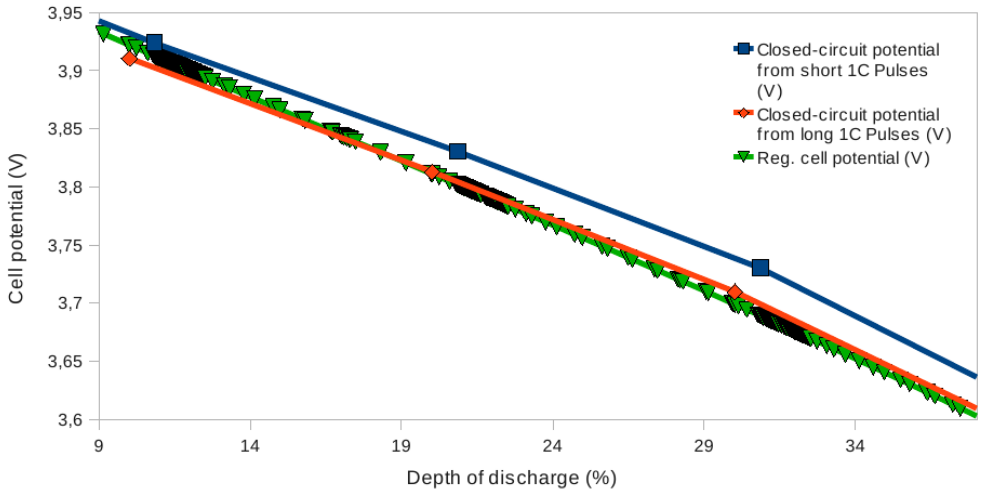

Figure B.10: Closed-circuit potential V from pulses and from regression of continuous discharge. The potential from the short pulses are clearly higher than for the long pulses, which follows the continuous discharge potential rather close.

As figure B.10 shows, the closed-circuit potential is higher for the shorter pulses. We further observe that the closed-circuit potential from the long

pulses follows the regression potential representation of the continuous curve quite close. This indicates that at $1C$ discharge, the potential does not drop more if longer pulses than 4 minutes are imposed at a given depth of discharge.

We need an expression for the difference between the open-circuit and the closed-circuit potential, i.e. $(U - V)$. We choose to apply the data from the continuous discharge test to represent V in further estimations. The potential difference $(U - V)$ is calculated by the regression approximations of the potentials from the characterization test and from the $1C$ continuous discharge test, respectively. We emphasize that U and V correspond as functions of depth of discharge despite they are from different tests. This is possible since the depth of discharge is a parameter that is independent of cell potential.

The equation for the potential difference thus reads

$$U - V = \tilde{a}\sigma^3 + \tilde{b}\sigma^2 + \tilde{c}\sigma + \tilde{d} \tag{B.3}$$

Here $\tilde{a}$, $\tilde{b}$, $\tilde{c}$ and $\tilde{d}$ are constants measured in (V), respectively. The constants are defined in table B.3.

Table B.3: Polynomial coefficients

$\tilde{a} =$	$(a_u - a_v) =$	$6.2 \cdot 10^{-7}$	(V)
$\tilde{b} =$	$(b_u - b_v) =$	$-8.374 \cdot 10^{-5}$	(V)
$\tilde{c} =$	$(c_u - c_v) =$	$3.566650 \cdot 10^{-3}$	(V)
$\tilde{d} =$	$(d_u - d_v) =$	$4.51243100 \cdot 10^{-2}$	(V)

Figure B.11 shows a plot of the potential difference between U and V:

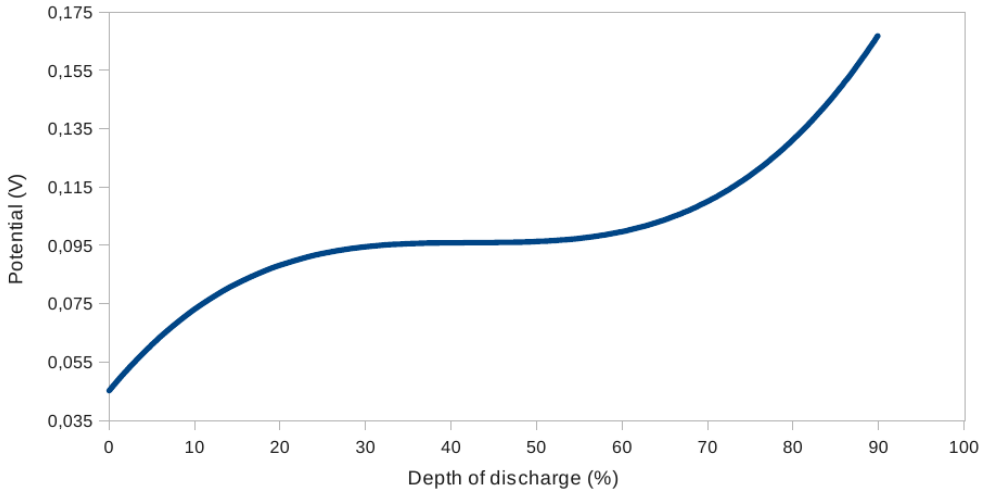

Figure B.11: 3. order polynomial regression approximation of the difference between U and V. U: Open-circuit potential. V: Closed-circuit potential. Equation $U - V = \tilde{a}\sigma^3 + \tilde{b}\sigma^2 + \tilde{c}\sigma + \tilde{d}$. σ: Depth of discharge.

The irreversible heat generation rate can also be considered as a function of the total internal resistance multiplied by the total cell current I. We calculate the total internal resistance for the characterization test. This is done by taking the difference between the open-circuit potential U, and the closed circuit potential V at the end of each current pulse. Thereafter this difference is divided with the current I at the moment the closed-circuit potential V is registered. The PEC battery tester also calculates the pure electric resistance in the cells. We present the calculated total internal resistance together with the pure electric resistance in figure B.12.

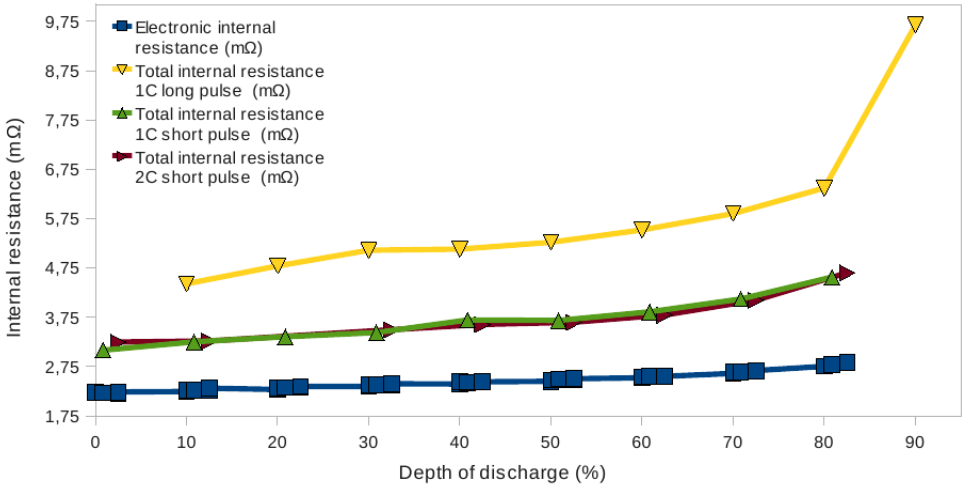

Figure B.12: Total internal resistance on long $1C$ pulses, short $1C$ pulses and short $2C$ pulses are shown together with pure electric resistance.

The information provided on the internal resistance could be used to separate the different heat generating mechanisms in the battery. This opens the possibility of distributing different heating effects locally inside the battery. We do not apply the internal resistance in our model, however.

B.2 Reversible Heat Generation

In this section we present experiments performed to estimate the entropic heat coefficient $\frac{\partial U}{\partial T}$. Since this reversible contribution in the heat source term could be in the same order of magnitude as the irreversible contribution [17], we are motivated to estimate this coefficient. An estimation method frequently reported in the literature is to measure the open-circuit potential U of the cell while the temperature T is varied at a given state of charge [2]. This method is adopted in our study. The tests are performed in Thermax climatic chambers where the cells are exposed to temperature changes, both from high temperature to low temperature “warmup“ and vice versa ”cooldown”. While the temperature in the chambers changes, the surface temperature of the cells is measured with thermocouples and the cell voltages are registered by a PEC battery tester. As the entropic heat coefficient is known to vary with state of charge [58], we conducted measurements on 80% and at 50% state of charge.

B.2.1 Entropic Heat Coefficient at 80% SOC

For the tests conducted at 80% SOC, experimental data for some hours after the heating process are available. This allows a study of the self-discharge of the cells, which may affect the data for the entropic heat coefficient. All data of the cells at 80% SOC are data from warmup processes.

Test 1

As figure B.13 shows, the surface temperature is steady over a 4 hour period after warmup. We can therefore study the decrease in cell potential over this period and assume it is related to self-discharge only. The test cell in figure B.13 is referred to as test cell A.

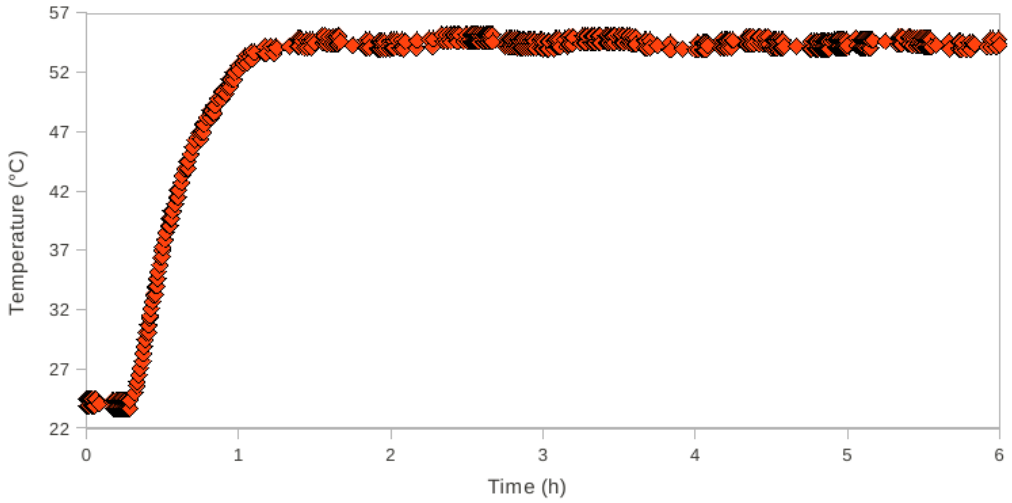

Figure B.13: Surface temperature of test cell A at 80% SOC measured during and after a warmup period.

The cell potential for the constant-temperature period of 4 hours at approximately 55 ℃ for test cell A is shown in figure B.14. A linear regression fit to the cell potential as a function of time shows a decrease in cell potential rate of 4.7 (mV/h) with $R^2 = 0.98$.

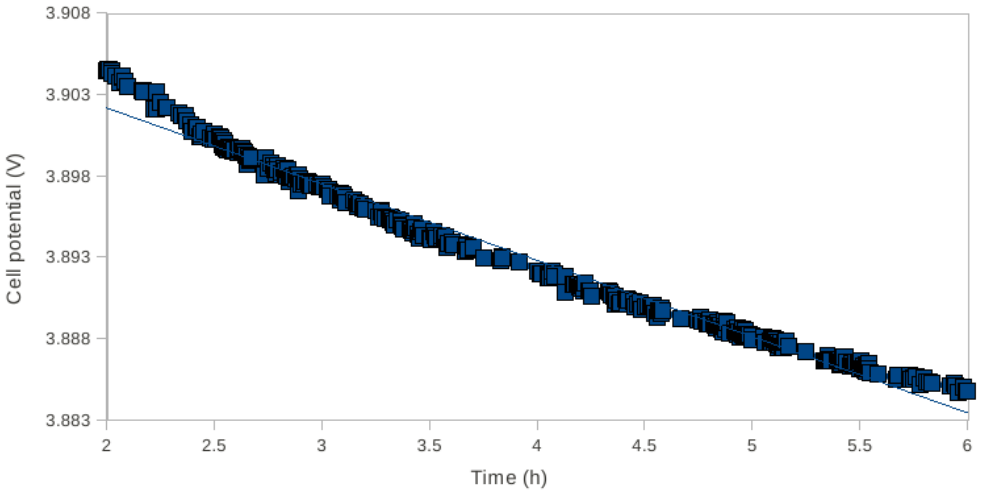

Figure B.14: Cell potential of test cell A at 80% SOC during a constant temperature period of 4 hours at approximately 55 ℃. A linear regression fit to these data shows a decrease rate in cell potential of 4.7 (mV/h) with $R^2 = 0.98$.

To study the self-discharge at a lower temperature, a short period in time with constant temperature before the warmup process starts can be examined. This period for test cell A is shown in figure B.15, and the corresponding self-discharge is shown in figure B.16.

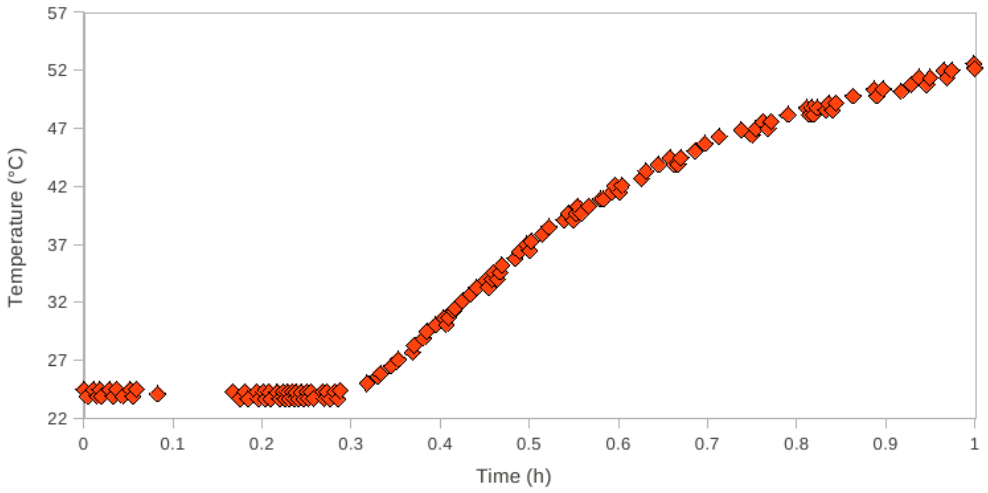

Figure B.15: Surface temperature for test cell A at 80% SOC measured before and during a warmup period.

The self-discharge at 25 ℃ for this cell differ substantially from the self-discharge at 55 ℃. A linear regression fit to the cell potential as a function of time at 25 ℃ shows a decrease in cell potential rate of 8.6 (mV/h) with $R^2 = 0.91$. This implies that the self-discharge may vary with temperature.

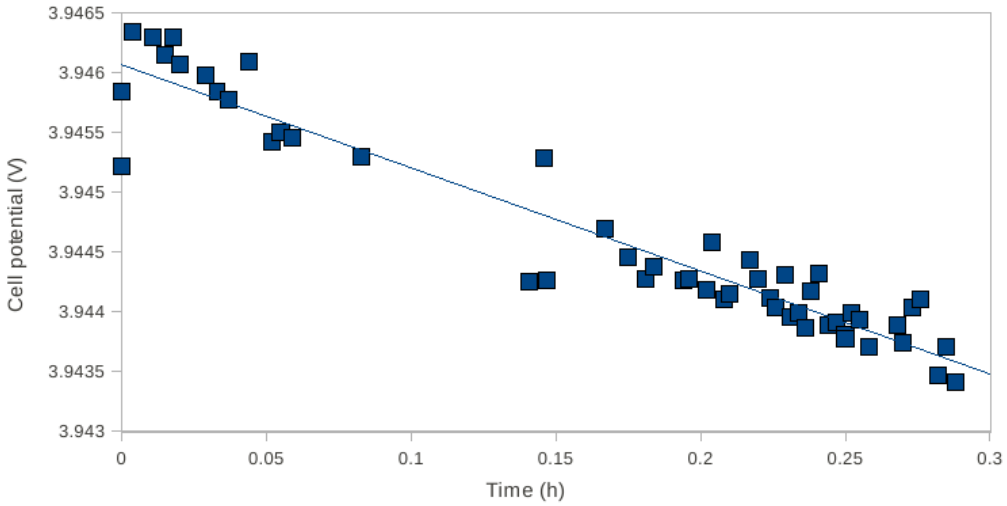

Figure B.16: Cell potential for test cell A at 80% SOC during a constant temperature period of 0.3 hours at approximately 25 ℃. A linear regression fit to these data shows a decrease rate in cell potential of 8.6 (mV/h) with a $R^2 = 0.91$.

Figure B.17 shows the change in cell potential for test cell A plotted against temperature during the warmup period only.

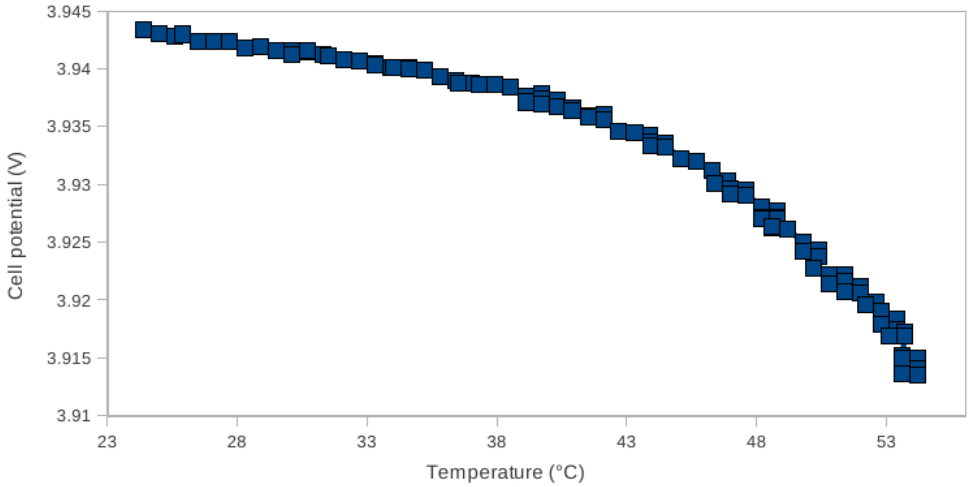

Figure B.17: Cell potential of test cell A at 80% SOC during a warmup period of 1 hour. A linear regression fit to these data seems not appropriate due to the obvious nonlinear trend.

As figure B.17 shows, test cell A seems to have a nonlinear relation between the cell potential U and the temperature T.

Test 2

A similar examination can be performed to the test cell B. This cell obtains a stable temperature after approximately 3 hours, which can be observed in figure B.18.

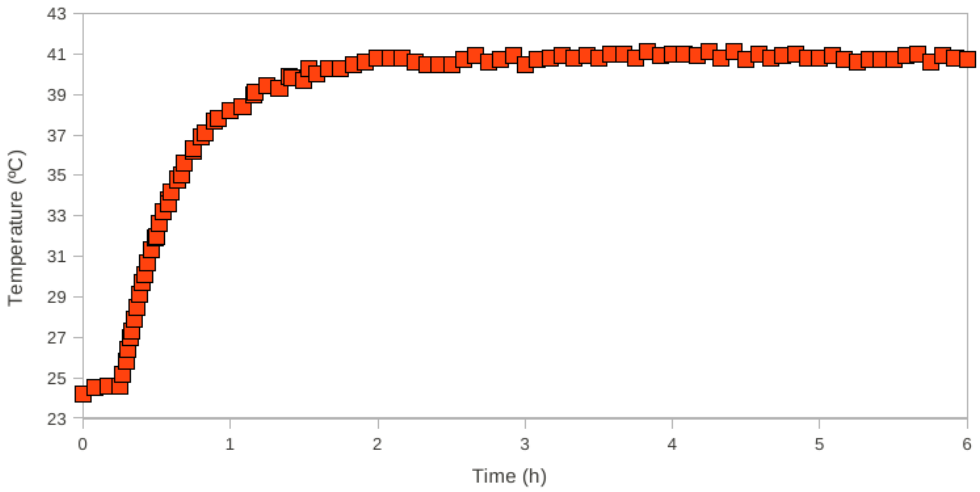

Figure B.18: Surface temperature of test cell B at 80% SOC measured during and after a warmup period.

The cell potential during the constant-temperature period of 3 hours at 41 ℃ for test cell B is shown in figure B.19. A linear regression fit to the cell potential as a function of time shows a decrease in cell potential rate of 0.90 (mV/h) with $R^2 = 0.71$.

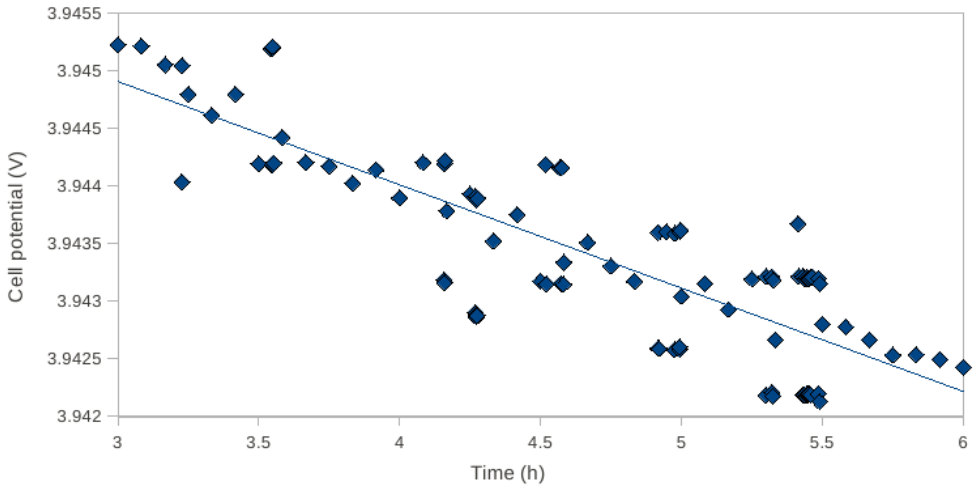

Figure B.19: Cell potential of test cell B at 80% SOC during a constant temperature period of 3 hours at approximately 41 ℃. A linear regression fit to these data shows a decrease rate in cell potential of 0.90 (mV/h) with $R^2 = 0.71$.

Figure B.20 shows the change in cell potential for test cell B plotted against the temperature during the warmup period only. A linear regression fit to these data results in an entropic heat coefficient of $\frac{\partial U}{\partial T} = -0.46$ (mV/K) with $R^2 = 0.95$.

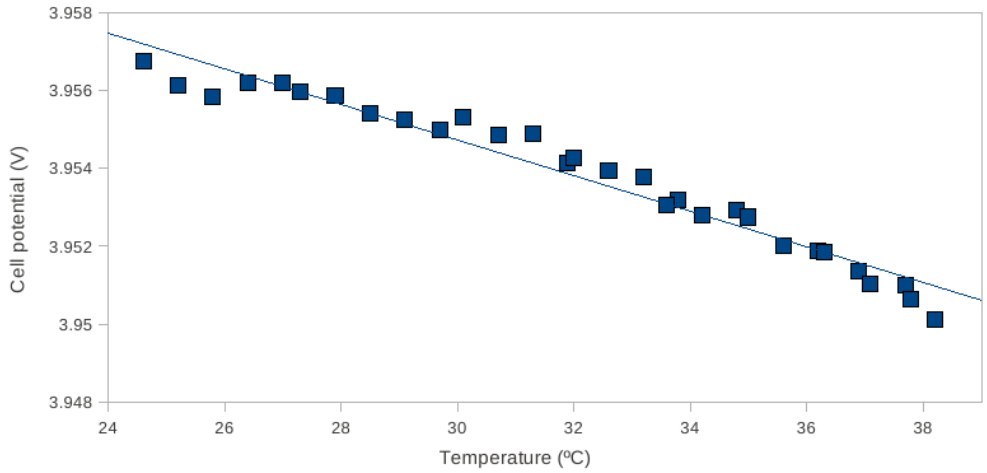

Figure B.20: Cell potential of test cell B at 80% SOC during a warmup period of 0.75 hour. A linear regression fit to these data results in an entropic heat coefficient of $\frac{\partial U}{\partial T} = -0.46$ (mV/K) with $R^2 = 0.95$.

To obtain an overview of whether the self-discharge is capable of affecting the results for the entropic heat coefficient, we do the following simple analysis. We consider the self-discharge measured on test cell B, which is 0.90 mV/h at 41 ℃. We assume that the self-discharge remains constant at 0.90 mV per hour during the warmup period of 0.75 hour (which may not be a valid assumption since the temperature increases). This yields a cell potential decrease related to self-discharge alone during this period of 0.68 mV. Thus the absolute value of the potential change related to the change in temperature for the warmup period is 0.68 mV to high. We then estimate a corrected entropic heat coefficient, i.e.

$$(\frac{\partial U}{\partial T})_{corr} \approx \frac{(\Delta U)_{corr}}{\Delta T} \tag{B.4}$$

where *corr* denotes the corrected values. Obviously, ΔT is the same. We have the regression expression for the uncorrected entropic heat coefficient, i.e.

$$\frac{\partial U}{\partial T} \approx \frac{\Delta U}{\Delta T} = -0.46\ (mV/K) \tag{B.5}$$

Dividing (B.4) with (B.5) results in

$$\frac{(\frac{\partial U}{\partial T})_{corr}}{\frac{\partial U}{\partial T}} = \frac{\Delta U_{corr}}{\Delta U} \tag{B.6}$$

Moreover we assume the relation

$$\Delta U_{corr} = \Delta U + 0.68\ (mV) \tag{B.7}$$

$$\frac{(\frac{\partial U}{\partial T})_{corr}}{\frac{\partial U}{\partial T}} = \frac{\Delta U + 0.68\ (mV)}{\Delta U} \tag{B.8}$$

We find that ΔU during this 0.75 hour period is -6.6 mV. By this we obtain the value for the estimated corrected entropic heat coefficient, i.e.

$$(\frac{\partial U}{\partial T})_{corr} = \frac{\partial U}{\partial T}(1 - \frac{0.68}{6.6}) = -0.41\ mV/K \tag{B.9}$$

which yields an error of approximately 11%.

Test 3

We now perform an examination of test cell C. This cell obtains a stable temperature after approximately 3 hours, which can be observed in figure B.21.

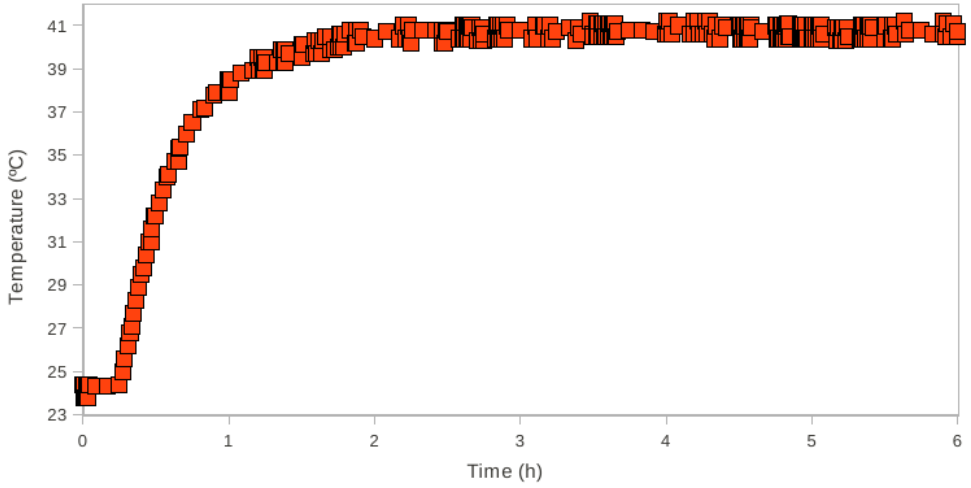

Figure B.21: Surface temperature of test cell C at 80% SOC measured during and after a warmup period.

The cell potential for the constant-temperature period of 3 hours at 40 ℃ for test cell C is shown in figure B.22. A linear regression fit to the cell potential as a function of time shows a decrease in cell potential rate of 0.88 (mV/h) with $R^2 = 0.81$.

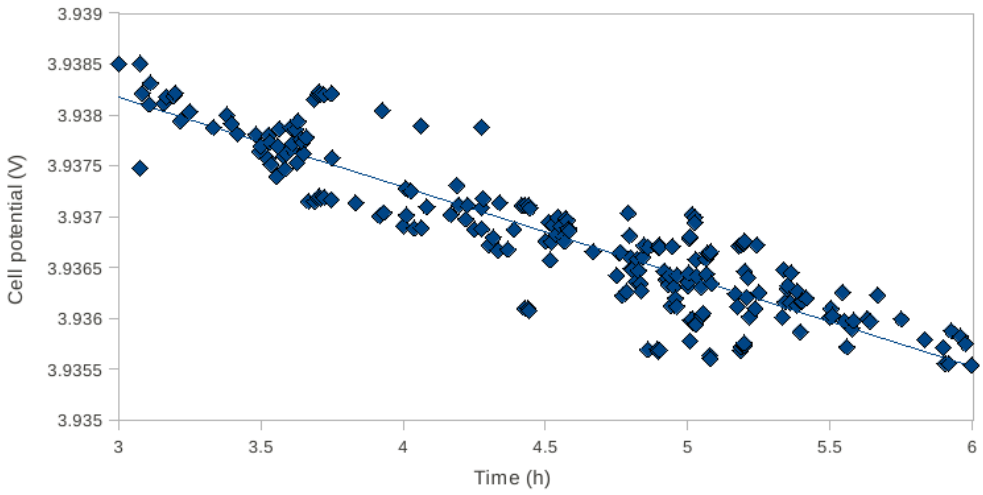

Figure B.22: Cell potential of test cell C at 80% SOC during a constant temperature period of 3 hours at 40 ℃. A linear regression fit to these data shows a decrease rate in cell potential of 0.88 (mV/h) with $R^2 = 0.81$.

Figure B.23 shows the change in cell potential for test cell C plotted against the temperature during the warmup period only. A linear regression fit to these data results in an entropic heat coefficient of $\frac{\partial U}{\partial T} = -0.42$ (mV/K) with $R^2 = 0.94$.

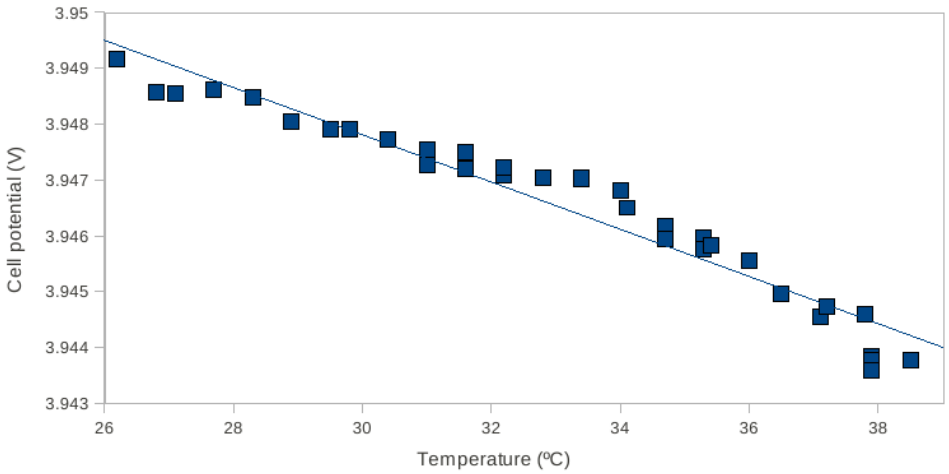

Figure B.23: Cell potential of test cell C at 80% SOC during a warmup period of 0.7 hour. A linear regression fit to these data results in an entropic heat coefficient of $\frac{\partial U}{\partial T} = -0.42$ (mV/K) with $R^2 = 0.94$.

Test 4

We perform a similar examination of test cell D. This cell obtains a stable temperature after approximately 2 hours, which can be observed in figure B.24.

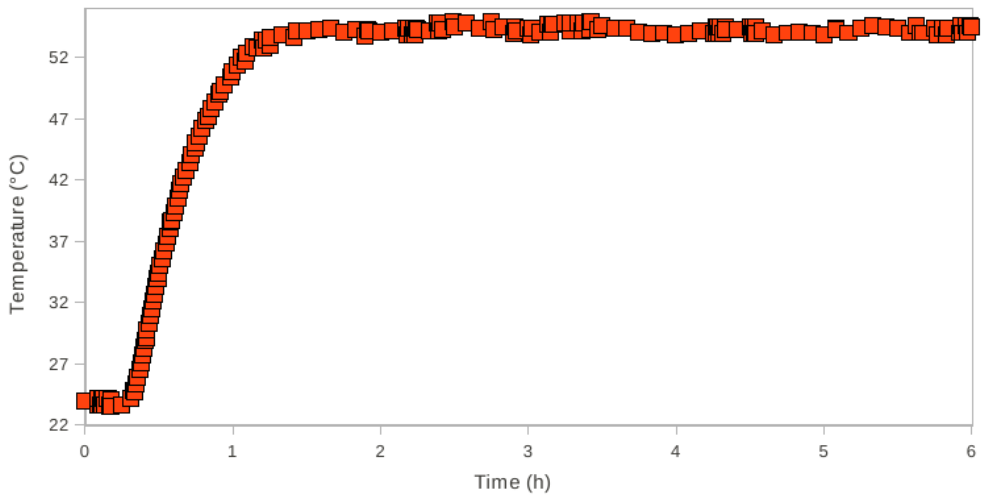

Figure B.24: Surface temperature of test cell D at 80% SOC measured during and after a warmup period.

The cell potential for the constant-temperature period of 4 hours at 55 ℃ for test cell D is shown in figure B.25. A linear regression fit to the cell potential as a function of time shows a decrease in cell potential rate of 1.8 (mV/h) with $R^2 = 0.97$.

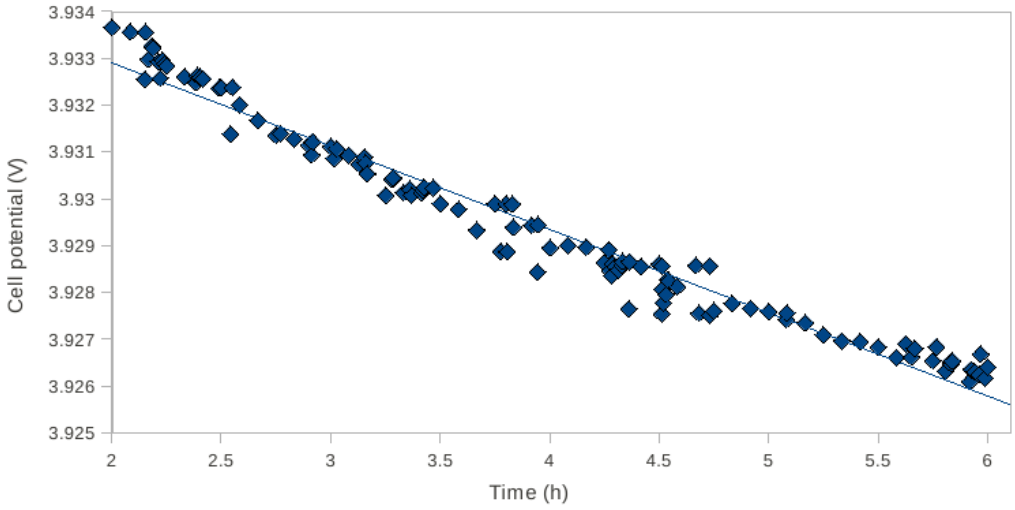

Figure B.25: Cell potential of test cell D at 80% SOC during a constant temperature period of 4 hours at approximately 55 ℃. A linear regression fit to these data shows a decrease rate in cell potential of 1.8 (mV/h) with $R^2 = 0.97$.

Figure B.26 shows the change in cell potential for test cell D plotted against temperature during the warmup period only. A linear regression fit to these data results in a entropic heat coefficient of $\frac{\partial U}{\partial T} = -0.59$ (mV/K) with $R^2 = 0.99$.

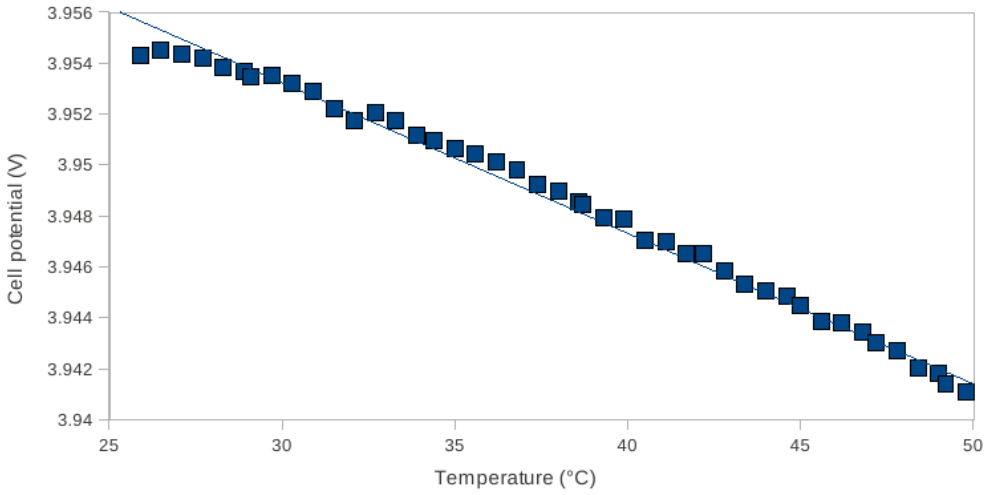

Figure B.26: Cell potential of test cell D at 80% SOC during a warmup period of 0.64 hour. A linear regression fit to these data results in a entropic heat coefficient of $\frac{\partial U}{\partial T} = -0.59$ (mV/K) with $R^2 = 0.99$.

Test 5

We perform a similar examination of test cell E. This cell obtains a stable temperature after approximately 3 hours, which can be observed in figure B.27.

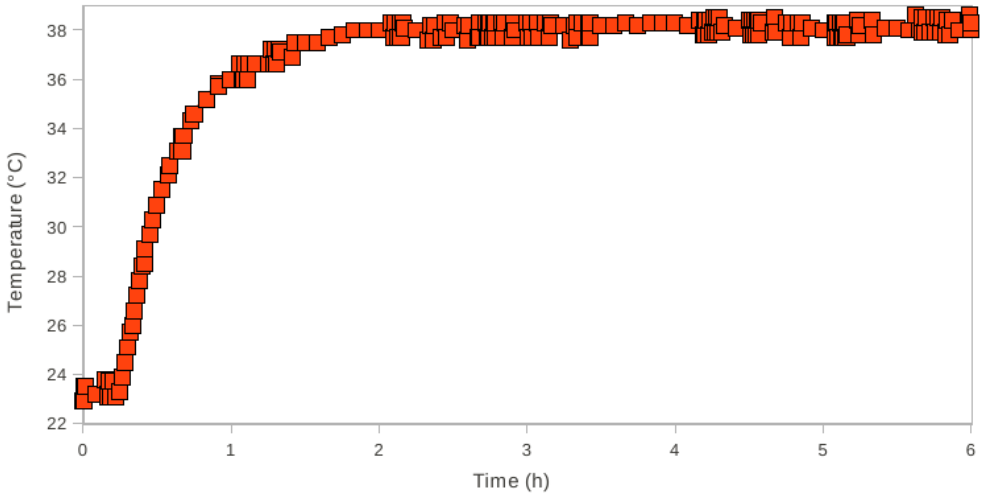

Figure B.27: Surface temperature of test cell E at 80% SOC measured during and after a warmup period.

The cell potential for the constant-temperature period of 3 hours at 38 ℃ for test cell E is shown in figure B.28. A linear regression fit to the cell potential as a function of time shows a decrease in cell potential rate of 0.82 (mV/h) with $R^2 = 0.58$.

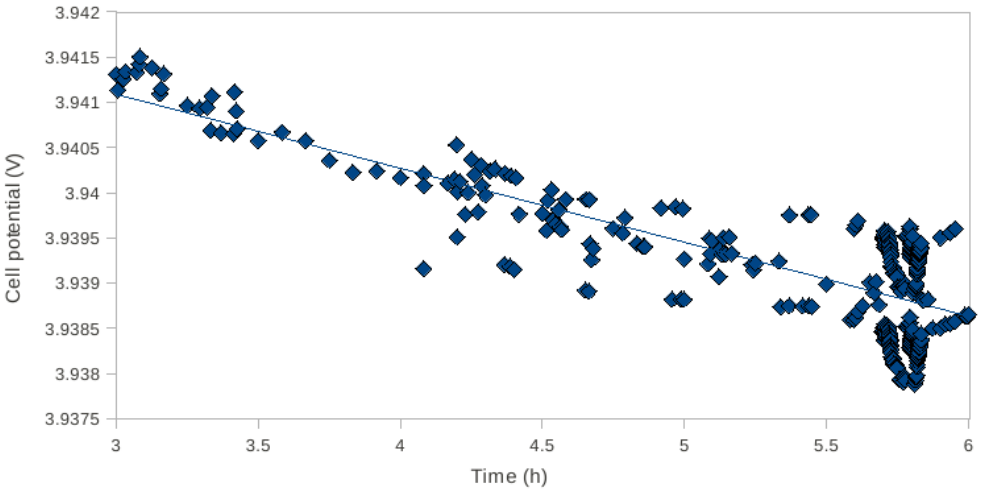

Figure B.28: Cell potential of test cell E at 80% SOC during a constant temperature period of 3 hours at approximately 38 ℃. A linear regression fit to these data shows a decrease rate in cell potential of 0.82 (mV/h) with $R^2 = 0.58$.

Figure B.29 shows the change in cell potential for test cell E plotted against the temperature during the warmup period only. A linear regression fit to these data results in an entropic heat coefficient of $\frac{\partial U}{\partial T} = -0.45$ (mV/K) with $R^2 = 0.95$.

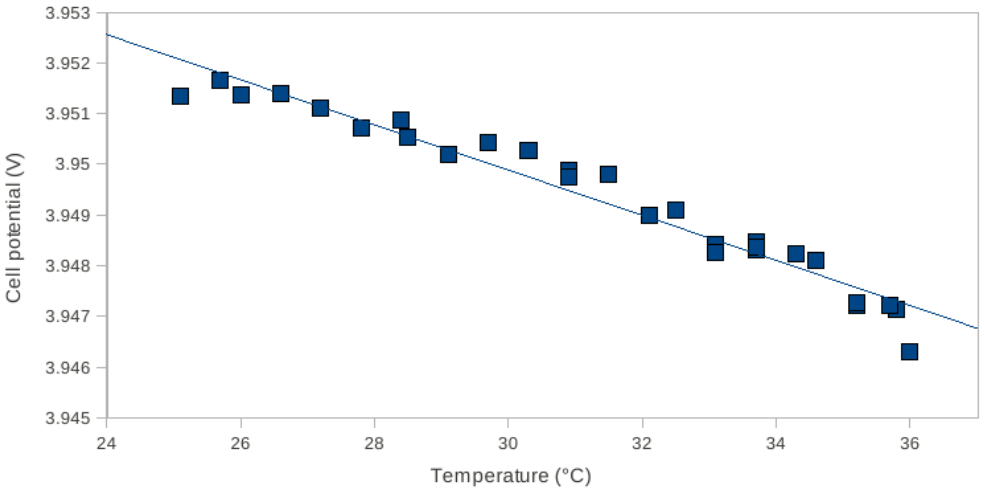

Figure B.29: Cell potential of test cell E at 80% SOC during a warmup period of 0.7 hour. A linear regression fit to these data results in a entropic heat coefficient of $\frac{\partial U}{\partial T} = -0.45$ (mV/K) with $R^2 = 0.95$.

The results of Test 1 - Test 6 are summarized in table B.4. The results from Test 1 are summarized in the first two rows. Thereafter the results from the tests are summarized in the order they are presented. As table B.4 shows, test cell A seems to have a high self-discharge compared with the other cells. We therefore exclude data of test cell A in further studies.

Table B.4: Entropic heat coefficient and self-discharge at 80% SOC

Test cell	$\frac{\partial U}{\partial T}$ (mV/K)	R^2	Self discharge (mV/h)	T (°C)	R^2
A	-	-	4.7	55	0.98
A	-	-	8.6	25	0.91
B	-0.46	0.95	0.90	41	0.71
C	-0.42	0.94	0.88	40	0.81
D	-0.59	0.99	1.8	55	0.97
E	-0.45	0.95	0.82	38	0.58

B.2.2 Entropic Heat Coefficient at 50% SOC

We perform the same experiments on 50% SOC as we did on 80% SOC. However, at 50% SOC data for the self-discharge are less sufficient. Nevertheless are the data here both from warmup and cooldown processes.

Test 6

Figure B.30 shows the change in cell potential for test cell F plotted against the temperature during the warmup period only. A linear regression fit to these data results in an entropic heat coefficient of $\frac{\partial U}{\partial T} = -0.11$ (mV/K) with $R^2 = 0.97$. No data for the self-discharge are available.

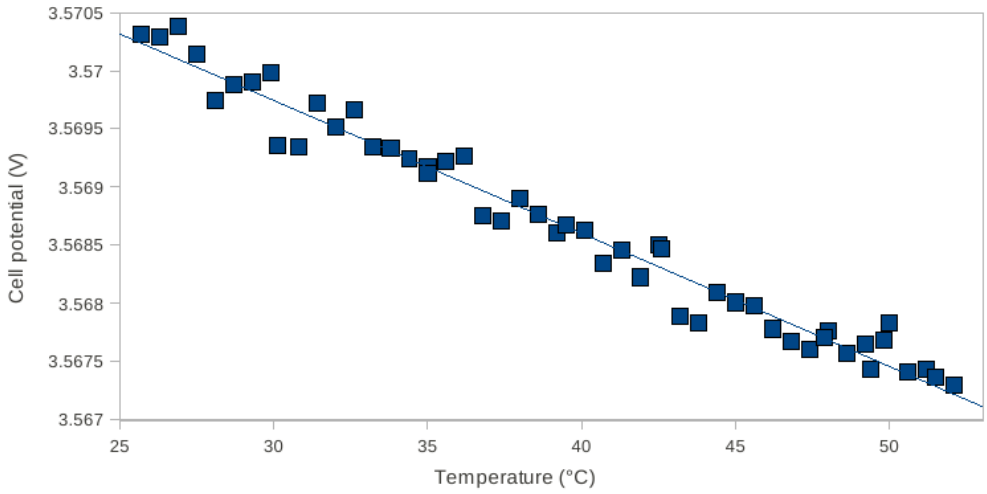

Figure B.30: Cell potential of test cell F at 50% SOC during a warmup period of 0.7 hour. A linear regression fit to these data results in an entropic heat coefficient of $\frac{\partial U}{\partial T} = -0.11$ (mV/K) with $R^2 = 0.97$.

Test 7

We perform a similar examination of test cell A. Figure B.31 shows the change in cell potential for test cell A plotted against temperature during the cooldown period only. A linear regression fit to these data results in an entropic heat coefficient of $\frac{\partial U}{\partial T} = -0.11$ (mV/K) with $R^2 = 0.97$. No data for the self-discharge are available.

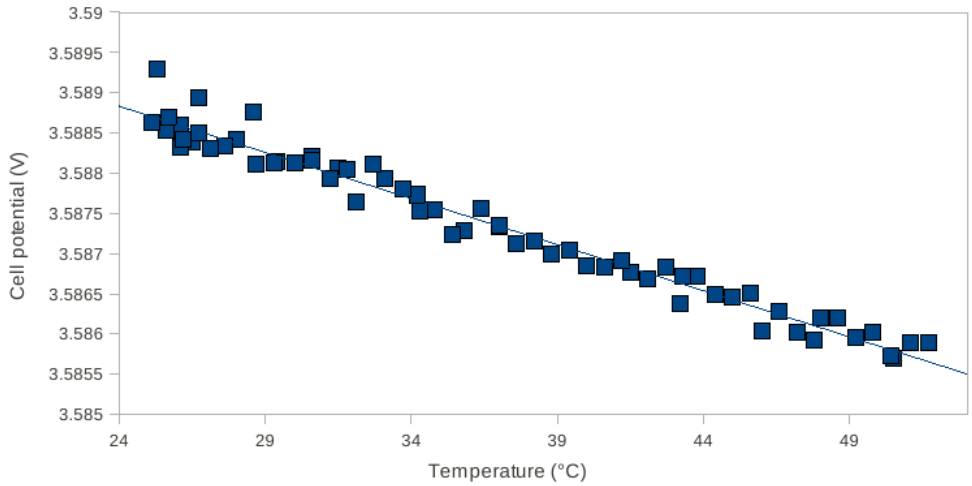

Figure B.31: Cell potential of test cell A at 50% SOC during a cooldown period of 1.64 hour. A linear regression fit to these data results in an entropic heat coefficient of $\frac{\partial U}{\partial T} = -0.11$ (mV/K) with $R^2 = 0.97$.

Test 8

We perform another examination of test cell A. In this test, the cell obtains a stable temperature after approximately 2 hours, which can be observed in figure B.32.

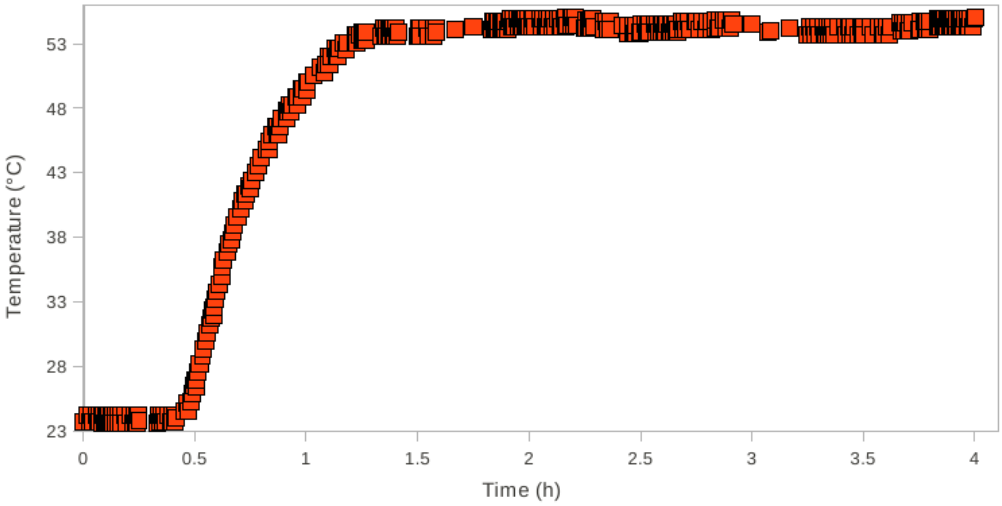

Figure B.32: Surface temperature of test cell A at 50% SOC measured during and after a warmup period.

The cell potential for the constant-temperature period of 2 hours at 54 ℃ for test cell A is shown in figure B.33. As the figure indicates, there is no clear trend for the self-discharge.

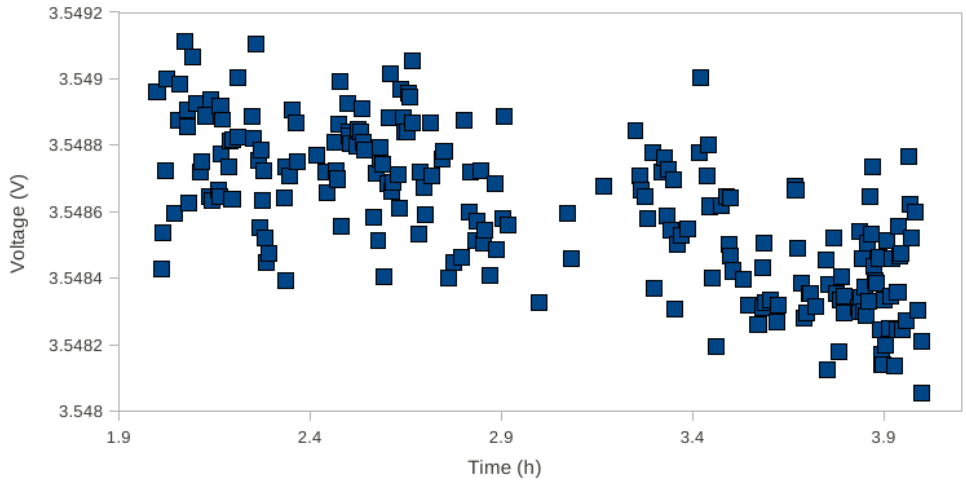

Figure B.33: Cell potential of test cell A at 50% SOC during a constant temperature period of 2 hours at 54 ℃. The data provides no clear trend for the self-discharge.

Figure B.34 shows the change in cell potential for test cell A plotted against the temperature during the warmup period only. A linear regression fit to these data results in an entropic heat coefficient of $\frac{\partial U}{\partial T} = -0.12$ (mV/K) with $R^2 = 0.97$.

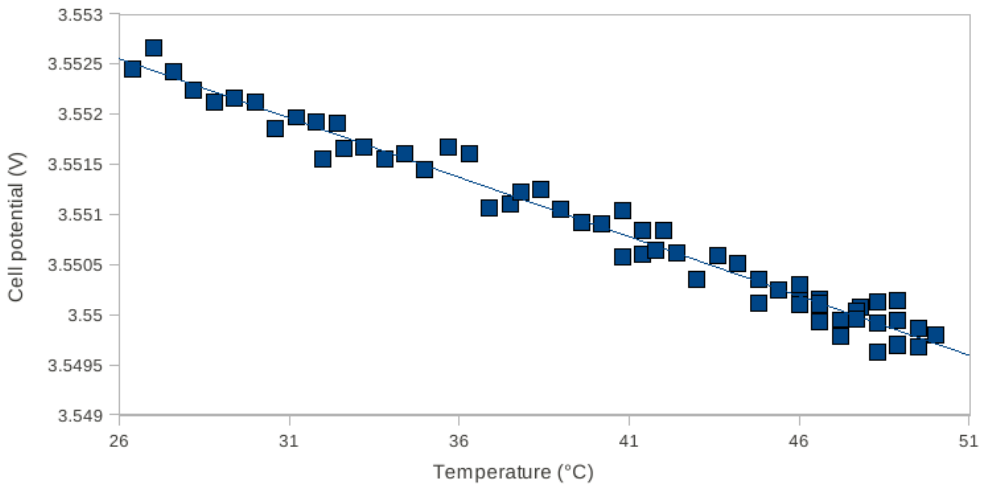

Figure B.34: Cell potential of test cell A at 50% SOC during a warmup period of 0.5 hour. A linear regression fit to these data results in an entropic heat coefficient of $\frac{\partial U}{\partial T} = -0.12$ (mV/K) with $R^2 = 0.97$.

Test 9

We performed another test of test cell A. Figure B.35 shows the change in cell potential for test cell A plotted against the temperature during a warmup period only. A linear regression fit to these data results in an entropic heat coefficient of $\frac{\partial U}{\partial T} = -0.35$ (mV/K) with $R^2 = 0.98$. No data for the self-discharge are available.

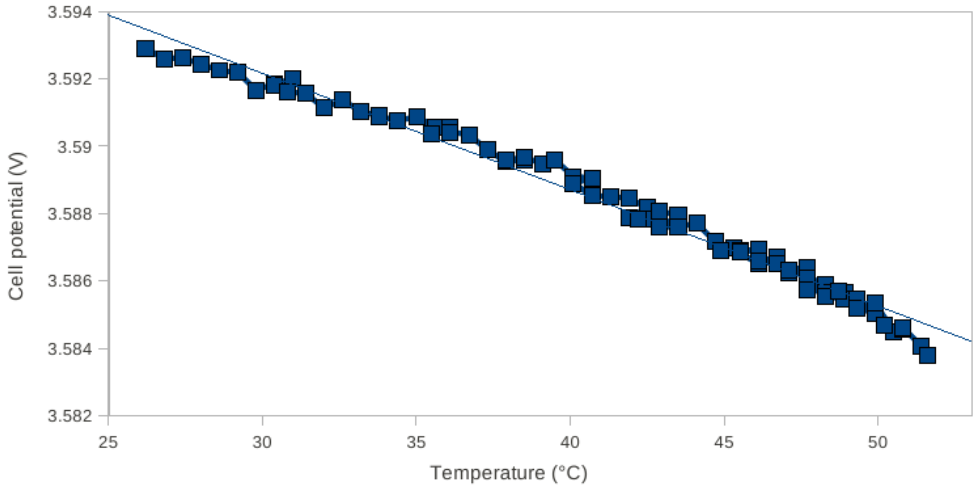

Figure B.35: Cell potential of test cell A at 50% SOC during a warmup period of 0.75 hour. A linear regression fit to these data results in an entropic heat coefficient of $\frac{\partial U}{\partial T} = -0.35$ (mV/K) with $R^2 = 0.98$.

Test 10

We perform an examination of test cell B. Figure B.36 shows the change in cell potential for test cell B plotted against temperature during the warmup period only. A linear regression fit to these data results in an entropic heat coefficient of $\frac{\partial U}{\partial T} = -0.11$ (mV/K) with $R^2 = 0.85$. No data for the self-discharge are available.

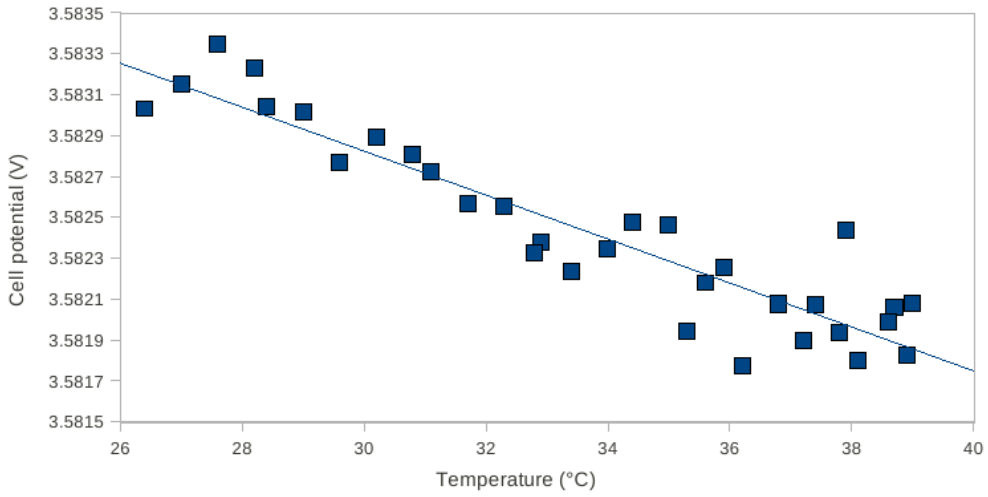

Figure B.36: Cell potential of test cell B at 50% SOC during a warmup period of 1 hour. A linear regression fit to these data results in an entropic heat coefficient of $\frac{\partial U}{\partial T} = -0.11$ (mV/K) with $R^2 = 0.85$.

Test 11

We perform a similar examination of test cell C. This cell obtains a stable temperature after approximately 1.5 hours, which can be observed in figure B.37.

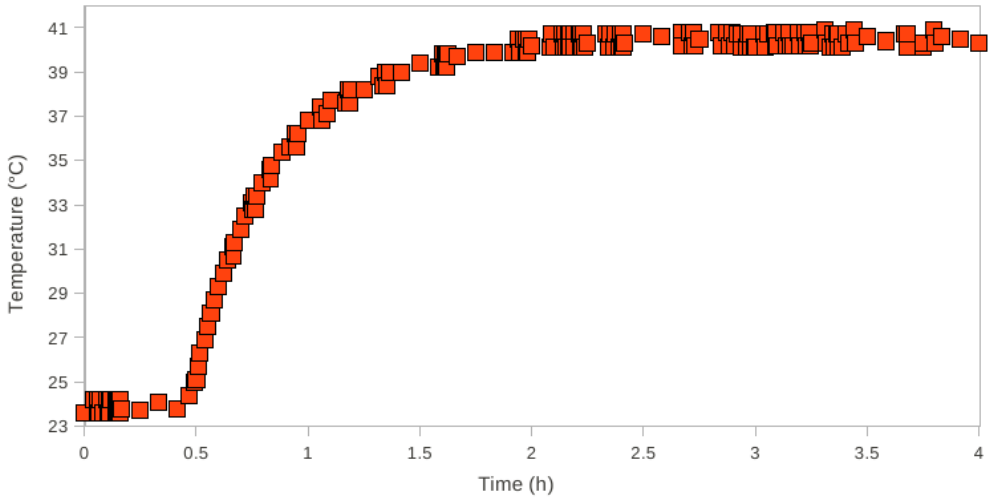

Figure B.37: Surface temperature of test cell C at 50% SOC measured during and after a warmup period.

The cell potential for the constant-temperature period of 2 hours at 40 ℃ for test cell C is shown in figure B.38. As the figure indicates, the self-discharge may be neglected.

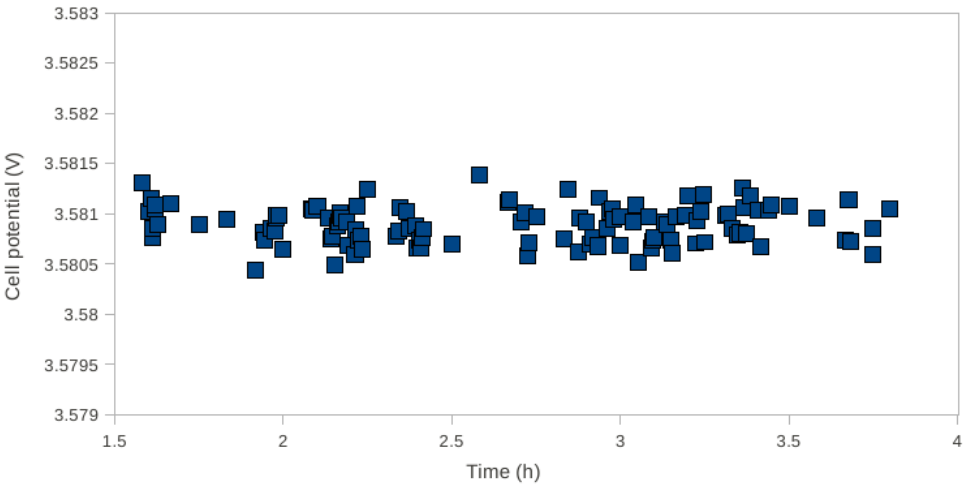

Figure B.38: Cell potential of test cell C at 50% SOC during a constant temperature period of 2 hours at approximately 40 ℃. The trend of the self-discharge indicates that it can be neglected.

Figure B.39 shows the change in cell potential for test cell C plotted against temperature during the warmup period only. A linear regression fit to these data results in an entropic heat coefficient of $\frac{\partial U}{\partial T} = -0.12$ (mV/K) with $R^2 = 0.90$.

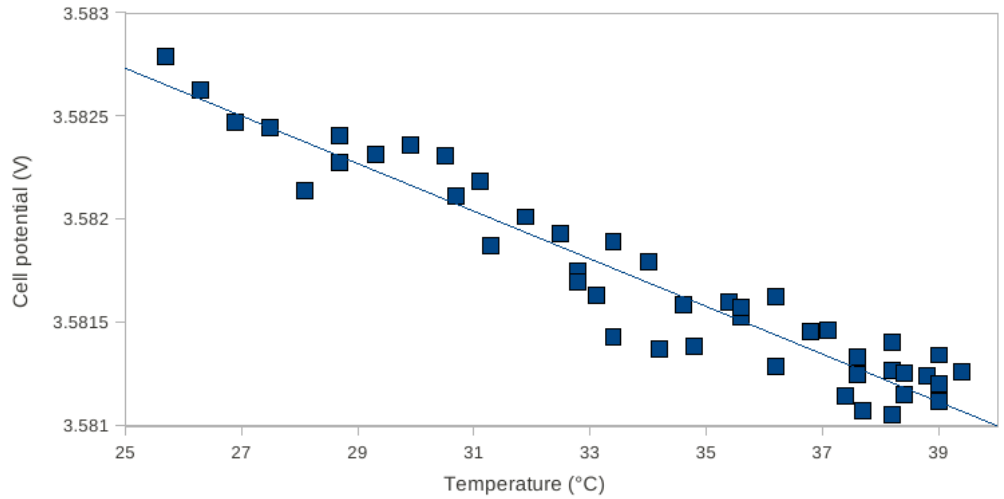

Figure B.39: Cell potential of test cell C at 50% SOC during a warmup period of 1 hour. A linear regression fit to these data results in an entropic heat coefficient of $\frac{\partial U}{\partial T} = -0.12$ (mV/K) with $R^2 = 0.90$.

Test 12

We now study test cell E. Figure B.40 shows the change in cell potential for test cell E plotted against temperature during the warmup period only. A linear regression fit to these data results in an entropic heat coefficient of $\frac{\partial U}{\partial T} = -0.11$ (mV/K) with $R^2 = 0.88$. No data for the self-discharge are available.

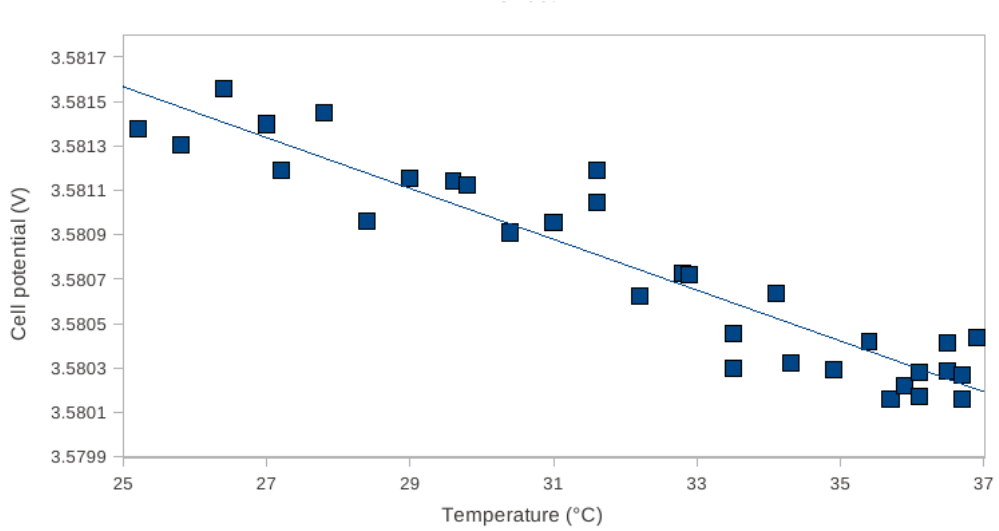

Figure B.40: Cell potential of test cell E at 50% SOC during a warmup period of 1 hour. A linear regression fit to these data results in an entropic heat coefficient of $\frac{\partial U}{\partial T} = -0.11$ (mV/K) with $R^2 = 0.88$.

Test 13

A similar test is performed on test cell G. Figure B.41 shows the change in cell potential for test cell G plotted against temperature during the 1.5 hours cooldown period only. A linear regression fit to these data results in an entropic heat coefficient of $\frac{\partial U}{\partial T} = -0.12$ (mV/K) with $R^2 = 0.81$. No data for the self-discharge are available.

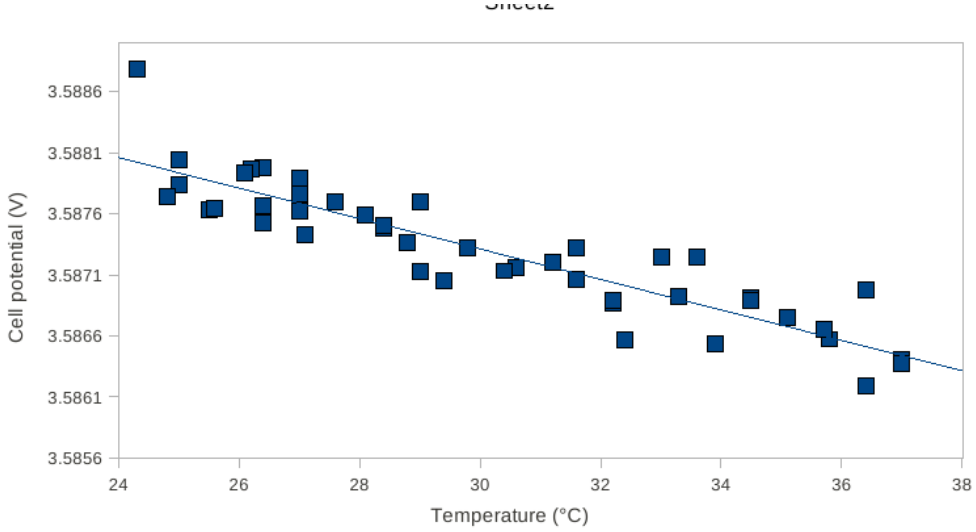

Figure B.41: Cell potential of test cell G at 50% SOC during a cooldown period of 1.5 hours. A linear regression fit to these data results in an entropic heat coefficient of $\frac{\partial U}{\partial T} = -0.12$ (mV/K) with $R^2 = 0.81$.

The results of Test 7 - Test 13 are summarized in table B.4. The first row summarize the results of Test 7. The second row summarize the results of Test 8, and so forth.

Table B.5: Entropic heat coefficient and self-discharge at 50% SOC

Test cell	$\frac{\partial U}{\partial T}$ (mV/K)	R^2	Self discharge (mV/h)	T (℃)	R^2
A	-0.11	0.97	-	-	-
A	-0.12	0.97	-	-	-
A	-0.35	0.98	-	-	-
B	-0.11	0.85	-	-	-
C	-0.12	0.90	0	40	-
E	-0.11	0.88	-	-	-
F	-0.11	0.97	-	-	-
G	-0.12	0.81	-	-	-

B.3 Total Heat Generation

In this section we summarize and make conclusions about the heat generation. This is mainly done based on the presented experimental results in section B.1 and B.2.

B.3.1 Summary and Conclusions

We obtain an excellent expression for the irreversible heat generation in the battery.

In order to examine whether the irreversible or the reversible contributions can be neglected, we compare the sizes of these two.

We first determine the irreversible heat generation rate at 50% SOC, i.e. insert $\sigma = 50$ in equation B.3 which yields

$$I(U - V) = 1.6 \ \ (\text{W}) \tag{B.10}$$

Here $I = 17.5$ (A) for the $1C$ discharge considered in this work. The reversible contribution at 50% SOC is

$$-IT\frac{\partial U}{\partial T} = 0.6 \ (\text{W}) \tag{B.11}$$

where we tacitly assumed $T = 308.15$ (K) and $\frac{\partial U}{\partial T} = -0.11$ (mV/K).

At 80% SOC or we obtain

$$I(U - V) = 1.5 \ (\text{W}) \tag{B.12}$$

Compared to the reversible heat at 80% SOC which is

$$-IT\frac{\partial U}{\partial T} = 2.5 \ (\text{W}) \tag{B.13}$$

where we assumed $T = 308.15$ (K) and $\frac{\partial U}{\partial T} = -0.46$ (mV/K).

This shows that both the irreversible and the reversible heat generation terms are important in the model. This is in accordance with the findings in a work by Viswanathan et al. [58] where also values for the entropy change at various SOC are presented for different lithium ion chemistries. Their presented entropy changes are shown in figure B.42. The label $LiNi_xCo_yMn_zO2-LICO/G-L$ represents a lithium ion cell chemistry with $LiNi_xCo_yMn_zO_2$ cathode and graphite anode.

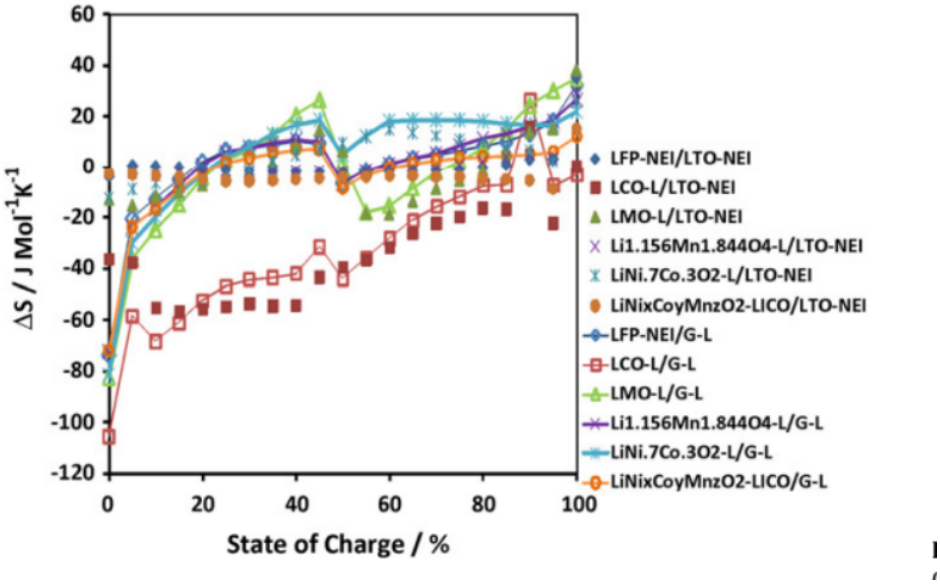

Figure B.42: Entropy change for various lithium ion chemistries. The label $LiNi_xCo_yMn_zO2 - LICO/G - L$ represents a lithium ion cell chemistry with $LiNi_xCo_yMn_zO_2$ cathode and graphite anode. Originally presented by Viswanathan et al. [58]. Reprinted with permission from Elsevier.

We observe in figure B.42 that the $NCM - C$ chemistry has an entropy change and thus a reversible heat generation term that varies significantly with state of charge. The trend do not look linear, so an approximation from the data we have at 50% and 80% SOC would be difficult. Moreover, the reversible heat generation is found to contribute significantly to the total heat generation. Therefore it should not be neglected. We conclude that there is a need to perform measurements of the entropic heat coefficient at other values of state of charge. In this manner a representative expression for the reversible heat generation can be obtained. However, for this modeling work we apply an average value as a representation for the entropic heat coefficient. By consideration of table B.4 in section B.1 and table B.5 in section B.2, we observe that there is consistence in the measured data for the entropic heat coefficient at a given SOC. We choose an entropic heat coefficient from the same pouch-cell as representative values for the average entropic heat coefficient at all SOC. As input to the average value we apply $\frac{\partial U}{\partial T} = -0.11$ (mV/K) for 50% SOC and $\frac{\partial U}{\partial T} = -0.42$ (mV/K) for 80% SOC (test cell B in both values). This results in an average value of the entropic heat coefficient of

$$\hat{\beta} = -0.27 \text{ (mV/K)} \tag{B.14}$$

We denote this average value as $\hat{\beta}$, in order to separate it from the real entropic heat coefficient. One single estimation of the self-discharge at 80% SOC in section B.2.1 show that it may affect the entropic heat coefficient by introducing an error of 11%. We assume that the self-discharge is dependent on temperature, state of charge, and of the battery health. The battery health may depend on the temperature it has been exposed to, the number of cycles and the rate of the cycles [2]. This may explain the difference in self-discharge observed in table B.4 in section B.2. Furthermore, lack of proper self-discharge data indicates that more experiments on self-discharge should be performed. However, since the induced error was found to be relatively small, we neglect the self-discharge in this work.

B.3.2 Input Data for the Heat Source Term

As input parameters to the source term in this work, we need a time dependent expression for the potential difference between the open-circuit potential and the closed-circuit potential, i.e. $(U(t) - V(t))$.

Let us introduce the time-dependent function $\hat{\alpha}(t)$ to describe this potential difference, i.e.

$$\hat{\alpha}(t) = U(t) - V(t) \tag{B.15}$$

However, the potential difference is by the regression approximation (B.3) a function of depth of discharge σ. In order to obtain the relation between time t and depth of discharge σ we consider the current I during discharge. For the $1C$ discharge considered here, the current I is a function of time described as follows:

$$I(t) = \begin{pmatrix} I(t) = 17.5(A) & 0 \leq t \leq t_c \\ I(t) = 0(A) & t > t_c \end{pmatrix} \tag{B.16}$$

Here t_c is the time at end of discharge with unit (s).

Let us introduce T_c as the time at end of discharge with unit (h).

For our data, we have a constant current discharge at $1C$ from $\sigma = 0$ % to $\sigma = 90$ %. Based on the nominal capacity of 17.5 Ah, 15.75 Ah is then extracted from the battery. At this rate, the process requires the time

$$T_c = \frac{15.75 \text{ (Ah)}}{17.5 \text{ (A)}} = 0.90 \text{ (h)} \tag{B.17}$$

In seconds the process requires $t_c = 3240$ (s).

We observe that for the $1C$ constant current discharge, we have the following relation between depth of discharge σ and time t, as far as time is expressed in hours:

$$t = \frac{1}{100}\sigma \tag{B.18}$$

However if time is expressed in seconds the relation is

$$t = 36\sigma \tag{B.19}$$

By (B.19) and (B.3) we now express $\hat{\alpha}(t)$ as

$$\hat{\alpha}(t) = a't^3 + b't^2 + c't + d' \tag{B.20}$$

Here a', b', c' and d' are constants measured in (V/s^3), (V/s^2), (V/s) and (V), respectively. These constants are given in table B.6.

Table B.6: Polynomial coefficients

$a' =$	$(\frac{a}{36^3}) =$	$1.3 \cdot 10^{-11}$	(V/s^3)
$b' =$	$(\frac{b}{36^2}) =$	$-6.461 \cdot 10^{-8}$	(V/s^2)
$c' =$	$(\frac{c}{36}) =$	$9.907361 \cdot 10^{-5}$	(V/s)
$d' =$	$d =$	$4.51243100 \cdot 10^{-2}$	(V)

The other input parameter to the source term is the constant $\hat{\beta}$ that represents the average entropic heat coefficient $\frac{\partial U}{\partial T}$, i.e.

$$\hat{\beta} = -0.27 \text{ (mV/K)} \tag{B.21}$$

B.4 External Heat Transfer Coefficient

The battery we want to model is cycled in a closed cabinet equipped with a fan that constantly blows air around the battery surface. Proper measurements and calculations must be taken to estimate the external heat transfer

coefficient h. However, in a work by Chen et al. [8], an equation for estimating h for forced convection is presented, i.e.

$$h = e(T)\sqrt{\frac{\nu}{L_{kar}}} \tag{B.22}$$

Here $e(T)$ is a temperature dependent coefficient which has units of (J/m^{2}K s$^{0.5}$), ν is the air flow velocity measured in (m/s) and L_{kar} is the characteristic length of the surface measured in (m). Chen et al. [8] also presents the following values of $e(T)$ at two temperatures: $e(298.15\ (\mathrm{K})) = 3.87$ (J/m^{2}K s$^{0.5}$) and $e(323.15\ (\mathrm{K})) = 3.78$ (J/m^{2}K s$^{0.5}$). We assume that the reason that the constant have units of (J) is that it has been integrated over time. Chen et al. [8] states that they use an average value of this constant, since it varies with temperature. This implies that they use a constant value of this coefficient that has the units (W/m^{2}K s$^{0.5}$). However, this is also required to have consistence with the units for h. Details around the derivation and around a valid modeling regime for this coefficient are not given, however. We assume that the coefficient can be considered as a constant in the temperature regime around 298 (K). We furthermore assume that the air velocity is $\nu = 3$ (m/s). The characteristic length is taken as $L_{kar} = 1.45 \cdot 10^{-1}$ (m). The estimated coefficient h is likely to be different for the various surface sides of the battery. However, for simplicity, we apply only one side in our calculation. The result is an estimated value of $h = 18$ (W/m^{2}K).

Furthermore, we observe that external heat transfer coefficients are influenced by many parameters when we study the topic in the book by Cengel [7]. We are especially aware of the fact that the estimated coefficient may not apply for the particular geometry and air flow conditions for our battery. We stress that this estimation must be considered as a guess for this constant, and that proper experimental determination has to be set out to get a more realistic value.

Appendix C

Source Code

```
# Code start

from dolfin import *
import sys
import numpy as numpy
import scitools.easyviz as ev
import scitools.BoxField
import numpy as py


##########################################
# INPUT START
##########################################
# Numerical parameters
##########################################

dt = 0.005 # timestep dist. \Delta \tau
dt_1 = dt # \Delta \tau
T = 1.0 # scaled end of simulation
T_c = 0.725 # scaled time current off

theta_1 = 0.5 # number ok
theta = Constant(theta_1)  # theta-rule i f.d.m.

# Must be the same as command-line input spec. when
# applying Scitools BoxField plotting resources!
```

```
nx = 30
ny = 30
nz = 30

########################################
# Physical size of battery components
########################################

plastic_coat = (3.0)*(1E-05) #(m)
al_case = (11.7)*(1E-05) #(m)
separator = (2.2)*(1E-05) #(m)
cathode_cc_cathode = (17.7)*(1E-05) # 17.7*10^{-5}(m)
anode_cc_anode = (22.0)*(1E-05) #(m)
cc_cathode = (8.0+1.7)*(1E-05) #(m)
cu_cc = (2.2)*(1E-05) #(m)
al_cc = (1.7)*(1E-05) #(m)

period_length = (2*separator + anode_cc_anode \
+ cathode_cc_cathode)

##########################################
# Physical parameters/scaling Constants:
##########################################
#h = 5.0
h = 18.0
g = (273.15 + 25.0)
T_0 = (273.15 + 25.0)
I = 17.5 # Current 1C discharge

B = g
A_s  = 0.01 #  = A in hatu..
alpha = 0.01
C = (1.4e+06)
i = 1.0
c = 1.0
d = 1.0

h_m = h*A_s # h'
g_1 = h*(g-B)  # g'

########################################
```

```
# Gamma_r: Real thermal cond.
########################################

Gamma_plastic_r = 0.40
#Gamma_plastic_r = 177.0 # test of other thermal
# cond in plastic coat
Gamma_Al_cas_r = 177.0
Gamma_sep_r = 1.0
Gamma_half_al_r = 200.0

f_1_r = 920.0*2500   # plastic # unscaled
f_2_r =  2770.0*875  # Al
f_3_r =  1200.0*700  # sep
f_4_r =  2700.0*870  # 1/2 Al.c.c.

########################################
# Gamma: Scaled thermal cond.
########################################

Gamma_plastic_e = (Gamma_plastic_r)/(alpha)
Gamma_Al_cas_e = (Gamma_Al_cas_r)/(alpha)
Gamma_sep_e = (Gamma_sep_r)/(alpha)
Gamma_half_al_e = (Gamma_half_al_r)/(alpha)

f_1_e =  (f_1_r)/(C)  # plastic
f_2_e =  (f_2_r)/(C)  # Al
f_3_e =  (f_3_r)/(C)  # sep
f_4_e =  (f_4_r)/(C)  # 1/2 Al.c.c.

########################################
# Gamma: Scaled thermal cond.
########################################

Gamma_hom_1 = (381.02) # Calculated from scaled
Gamma_hom_2 = (3082.54) # homogenized th. cond.
Gamma_hom_3 = (3082.54) # directly

Gamma_plastic = Constant(Gamma_plastic_e)
Gamma_Al_cas = Constant(Gamma_Al_cas_e)
Gamma_sep = Constant(Gamma_sep_e)
Gamma_half_al = Constant(Gamma_half_al_e)
```

```
f_hom = Constant(1.648) # \langle f \rangle
# Calculated from
#scaled values directly

f_1 =  Constant(f_1_e)  # plastic
f_2 =  Constant(f_2_e)  # Al
f_3 =  Constant(f_3_e)  # sep
f_4 =  Constant(f_4_e)  # 1/2 Al.c.c.

a_r_r = (1.328875171e-11)  #  \alpha= (U-V)
# expressed in t
# in seconds (unscaled)
b_r_r = (-6.461419753e-08)
c_r_r = (9.907361111e-05)
d_r_r = (0.04512431)

t_tau = 4469.2 # diffusion timescale:
#  \tau = \frac{ t }{ t_{\tau} }

a_r = a_r_r*t_tau*t_tau*t_tau  #  \kappa=
# expressed in \tau (scaled)
b_r = b_r_r*t_tau*t_tau
c_r = c_r_r*t_tau
d_r = d_r_r

##########################################
# INPUT END
##########################################

# Automatic calc. of geometry

inner_x1 = 11*cathode_cc_cathode +\
 12*anode_cc_anode + 2*cc_cathode \
- 0.5*2*al_cc + 24*separator

print 'inner_x1=',inner_x1  # thickness in
# x-direction of periodic region

# Physical locations inside the battery
L1_outa_r = plastic_coat #(m)
```

```
#_r denotes physical size

L1_out1a_r = plastic_coat + al_case #(m)

L1_out2a_r = plastic_coat +\
 al_case + separator #(m)

L1_out3a_r = plastic_coat + al_case \
+ separator + 0.5*al_cc #(m)

L1_out3b_r = plastic_coat + al_case +\
 separator + 0.5*al_cc \
+ inner_x1 #(m)

L1_out2b_r = plastic_coat + al_case + \
separator + 0.5*al_cc \
+ inner_x1 + 0.5*al_cc #(m)

L1_out1b_r = plastic_coat + al_case + \
separator + 0.5*al_cc \
+ inner_x1 + 0.5*al_cc + separator #(m)

L1_outb_r = plastic_coat + al_case + \
separator + 0.5*al_cc \
+ inner_x1 + 0.5*al_cc + separator + al_case #(m)

L_x1 = plastic_coat + al_case + \
separator + 0.5*al_cc \
+ inner_x1 + 0.5*al_cc + separator + al_case \
+ plastic_coat #(m)

L_1 = L_x1 # choose scaling constant so that scaled
# region becomes unit.. ## Caution: Do not change,
# code based on scaled region of unity in
# choise of geometry and in partion of
# subdomains, i.e. must have L_xi1 = 1.0.

##

inner_x2 = (23.425e-02) #(m)
inner_x2_tot = inner_x2 + 2*plastic_coat\
```

```
 + 2*al_case + 2*separator

L2_outa_r = plastic_coat #(m) _r denotes physical size

L2_out1a_r = plastic_coat + al_case #(m)

L2_out2a_r = plastic_coat + al_case + separator #(m)

L2_out2b_r = plastic_coat + al_case + separator \
+ inner_x2 #(m)

L2_out1b_r = plastic_coat + al_case + separator \
+ inner_x2 + separator #(m)

L2_outb_r = plastic_coat + al_case + separator \
+ inner_x2 + separator + al_case #(m)

L_x2 = plastic_coat + al_case + separator \
+ inner_x2 + separator + al_case \
+ plastic_coat #(m)

L_2 = L_x2 # choose scaling constant so that scaled
# region becomes unit.. ## Caution: Do not change,
# code based on scaled region of unity in
# choise of geometry and in partion of
# subdomains, i.e. must have L_xi2 = 1.0.

##

inner_x3 = (14.467e-02) #(m)
inner_x3_tot = inner_x3 + 2*plastic_coat \
+ 2*al_case + 2*separator

L3_outa_r = plastic_coat #(m) _r denotes physical size

L3_out1a_r = plastic_coat + al_case #(m)

L3_out2a_r = plastic_coat + al_case + separator #(m)

L3_out2b_r = plastic_coat + al_case + separator \
+ inner_x3 #(m)
```

```
L3_out1b_r = plastic_coat + al_case + separator \
+ inner_x3 + separator #(m)

L3_outb_r = plastic_coat + al_case + separator \
+ inner_x3 + separator + al_case #(m)

L_x3 = plastic_coat + al_case + separator \
+ inner_x3 + separator + al_case \
+ plastic_coat #(m)

L_3 = L_x3 # choose scaling constant so that scaled
# region becomes unit.. ## Caution: Do not change,
# code based on scaled region of unity in
# choise of geometry and in partion of
# subdomains, i.e. must have L_xi3 = 1.0.

##

# Scaled locations inside the battery
L1_outa = (L1_outa_r)/(L_1) #(-)

L1_out1a = (L1_out1a_r)/(L_1) #(-)

L1_out2a = (L1_out2a_r)/(L_1) #(-)

L1_out3a = (L1_out3a_r)/(L_1) #(-)

L1_out3b = (L1_out3b_r)/(L_1) #(-)

L1_out2b = (L1_out2b_r)/(L_1) #(-)

L1_out1b = (L1_out1b_r)/(L_1) #(-)

L1_outb = (L1_outb_r)/(L_1) #(-)

L_xi1 = (L_x1)/(L_1) #(-)

##

L2_outa = (L2_outa_r)/(L_2) #(-)
```

```
L2_out1a = (L2_out1a_r)/(L_2) #(-)

L2_out2a = (L2_out2a_r)/(L_2) #(-)

L2_out2b = (L2_out2b_r)/(L_2) #(-)

L2_out1b = (L2_out1b_r)/(L_2) #(-)

L2_outb = (L2_outb_r)/(L_2) #(-)

L_xi2 = (L_x2)/(L_2) #(-)

##

L3_outa = (L3_outa_r)/(L_3) #(-)

L3_out1a = (L3_out1a_r)/(L_3) #(-)

L3_out2a = (L3_out2a_r)/(L_3) #(-)

L3_out2b = (L3_out2b_r)/(L_3) #(-)

L3_out1b = (L3_out1b_r)/(L_3) #(-)

L3_outb = (L3_outb_r)/(L_3) #(-)

L_xi3 = (L_x3)/(L_3) #(-)

# Inner and outer regions
L1Gammaa = L1_out3a
L1Gammab = L1_out3b
L2Gammaa = L2_out2a
L2Gammab = L2_out2b
L3Gammaa = L3_out2a
L3Gammab = L3_out2b

gamma1 = (L_1)/(L_1) # gamma i diff.op.
gamma2 = (L_1)/(L_2) # gamma i diff.op.
gamma3 = (L_1)/(L_3) # gamma i diff.op.
gamma1_2 = gamma1*gamma1 # gamma i diff.op.
```

```
gamma2_2 = gamma2*gamma2 # gamma i diff.op.
gamma3_2 = gamma3*gamma3 # gamma i diff.op.

brok_1_a = (theta_1*dt_1*L_1*h_m)/(A_s*alpha)
broka = Constant(brok_1_a)

theta_m1 = (1.0-theta_1)
theta_minus1= Constant(theta_m1)

brok_2_a = (theta_1*L_1*dt_1*g_1)/(A_s*alpha)
brok_2 = Constant(brok_2_a)

brok_3_a = (theta_m1*dt_1*L_1*h_m)/(A_s*alpha)
brok_3 = Constant(brok_3_a)

brok_4_a = (theta_m1*dt_1*L_1*g_1)/(A_s*alpha)
brok_4 = Constant(brok_4_a)

#print 'brok_2_a', brok_2_a
#print 'brok_4_a', brok_4_a


print 'L_x1=L_1=', L_x1 # Total thickness in x1-dir.
print 'L_xi1=', L_xi1 # Scaled thickness in xi1-dir.

print 'L_x2=L_2=', L_x2 # Total thickness in x2-dir.
print 'L_xi2', L_xi2 # Scaled thickness in xi2-dir.

print 'L_x3=L_3=', L_x3 # Total thickness in x3-dir.
print 'L_xi3', L_xi3 # Scaled thickness in xi3-dir.

print 'inner_x2_tot', inner_x2_tot
print 'inner_x2_tot', inner_x3_tot

print 'gamma1', gamma1
print 'gamma1_2', gamma1_2
print 'gamma2', gamma2
print 'gamma2_2', gamma2_2
print 'gamma3', gamma3
print 'gamma3_2', gamma3_2
```

```
# Check: Ok

# Automatic spec. of degree of polynomial, of space
# dimension and number of divisons
#
# e.g.
# write "%run filename.py 3 10 4 3" on command-line
# for 3D polynomial of degree 3 and with 10, 4 and
# 3 divisions in the x, y, and z directions
# write "%run filename.py 1 4 3" on command-line
# for 2D polynomial of degree 1 and with 4 and 3 di-
# visions in the x and y directions
degree = int(sys.argv[1])
divisions = [int(arg) for arg in sys.argv[2:]]
d = len(divisions)
domain_type = [UnitInterval, UnitSquare, UnitCube]
mesh = domain_type[d-1](*divisions)

print 'number of space dim: d =', d

V = FunctionSpace(mesh, 'Lagrange', degree)
u = TrialFunction(V) #u must be defined as
# TrialFunction object for the unknown in the
# problem spec.
v = TestFunction(V)

# Define the subdomains for the
# homogenized region and for
# the casing:
# Interior, homogenized region
class Gamma1(SubDomain):
        def inside(self, x, on_boundary):
                if d==3:
                        return True if  \
x[0] >= L1Gammaa and \
                                        \
x[0] <= L1Gammab and \
                                        \
x[1] >= L2Gammaa and \
                                        \
```

```
x[1] <= L2Gammab and \
                                        \
x[2] >= L3Gammaa and \
                                        \
x[2] <= L3Gammab \
                                        \
else False
                elif d==2:
                        return True if \
x[0] >= L1Gammaa and \
                                        \
x[0] <= L1Gammab and \
                                        \
x[1] >= L2Gammaa and \
                                        \
x[1] <= L2Gammab \
                                        \
else False
                elif d==1:
                        return True if \
x[0] >= L1Gammaa and \
                                        \
x[0] <= L1Gammab \
                                        \
else False

#Casing, outermost layer (plastic coating)
class Gamma3(SubDomain):
        def inside(self, x, on_boundary):
                if d==3:
                        return True if \
x[0] <= L1_outa or \
                        x[0] >= L1_outb or \
                        x[1] <= L2_outa or \
                        x[1] >= L2_outb or \
                        x[2] <= L3_outa or \
                        x[2] >= L3_outb else False
                elif d==2:
                        return True if\
 x[0] <= L1_outa or \
                        x[0] >= L1_outb or \
```

```
                        x[1] <= L2_outa or \
                        x[1] >= L2_outb \
                        else False
                elif d==1:
                        return True if \
x[0] <= L1_outa or \
                        x[0] >= L1_outb \
                        else False

#Casing, Al-layer
# d==3,d==2,D==1

class Gamma4(SubDomain):
        def inside(self, x, on_boundary):
                if d==3:
                        return True if \
x[0] <= L1_out1a and \
                        x[0] >= L1_outa and \
                        x[1] <= L2_outb and \
                        x[1] >= L2_outa and \
                        x[2] <= L3_outb and \
                        x[2] >= L3_outa or \
                        x[0] <= L1_outb and \
                        x[0] >= L1_out1b and \
                        x[1] <= L2_outb and \
                        x[1] >= L2_outa and \
                        x[2] <= L3_outb and \
                        x[2] >= L3_outa or \
                        x[1] <= L2_out1a and \
                        x[1] >= L2_outa and \
                        x[0] <= L1_outb and \
                        x[0] >= L1_outa and \
                        x[2] <= L3_outb and \
                        x[2] >= L3_outa or \
                        x[1] <= L2_outb and \
                        x[1] >= L2_out1b and \
                        x[0] <= L1_outb and \
                        x[0] >= L1_outa and \
                        x[2] <= L3_outb and \
                        x[2] >= L3_outa or \
                        x[2] <= L3_outb and \
```

```
                        x[2] >= L3_out1b and \
                        x[0] <= L1_outb and \
                        x[0] >= L1_outa and \
                        x[1] <= L2_outb and \
                        x[1] >= L2_outa or \
                        x[2] <= L3_out1a and \
                        x[2] >= L3_outa and \
                        x[0] <= L1_outb and \
                        x[0] >= L1_outa and \
                        x[1] <= L2_outb and \
                        x[1] >= L2_outa else \
                        False
                elif d==2:
                        return True if \
x[0] <= L1_out1a and \
                        x[0] >= L1_outa and \
                        x[1] <= L2_outb and \
                        x[1] >= L2_outa or \
                        x[0] <= L1_outb and \
                        x[0] >= L1_out1b and \
                        x[1] <= L2_outb and \
                        x[1] >= L2_outa or \
                        x[1] <= L2_out1a and \
                        x[1] >= L2_outa and \
                        x[0] <= L1_outb and \
                        x[0] >= L1_outa or \
                        x[1] <= L2_outb and \
                        x[1] >= L2_out1b and \
                        x[0] <= L1_outb and \
                        x[0] >= L1_outa else \
                        False
                elif d==1:
                        return True if \
x[0] <= L1_out1a and \
                        x[0] >= L1_outa or \
                        x[0] <= L1_outb and \
                        x[0] >= L1_out1b else \
                        False

#Casing, sep-layer
# d==3,d==2,D==1
```

```
class Gamma5(SubDomain):
        def inside(self, x, on_boundary):
                if d==3:
                        return True if \
x[0] <= L1_out2a and \
                        x[0] >= L1_out1a and \
                        x[1] <= L2_out1b and \
                        x[1] >= L2_out1a and \
                        x[2] <= L3_out1b and \
                        x[2] >= L3_out1a or \
                        x[0] <= L1_out1b and \
                        x[0] >= L1_out2b and \
                        x[1] <= L2_out1b and \
                        x[1] >= L2_out1a and \
                        x[2] <= L3_out1b and \
                        x[2] >= L3_out1a or \
                        x[1] <= L2_out2a and \
                        x[1] >= L2_out1a and \
                        x[0] <= L1_out1b and \
                        x[0] >= L1_out1a and \
                        x[2] <= L3_out1b and \
                        x[2] >= L3_out1a or \
                        x[1] <= L2_out1b and \
                        x[1] >= L2_out2b and \
                        x[0] <= L1_out1b and \
                        x[0] >= L1_out1a and \
                        x[2] <= L3_out1b and \
                        x[2] >= L3_out1a or \
                        x[2] <= L3_out1b and \
                        x[2] >= L3_out2b and \
                        x[0] <= L1_out1b and \
                        x[0] >= L1_out1a and \
                        x[1] <= L2_out1b and \
                        x[1] >= L2_out1a or \
                        x[2] <= L3_out2a and \
                        x[2] >= L3_out1a and \
                        x[0] <= L1_out1b and \
                        x[0] >= L1_out1a and \
                        x[1] <= L2_out1b and \
                        x[1] >= L2_out1a else \
```

```
                        False
                elif d==2:
                        return True if \
x[0] <= L1_out2a and \
                        x[0] >= L1_out1a and \
                        x[1] <= L2_out1b and \
                        x[1] >= L2_out1a or \
                        x[0] <= L1_out1b and \
                        x[0] >= L1_out2b and \
                        x[1] <= L2_out1b and \
                        x[1] >= L2_out1a or \
                        x[1] <= L2_out2a and \
                        x[1] >= L2_out1a and \
                        x[0] <= L1_out1b and \
                        x[0] >= L1_out1a or \
                        x[1] <= L2_out1b and \
                        x[1] >= L2_out2b and \
                        x[0] <= L1_out1b and \
                        x[0] >= L1_out1a else \
                        False
                elif d==1:
                        return True if \
x[0] <= L1_out2a and \
                        x[0] >= L1_out1a or \
                        x[0] <= L1_out1b and \
                        x[0] >= L1_out2b else \
                        False

#Casing, half Al.cc.-layer,
#NB! Only relevant for x-direction

class Gamma6(SubDomain):
        def inside(self, x, on_boundary):
                if d==3:
                        return True if \
x[1] <= L2_out2b and \
                        x[1] >= L2_out2a and \
                        x[2] <= L3_out2b and \
                        x[2] >= L3_out2a and \
                        x[0] <= L1_out3a and \
                        x[0] >= L1_out2a or \
```

```
                        x[0] <= L1_out2b and \
                        x[0] >= L1_out3b else \
                        False
                elif d==2:
                        return True if \
x[1] <= L2_out2b and \
                        x[1] >= L2_out2a and \
                        x[0] <= L1_out3a and \
                        x[0] >= L1_out2a or \
                        x[0] <= L1_out2b and \
                        x[0] >= L1_out3b else \
                        False
                elif d==1:
                        return True if \
x[0] <= L1_out3a and \
                        x[0] >= L1_out2a or \
                        x[0] <= L1_out2b and \
                        x[0] >= L1_out3b else \
                        False

subdomains = MeshFunction('uint', mesh, d)
#subdomains1 = MeshFunction('uint', mesh, d)
subdomains.set_all(0) # Set all as 0 first for safety

subdomain1 = Gamma1()
subdomain1.mark(subdomains, 0)
#subdomain2 = Gamma2()
#subdomain2.mark(subdomains, 1)
subdomain3 = Gamma3()
subdomain3.mark(subdomains, 1)
subdomain4 = Gamma4()
subdomain4.mark(subdomains, 2)
subdomain5 = Gamma5()
subdomain5.mark(subdomains, 3)
subdomain6 = Gamma6()
subdomain6.mark(subdomains, 4)

#All UFL code coeff. must be expressed as constants

G_plastic = Gamma_plastic
# Possible to not use Const. if only app. in matrix
```

```
G_Al_cas = Gamma_Al_cas
G_sep =Gamma_sep
G_half_al = Gamma_half_al

G1 = Gamma_hom_1*gamma1_2
G2 = G_plastic*gamma1_2
G3 = G_Al_cas*gamma1_2
G4 = G_sep*gamma1_2
G5 = G_half_al*gamma1_2

vol = inner_x1*inner_x2*inner_x3
vol_total = L_x1*L_x2*L_x3


print 'vol=', vol
print 'vol_total=', vol_total
print 'inner_x1, inner_x2, inner_x3',\
 inner_x1, inner_x2, inner_x3

if d==1:
        A1 = Constant(G1)
        A2 = Constant(G2)
        A3 = Constant(G3)
        A4 = Constant(G4)
        A5 = Constant(G5)
elif d==2:
        A1 = as_matrix ([[Gamma_hom_1*gamma1_2, 0.0],\
 [0.0, Gamma_hom_2*gamma2_2]])
        A2 = as_matrix ([[G_plastic*gamma1_2, 0.0],\
 [0.0, G_plastic*gamma2_2]])
        A3 = as_matrix ([[G_Al_cas*gamma1_2, 0.0],\
 [0.0, G_Al_cas*gamma2_2]])
        A4 = as_matrix ([[G_sep*gamma1_2, 0.0],\
 [0.0, G_sep*gamma2_2]])
        A5 = as_matrix ([[G_half_al*gamma1_2, 0.0],\
 [0.0, G_half_al*gamma2_2]])
elif d==3:
        A1 = as_matrix (\
[[Gamma_hom_1*gamma1_2, 0.0, 0.0],\
 [0.0, 0.0, Gamma_hom_2*gamma2_2],\
 [0.0, 0.0, Gamma_hom_3*gamma3_2]])
```

```
        A2 = as_matrix (\
[[G_plastic*gamma1_2, 0.0, 0.0],\
 [0.0, 0.0, G_plastic*gamma2_2],\
 [0.0, 0.0, G_plastic*gamma3_2]])
        A3 = as_matrix (\
[[G_Al_cas*gamma1_2, 0.0, 0.0],\
 [0.0, 0.0, G_Al_cas*gamma2_2],\
 [0.0, 0.0, G_Al_cas*gamma3_2]])
        A4 = as_matrix (\
[[G_sep*gamma1_2, 0.0, 0.0],\
 [0.0, 0.0, G_sep*gamma2_2],\
 [0.0, 0.0, G_sep*gamma3_2]])
        A5 = as_matrix (\
[[G_half_al*gamma1_2, 0.0, 0.0],\
 [0.0, 0.0, G_half_al*gamma2_2],\
 [0.0, 0.0, G_half_al*gamma3_2]])

# Initial Condition
ToAB_1 = (T_0-B)/(A_s)
ToAB = Constant(ToAB_1)

#u_prev = interpolate(ToAB,V)
u_prev = project(ToAB, V)

t = dt # staa som tall
tol = 1E-05 # staa som tall

I = 17.5

hat_beta = -0.00027; L_1 = L_1
P = Expression('(-I*(pow(L_1,2))*hat_beta)/(alpha*vol)',
               {'I=I': I, 'alpha': alpha, 'vol': vol,
                'L_1': L_1, 'hat_beta': hat_beta})

O = Expression('((I*(pow(L_1,2)))/(A_s*alpha*vol))*\
( a_r*pow(t,3) + b_r*pow(t,2) + c_r*(t) + d_r -B*\
hat_beta)', {'I': I, 'L_1': L_1, 'A_s': A_s,\
 'alpha': alpha,\
'vol': vol, 'B': B, 'hat_beta': hat_beta,\
'a_r': a_r, 'b_r': b_r, 'c_r': c_r, 'd_r': d_r, 't': t})
```

```
P_prev = Expression('(-I*(pow(L_1,2))*hat_beta)/(alpha*vol)',
                    {'I': I, 'alpha': alpha, 'vol': vol,\
 'L_1': L_1, 'hat_beta': hat_beta})

O_prev = Expression('((I*(pow(L_1,2)))/(A_s*alpha*vol))*\
( a_r*pow((t-dt),3) + b_r*pow((t-dt),2) + c_r*(t-dt) + \
d_r -B*hat_beta)',
                    {'I': I, 'L_1': L_1, 'A_s': A_s,\
 'alpha': alpha,
                     'vol': vol, 'B': B,\
 'hat_beta': hat_beta,\
 'a_r': a_r, 'b_r': b_r, 'c_r': c_r, 'd_r': d_r,\
 't': t, 'dt': dt})

P.I = 17.5
O.I = 17.5
P_prev.I = 17.5
O_prev.I = 17.5

O.t = 0.0

O_prev.t = dt
O_prev.dt = dt

#O_plot = interpolate(O,V)
#plot(O_plot) # O gir rett verdi i t = 0
#O2_plot = interpolate(O_prev,V)
#plot(O2_plot) # O_prev gir rett verdi i t = 0
#P_plot = interpolate(P,V)
#plot(P_plot) # P gir rett verdi for alle t
#P2_plot = interpolate(P_prev,V)
#plot(P2_plot) # P_prev gir rett verdi for alle t

# UFL-code for var.form. representation:
a = f_hom*inner(u,v)*dx(0) + f_1*inner(u,v)*dx(1) \
+ f_2*inner(u,v)*dx(2) \
+ f_3*inner(u,v)*dx(3) + f_4*inner(u,v)*dx(4) \
+ theta*dt*inner(A1*grad(u),grad(v))*dx(0) \
- theta*dt*P*inner(u,v)*dx(0) \
+ theta*dt*inner(A2*grad(u),grad(v))*dx(1) \
+ theta*dt*inner(A3*grad(u),grad(v))*dx(2) \
```

```
+ theta*dt*inner(A4*grad(u),grad(v))*dx(3) \
+ theta*dt*inner(A5*grad(u),grad(v))*dx(4) \
+ broka*u*v*ds

L = f_hom*u_prev*v*dx(0) + f_1*u_prev*v*dx(1) \
+ f_2*u_prev*v*dx(2) + f_3*u_prev*v*dx(3)\
+ f_4*inner(u_prev,v)*dx(4) - theta_minus1*dt\
*inner(A1*grad(u_prev),grad(v))*dx(0) \
+ theta*dt*O*v*dx(0) + theta_minus1*dt*O_prev*v*dx(0) \
+ theta_minus1*dt*P_prev*inner(u_prev,v)*dx(0) \
- theta_minus1*dt*inner(A2*grad(u_prev),grad(v))*dx(1) \
- theta_minus1*dt*inner(A3*grad(u_prev),grad(v))*dx(2) \
- theta_minus1*dt*inner(A4*grad(u_prev),grad(v))*dx(3) \
- theta_minus1*dt*inner(A5*grad(u_prev),grad(v))*dx(4) \
+ brok_2*v*ds - brok_3*inner(u_prev,v)*ds \
+ brok_4*v*ds

b = None

# Plot initial condition
X = 0; Y = 1; Z = 0
u2 = interpolate(u_prev, FunctionSpace(mesh,\
 'Lagrange', 1))
u_box = scitools.BoxField.\
dolfin_function2BoxField(u2,\
mesh, (nx,ny), uniform_mesh=True)

#ev.figure()
#ev.surf(u_box.grid.coorv[X],\
# u_box.grid.coorv[Y], u_box.values,
#shading='interp', xlabel='{/Symbol x}_{1}',\
# ylabel='{/Symbol x}_{2}', colorbar='on',
#title='', hardcopy='u_2d_t00_surf.eps')

# Extract and plot u along the line y=0.5
#start = (0,0.5)
#x0, uval0y, y_fixed, snapped =\
# u_box.gridline(start, direction=X)
# Extract and plot u along the line x=0.5
#start = (0.5,0)
#y0, uval0x, x_fixed, snapped = \
```

```
#u_box.gridline(start, direction=Y)

# plot mesh
#s = plot(mesh, title='Finite element mesh')
#s.write_png('mesh_2d.png')

while t <= T:
        print 't=', t
        if t<(T_c-tol):
                P.I =  17.5
                O.I =   17.5
                P_prev.I =   17.5
                O_prev.I =  17.5
                O.t = t
                O_prev.t = t
                #O_plot = interpolate(O,V)
                #plot(O_plot)
                #O_plot = interpolate(O_prev,V)
                #plot(O_plot)
        elif t>(T_c-tol) and t<(T_c+tol):
                P.I = 0.0
                O.I = 0.0
                P_prev.I =  17.5
                O_prev.I =  17.5
                O_prev.t = t
        elif t>(T_c+tol):
                P.I = 0.0
                O.I = 0.0
                P_prev.I = 0.0
                O_prev.I = 0.0
                #O_plot = interpolate(O,V)
                #plot(O_plot)
                #O_plot = interpolate(O_prev,V)
                #plot(O_plot)
#               O_plot = interpolate(P,V)
#               plot(O_plot)
#               O_plot = interpolate(P_prev,V)
#               plot(O_plot)
        A = assemble(a, cell_domains=subdomains)
        b = assemble(L, cell_domains=subdomains)
#       b = assemble(L, cell_domains=subdomains, tensor=b)
```

```
# Tensor seems to be remarkable similar
# in computation time as without tensor argument.

        u = Function(V)
        solve(A, u.vector(), b)

        if t>(0.735-tol) and t<(0.735+tol):
                X = 0; Y = 1; Z = 0
                u2 = u if u.ufl_element().degree()\
 == 1 else \
                interpolate(u, FunctionSpace(mesh,\
 'Lagrange', 1))
                u_box = \
scitools.BoxField.dolfin_function2BoxField(u2,\
                mesh, (nx,ny), uniform_mesh=True)

                # Extract and plot u along the line y=0.5
                start = (0,0.5)
                x0735, uval0735y, y_fixed,\
 snapped = u_box.gridline(start, direction=X)
                # Extract and plot u along the line x=0.5
                start = (0.5,0)
                y0735, uval0735x, x_fixed,\
 snapped = u_box.gridline(start, direction=Y)

                ev.figure()
                ev.plot(y0735, uval0735x, title='',
                legend=('{/Symbol t} = 0.735'),\
 xlabel='{/Symbol x}_{2}', legend_fancybox=True,
                hardcopy='testtest.eps')

        t = t + dt
        u_prev.assign(u)

# Code end
```